

ISSN 1883 - 0315

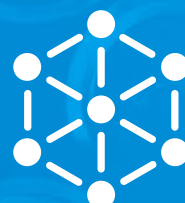


TOHOKU  
UNIVERSITY

# IMR

## KINKEN Research Highlights 2022

Institute for Materials Research, Tohoku University



Research



# KINKEN

## Research Highlights

### 2022



Institute for Materials Research, Tohoku University

# KINKEN Research Highlights 2022

## Contents

<b>Preface</b> .....	4
----------------------	---

## Research Highlights

### 1. Infrastructural Materials

Microstructure Design of Structural Metallic Materials Research Laboratory.....	8
Irradiation Effects in Nuclear and Their Related Materials Research Laboratory.....	9
Environmentally Robust Materials Research Laboratory .....	10
Advanced Crystal Engineering Research Laboratory .....	11
Non-Equilibrium Materials Research Laboratory.....	12
Deformation Processing Research Laboratory .....	13
Analytical Science Research Laboratory .....	14
Design & Engineering by Joint Inverse Innovation for Materials Architecture (DEJI <sup>2</sup> MA) .....	15
Professional development Consortium for Computational Materials Scientists (PCoMS) .....	16

### 2. Energy-Related Materials

Materials Design by Computer Simulation Research Laboratory.....	18
Nuclear Materials Engineering Research Laboratory .....	19
Chemical Physics of Non-Crystalline Materials Research Laboratory .....	20
Structure-Controlled Functional Materials Research Laboratory .....	21
Magnetic Materials Research Laboratory .....	22
Hydrogen Functional Materials Research Laboratory .....	23

### 3. Electronic Materials

Theory of Solid State Physics Research Laboratory .....	26
Crystal Physics Research Laboratory .....	27
Magnetism Research Laboratory .....	28
Low Temperature Physics Research Laboratory.....	29
Low Temperature Condensed State Physics Research Laboratory.....	30
Quantum Beam Materials Physics Research Laboratory .....	31
Quantum Functional Materials Physics Research Laboratory .....	32
Solid-State Metal-Complex Chemistry Research Laboratory.....	33

Crystal Chemistry Research Laboratory .....	34
Actinide Materials Science Research Laboratory .....	35
Materials Science of Non-Stoichiometric Compounds Research Laboratory .....	36
Exploratory Research Laboratory.....	37

## Research Centers

International Research Center for Nuclear Materials Science.....	40
Cooperative Research and Development Center for Advanced Materials .....	41
High Field Laboratory for Superconducting Materials.....	42
Trans-Regional Corporation Center for Industrial Materials Research .....	43
Collaborative Research Center on Energy Materials.....	44
Center for Computational Materials Science.....	45
Center of Neutron Science for Advanced Materials .....	46
International Collaboration Center (ICC-IMR).....	47
Center for Advanced Light Source and Materials Science .....	48
Laboratory of Low Temperature Materials Science .....	49
Laboratory of Alpha-Ray Emitters .....	50
Analytical Research Core for Advanced Materials.....	51

## International Collaborative Research

Magnetism Research Laboratory .....	54
Microstructure Design of Structural Metallic Materials Research Laboratory.....	55
Advanced Crystal Engineering Research Laboratory .....	56
Non-Equilibrium Materials Research Laboratory.....	57
Magnetic Materials Research Laboratory .....	58
International Research Center for Nuclear Materials Science.....	59
Cooperative Research and Development Center for Advanced Materials .....	60
High Field Laboratory for Superconducting Materials.....	61
Center for Computational Materials Science.....	62
Center of Neutron Science for Advanced Materials .....	63



# Preface

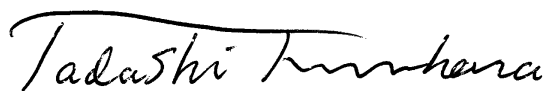
Dear Colleagues,

We are pleased to present *KINKEN* Research Highlights 2022, which is the annual report that includes a collection of research outputs of the past year from the Institute for Materials Research (IMR), Tohoku University. *KINKEN* is the abbreviation for “Kinzoku Zairyo Kenkyujo,” the Japanese name for IMR, which is well known in the materials science community.

IMR was the first Tohoku University research institute, of which there are currently six, to be established in 1916. Aiming to contribute to the well-being of the human race and the development of civilization through the creation of new materials that are useful to society, it carries out research on both the fundamentals and applications of a wide range of substances and materials. After its founding, IMR first focused on steel but quickly expanded its research area to the other metals and alloys. Then, in response to changing times and economic growth, it came to cover semiconductors, ceramics, and a wide range of other materials. Ever since our first director, Professor Kotaro Honda, invented the first artificial permanent magnet called “KS steel,” we have developed many new materials for practical use, including Sendust alloy, SiC fibers, and soft magnetic amorphous alloys. We have also focused on fundamental research, which is important for the development of new materials, as well as carried out cutting-edge research on magnetism, optical properties, superconductivity, and microstructure of materials. While doing so, IMR has become a leading research institute in the field of materials science.

IMR is notable for its fusion of fundamental and applied research, as well as of science and engineering. We offer some of the best large research facilities in the world — covering high-energy





Director Prof. Tadashi Furuhashi



irradiation, strong magnetic fields, and supercomputing — enabling researchers from Japan and abroad to engage in a variety of collaborative projects. To develop superior or new materials that are useful, we believe it is necessary to organically connect three “pillars”: (1) the “exploration” of physical phenomena that govern materials’ functions, (2) the “creation” of materials via various methods, and (3) the “measurement” of materials’ properties from various perspectives. IMR has for many years been contributing to the materials research community via our joint usage/research programs. IMR celebrated its 100-year anniversary in 2016. Having been designated in 2018 as an International Joint Usage/Research Center in Materials Science, known as Global Institute for Materials Research Tohoku (GIMRT), we have now further heightened our efforts to enhance such collaborations and cultivate new talent.

In the 21st century, our society faces global-scale environmental issues, such as global warming, resource depletion, acquiring a stable energy supply, and new kinds of environmental pollution. IMR will continue to work towards a sustainable society both by engaging in important research to solve various problems as well as by creating new areas of research that can bring about paradigm shifts in the future.

We hope that the KINKEN Research Highlights will enable you to better understand our recent research activities and will aid the promotion of worldwide collaboration with IMR. We ask for your continued support and welcome any suggestions.





## ***Infrastructural Materials***

IMR KINKEN Research Highlights 2022



# Ferrite Transformation in Fe-0.3N Alloy

Ferrite transformation behavior during isothermal holding was studied in the ferrite ( $\alpha$ ) + austenite ( $\gamma$ ) two-phase region of Fe-0.3mass%N binary alloy. Two morphologies of Allotriomorphic ferrite (AF) and Widmanstetten ferrite (WF) formed from the prior  $\gamma$  grain boundary. The retained  $\gamma$  was obtained by decreasing the transformation temperature in the two-phase region, and a maximum volume fraction of 9% was obtained by holding at 600 °C. AF had a near Kurdjumov-Sachs orientation relationship (K-S OR) with one side of the adjacent  $\gamma$  grains and grew into the  $\gamma$  grains without K-S OR. On the other hand, WF had a near K-S OR with the matrix.

Nitrogen is an interstitial element and thermodynamically stabilizes the  $\gamma$  phase in Fe alloys. It is known that the behavior of nitrogen in iron shows a similar tendency to carbon with respect to the concentration dependence of the change in the  $A_{e3}$  or  $M_s$  temperature and the lattice constant [1-3]. On the other hand, due to the difference in thermodynamic stability between iron nitride and iron carbide in  $\gamma$ , the eutectoid temperature and concentration are different between Fe-C and Fe-N binary systems, and the  $A_{e1}$  point in Fe-N is lower in temperature and higher in concentration than Fe-C alloy. These characteristics of Fe-N alloy can be applied to a new kind of TRIP steel using retained  $\gamma$  stabilized by N enrichment.

In this study, Fe-0.3mass%N austenite was prepared by a gas nitriding process. The nitrided sample was directly dropped into a salt bath heated to the  $\alpha$ + $\gamma$  two phase region of 600–750 °C and isothermally treated for 3–3600 s. The microstructure of the heat-treated samples was observed using FE-SEM, and the volume fraction of constituent phases was determined by point counting and XRD.

Figure 1 shows OM images of Fe-0.3N alloy isothermally treated at 600–750 °C for various period of times. At 750 °C, AF is formed at the  $\gamma$  grain boundary after 5 s. Transformation rapidly progresses by 60 s, and the  $\gamma$  grain boundaries are covered by AF. At 600 °C, AF and WF are formed along the  $\gamma$  grain boundary, and Martensite-Austenite constituent (MA) exists between adjacent WFs.

Figure 2 shows the transformation kinetics curve of the isothermally treated samples. In the 750 °C sample, the  $\alpha$  volume fraction in the early stage was small, and reached about 10% after 10 s. The transformation then proceeded more rapidly and an equilibrium volume fraction of 65% was obtained at 3600 s. At 600 °C, the  $\alpha$  transformation was faster due to the increasing driving force, and the initial  $\alpha$  volume fraction was much higher than that of 750 °C. From the XRD measurement, it was found that

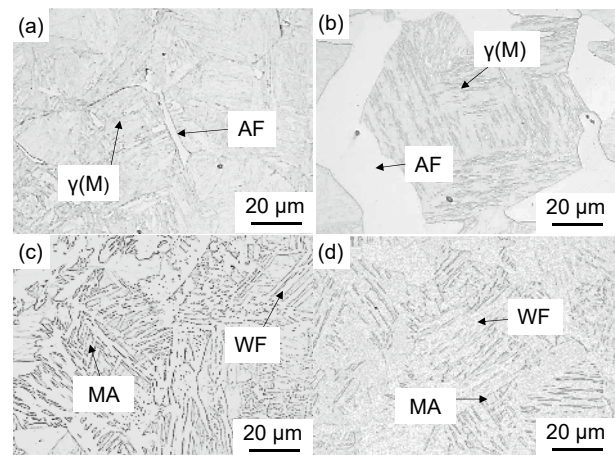


Fig. 1 Microstructures of isothermally treated samples. (a) 5 s and (b) 3600 s at 750 °C, (c) 5 s and (d) 3600 s at 600 °C, respectively [4].

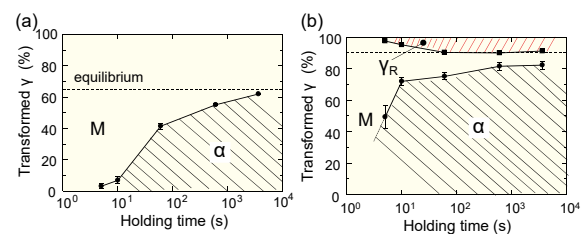


Fig. 2 Ferrite transformation kinetics curves of Fe-0.3N alloy isothermally treated at (a) 750 °C and (b) 600 °C [4].

the amount of retained  $\gamma$  increased with an increased holding time. A value of 9% retained  $\gamma$  was obtained at 600 s holding, and remained constant during further holding.

## References

- [1] Y. Imai, Tetsu-to-Hagané, **51**, 2336 (1965).
- [2] L. Chen and E. J. Mittemeijer, Scripta Metall. Mater., **24**, 509 (1990).
- [3] T. Tsuchiyama, K. Inoue, K. Hyodo, D. Akama, N. Nakada, S. Takaki, and T. Koyano, ISIJ Inter., **59**, 161 (2019).
- [4] M. Sato, T. Murata, S. Shimaya, G. Miyamoto, and T. Furuhashi, ISIJ Inter., **61**, 343 (2021)

Mitsutaka Sato (Microstructure Design of Structural Metallic Materials Research Laboratory)

E-mail: mitsutaka.sato.a3@tohoku.ac.jp

URL: <http://www.st-mat.imr.tohoku.ac.jp/en/index.html>

# Growth Sequence of Long-Period Stacking-Ordered Phase in Mg-Al-Gd Alloy Investigated by Correlative Atom Probe Tomography and Scanning Transmission Electron Microscopy

Atom probe tomography (APT) and scanning transmission electron microscopy (STEM) were used correlatively to explore atomic-scale local structure and chemistry of the same area in the vicinity of the growth front of a long-period stacking ordered (LPSO) phase in a ternary Mg-Al-Gd alloy. The correlative method revealed the growth sequence of the LPSO phase in Mg-Al-Gd alloy.

Mg-M-RE (M: metal, RE: rare-earth elements) alloys such as those in Mg-Zn-Y and Mg-Al-Gd systems have received considerable attention as a new class of structural materials. In these Mg-M-RE alloys, unique platelet precipitates so-called 'synchronized' long-period stacking ordered (LPSO) phases are known to form. The synchronized LPSO phase consists of hexagonally-arranged close-packed atomic layers stacked along their plane normal ([0001] in the hexagonal closed packed (hcp) notation), in which M and RE atoms are enriched to form  $M_6RE_8$  atomic clusters with the L1<sub>2</sub>-type atomic arrangement based on face-centered cubic stacking in four consecutive atomic layers that are bounded by several Mg layers with hcp stacking.

Scanning transmission electron microscopy (STEM) with angstrom spatial resolution, in particular Z (atomic number)-contrast imaging by high-angle annular dark-field (HAADF)-STEM has provided various structural and chemical information for LPSO phases at an atomic scale. However, differentiating atoms with close atomic numbers is usually very difficult. Differentiating Mg (Z=12) and Al (Z=13) in Mg-Al-Gd ternary alloys is one typical case. Atom probe tomography (APT), by which a 3D elemental map can be reconstructed at (sub-) nanometer spatial resolution for a needle specimen, is a unique method that possesses high analytical sensitivity and high mass-resolving capability [1,2]. This means that APT can provide elemental information that is difficult to obtain simply by atomic-resolution Z-contrast STEM imaging. However, the spatial resolution in APT analysis is insufficient to capture crystallographic information on crystal and defect structures that can be obtained by TEM/STEM imaging.

In this study, we investigated variations of atomic structures and elemental distributions on an atomic scale occurring at the interface region between the LPSO and Mg phases in a Mg-Al-Gd alloy, using correlative APT and TEM/STEM in the same regions, in order to better understand how chemical modulation synchronizes with structural modulation in the growth

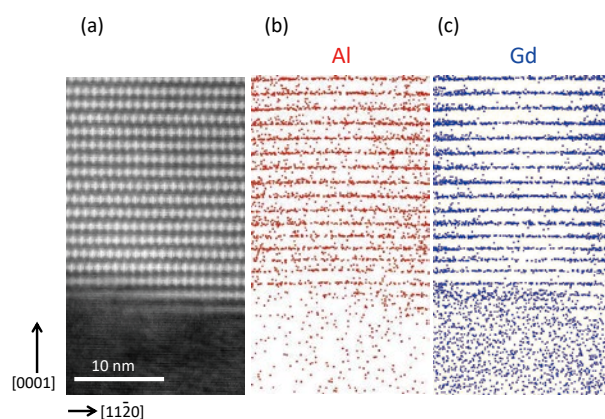


Fig.1 (a) HAADF-STEM image taken along the  $[1\bar{1}00]$  direction. (b), (c) APT maps for Al and Gd in the same region as the HAADF-STEM image.

sequence of the synchronized LPSO phase.

Figure 1(a), 1(b), and 1(c) respectively show a HAADF-STEM image taken along the  $[1\bar{1}00]$  direction, and APT maps for Al and Gd in the vicinity of the interface between the LPSO and Mg phases. (0001) Gd-enriched atomic layers in the transition region at the interface changed in the HAADF-STEM contrast from a row of double-dagger patterns (right-hand side) to a slightly brighter line (left-hand side) (Fig. 1(a)). In these (0001) Gd-enriched atomic layers in the transition region, while Gd enrichment extends across the areas where the HAADF-STEM contrast changes, Al enrichment is limited only to the layers where a row of double-dagger patterns is observed. This confirms that the formation of  $Al_6Gd_8$  clusters occurs only after sufficient Al atoms to form  $Al_6Gd_8$  clusters reach the relevant portions [3].

## References

- [1] T. Yoshiie, K. Inoue, K. Yoshida, T. Toyama, Y. Satoh, and Y. Nagai, *Philos. Mag.* **101**, 1202 (2021).
- [2] D. Egusa, K. Inoue, Y. Nagai, and E. Abe, *Mater. Charact.* **177**, 111153 (2021).
- [3] K. Inoue, K. Yoshida, Y. Nagai, K. Kishida, and H. Inui, *Sci. Rep.* **11**, 3073 (2021).



# Microstructure Creation via High-pressure Hydrogenation and Subsequent Dehydrogenation in a Face-Centered Cubic Steel

Hydrogen in steels has the potential to improve mechanical properties via alteration of phase stability and plasticity. A stoichiometric composition of hydrogen can be introduced for steel compositions, enabling unconventional diffusionless transformation. For instance, hydrogenation/dehydrogenation treatment in an fcc steel resulted in a fine lath bcc structure arising from diffusionless transformation with the sequence of face-centered cubic (fcc)→hexagonal close-packed (hcp)→double hexagonal close-packed (dhcp)→body-centered cubic(bcc).

The use of diffusionless transformation has been key to designing high-strength steel and iron alloys. The strength of the diffusionless transformation phase can be increased by increasing the content of interstitial atoms such as carbon and nitrogen, microstructure boundary density, and dislocation density. Therefore, one strategy for improving the strength of steel alloy is to use the interstitial elements to control the substructure of the diffusionless transformation phase. Hydrogen is also an interstitial element in steels, and it has recently been noted as a promising element that enables the control of microstructures associated with diffusionless transformation [1]. Moreover, a large amount of hydrogen can be introduced into steel by pressurizing the sample with hydrogen, causing a dramatic change in microstructure [2]. Here, we examine the effect of hydrogen on the microstructure associated with diffusionless transformation in steels.

In this study, we used a SUS304L metastable austenitic stainless steel. Two SUS304L samples were pressurized to 9 GPa without and with a hydrogen source ( $\text{AlH}_3$ ), heated to 973 K, and subsequently depressurized at 293 K. Some interesting differences were found between the samples with and without hydrogenation. First, the constituent phases were different; the microstructure without hydrogen mainly consisted of fcc phase, whereas the hydrogenated microstructure was fully composed of bcc phase after depressurization. In terms of microstructure morphology, the non-hydrogenated sample showed equi-axed coarse grains with some thin plates (Fig. 1(a)). In contrast, the hydrogenated microstructure morphology was a fine lath (Fig. 1(b)), which is a typical morphology of bcc diffusionless transformation phase in steels. In addition, the dislocation density was higher in the hydrogenated sample than that in the non-hydrogenated sample. As the dislocations that were introduced during the pressurization were removed during recrystallization at 973 K, the numerous dislocations observed were introduced during the cooling and depressurization. Furthermore, through in situ diffraction experiments, the transformation

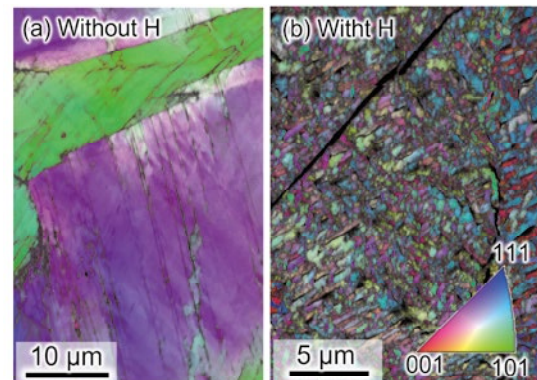


Fig. 1 Inverse pole figure maps showing the microstructures after high-pressure heat treatment (a) without and (b) with hydrogen [3].

sequence in the hydrogenated sample was clarified to be fcc→hcp→dhcp→bcc.

The important finding here is the fact that “the hydrogenation–dehydrogenation treatment could refine the microstructure (below 300 nm) and introduce numerous dislocations by inducing/promoting diffusionless transformation”. It is also noteworthy that SUS304L does not show a microstructure that consists fully of the bcc phase arising from diffusionless transformation, as long as the steel is not severely deformed. That is, we can say that the hydrogenation–dehydrogenation treatment can create an unconventional microstructure in the metastable fcc steel. The fine microstructure with numerous dislocations was found to show higher hardness than that of the non-hydrogenated sample. Thus, a hydrogenation–dehydrogenation treatment could be used for developing high-strength steels in the future.

## References

- [1] M. Koyama, C. Hao, E. Akiyama, and K. Tsuzaki, *Metall. Mater. Trans. A* **51**, 4439 (2020).
- [2] M. Koyama, H. Saitoh, T. Sato, S. Orimo, and E. Akiyama, *Mater. Lett. X* **11**, 100078 (2021).
- [3] M. Koyama, H. Saitoh, T. Sato, S. Orimo, and E. Akiyama, *Sci. Rep.* **11**, 19384 (2021).

Motomichi Koyama (Environmentally Robust Materials Research Laboratory)

E-mail: motomichi.koyama.c5@tohoku.ac.jp

URL: <https://akiyamaimr-e.amebaownd.com/>

# Co-Cr-Mo Crystal Fibers Fabricated from the Melt by Unidirectional Solidification

A novel fabrication technique for CCM alloy crystal fibers was developed by unidirectional solidification directly from the melt using the alloy-micro-pulling-down (A- $\mu$ -PD) method. Compared with conventional methods, the proposed innovative technique is characterized by low cost, time saving, and low loading. The growth rate in the A- $\mu$ -PD method had a noticeable effect on the fabrication of single- or poly-crystalline CCM fibers.

The micro-pulling-down ( $\mu$ -PD) method is appropriate for growing shape-controlled single crystals directly from the melt. Based on the shape-control technique of the  $\mu$ -PD method, we previously developed an alloy- $\mu$ -PD (A- $\mu$ -PD) method for the fabrication of metal and alloy fibers directly from the melt [1].

Co-Cr-Mo (CCM) alloys have been investigated for various applications of biomedical materials. However, the mechanical properties of as-cast CCM alloys are limited; in particular, the low ductility and fatigue strength are a matter of concern for applications.

In this study, we developed an innovative technique to fabricate CCM crystal fibers from the melt using the A- $\mu$ -PD method without the problem of the poor workability of CCM alloys [2].

CCM fibers were fabricated by the A- $\mu$ -PD method using an  $\text{Al}_2\text{O}_3$  crucible. The liquid-solid interface was located just below the crucible bottom, and the fabricated CCM fiber diameter could be controlled by maintaining the position of the liquid-solid interface within the crucible hole during the fiber fabrication.

The SEM image of  $\phi 2$  mm CCM fiber grown at 0.5 mm/min (CCM2[0.5]) was clearly different from those of fibers grown at 0.1 and 0.3 mm/min (CCM2[0.1] and CCM2[0.3]) (Fig. 1a). The results confirmed that CCM2[0.5] fiber was composed of two phases, whereas CCM2[0.1] and CCM2[0.3] fibers were composed of a single phase.

According to these phase maps, CCM2[0.1] and CCM2[0.3] fibers were composed of only the hcp- $\epsilon$ -phase. In contrast, both the fcc- $\gamma$ -phase and hcp- $\epsilon$ -phase were observed in CCM2[0.5] fiber. The results of SEM and EBSD observations confirmed that the martensitic transformation from the fcc- $\gamma$ -phase to the hcp- $\epsilon$ -phase proceeded to completion during the fabrication of CCM2[0.1] and CCM2[0.3] fibers. The appearance of fcc- $\gamma$ -phase in CCM2[0.5] fiber implied that parts of the fcc- $\gamma$ -phase remained without martensitic transformation during and after the fiber fabrication, owing to the relatively fast growth rate. In addition, according to the growth rate dependence of the fcc- $\gamma$ -phase ratio, the fcc- $\gamma$ -phase appeared at growth rates greater than 0.5 mm/min; it increased considerably when the growth rate increased in the range of 0.5–5 mm/min and increased slightly when

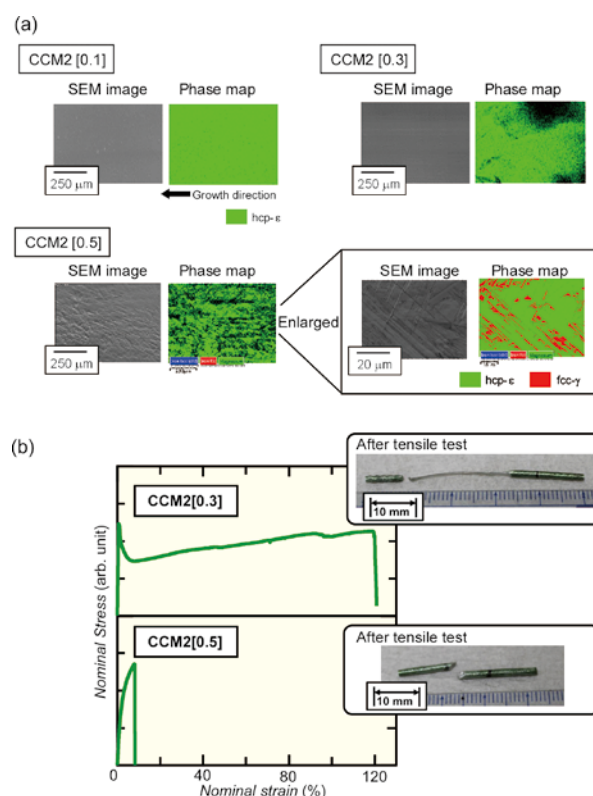


Fig.1 (a) SEM images and phase maps of CCM2 fibers, and (b) stress-strain curves of CCM2 specimens with the photographs of specimens after tensile test.

the growth rate increased in the range of 5–10 mm/min.

In the stress-strain curve of CCM2[0.5], the tensile deformation behavior was comparable to that of the CCM specimen prepared by casting (Fig. 1b). In contrast, the elongation of CCM2[0.3] was significantly higher than that of CCM2[0.5]. The elongation values of CCM2[0.3] and CCM2[0.5] were approximately 120% and 8%, respectively.

## References

- [1] Y. Yokota, T. Nihei, K. Tanaka, K. Sakairi, V. Chani, Y. Ohashi, S. Kurosawa, K. Kamada, and A. Yoshikawa, *Adv. Eng. Mater.* **20**, 1700506 (2018).
- [2] Y. Yokota, T. Nihei, S. Abe, and A. Yoshikawa, *Adv. Eng. Mater.* **23**, 2100144 (2021).

Yuui Yokota and Akira Yoshikawa (Advanced Crystal Engineering Research Laboratory)

E-mail: yui.yokota.a5@tohoku.ac.jp, akira.yoshikawa.d8@tohoku.ac.jp

URL: <http://yoshikawa-lab.imr.tohoku.ac.jp/index-e.html>

# Decoupling Between Calorimetric and Dynamical Glass Transitions in High-Entropy Metallic Glasses

Glass transition is one of the unresolved critical issues in solid-state physics and materials science. Here, we explored the correlations between the calorimetric and dynamical glass transitions of three prototypical high-entropy metallic glass systems, which present a depressed dynamical glass transition phenomenon, owing to sluggish diffusion, decreased dynamic, and spatial heterogeneities from high mixing entropy.

Metallic glasses (MGs) exhibit unique thermodynamic and dynamic characteristics, especially when approaching the glass transition temperature ( $T_g$ ). The conventional MG design strategy is based on a principal element with adding of secondary elements around the eutectic points of the phase diagrams. This restricts the discovery of MGs with divergent physical and mechanical properties. Recently, an intriguing alloy design approach was proposed [1], defined as multiple-principal-element alloys or high entropy alloys (HEAs), which exhibits great potential for developing advanced structural and functional materials. However, the core critical behaviors of HEAs, especially the effect of sluggish diffusion on the thermodynamic and dynamic properties of high entropy metallic glasses (HEMGs) have not been studied.

We utilized the strategy of equivalent substitution elements to design La(Ce)-based, Pd(Pt)-based and Ti(Zr)-based MGs and HEMGs, as model systems to investigate the high entropy effect on the structure and dynamics of glass-forming alloys [2]. The mixing entropy was  $1.38R$ ,  $1.67R$ , and  $1.57R$  (Fig. 1a) for the designed LaCe-, PdPt-, and TiZr- HEMGs, which is higher than the value generally defined as high entropy ( $1.36R$ ). Differential scanning calorimeter (DSC) traces

obtained at a heating rate of 20 K/min are shown in Fig. 1b. The obvious glass transition and crystallization signals confirm the glassy state of the three samples. Calorimetric  $T_g$  is determined from the intersection of the tangent lines of the onset of transformation and is indicated by arrows (Fig. 1b). Figure 1c presents the temperature dependence of the loss modulus of the HEMG at 1 Hz with a constant heating rate of 3 K/min (normalized by the maximum peak value). Two relaxation modes are seen, termed the  $\beta$ - and  $\alpha$ -relaxation, from low to high temperatures, respectively. Our findings indicate a decoupling between the calorimetric and dynamical glass transitions of HEMGs.

Based on the present study, the effect of high mixing entropy on the glass transition and crystallization behaviors of the representative HEMGs was proposed. It is expected that these HEA 'core effects' will benefit studies on fundamental issues, such as the glass transition, relaxations, and aging behaviors of MGs.

## References

- [1] J.-W. Yeh, S.-K. Chen, S.-J. Lin, J.-Y. Gan, T.-S. Chin, T.-T. Shun, C.-H. Tsau, and S.-Y. Chang, *Adv. Eng. Mater.* **6**(5), 299 (2004).
- [2] J. Jiang, Z. Lu, J. Shen, T. Wada, H. Kato, and M. Chen, *Nat. Commun.* **12**, 3843 (2021).

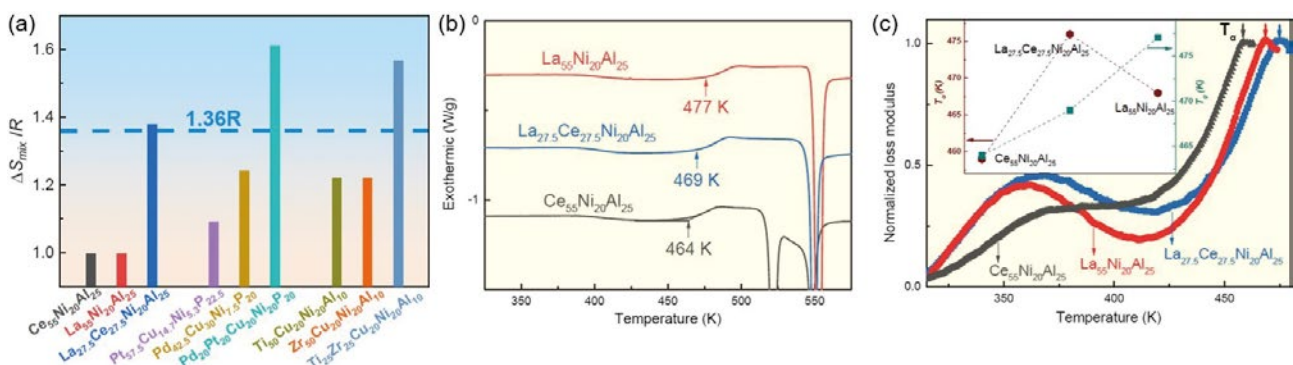


Fig. 1 The mixing of entropy, calorimetric and dynamical behaviors. (a) Calculated mixing entropies for the three MGs systems. (b) DSC traces (heating rate of 20 K/min) of the La(Ce)NiAl system, the arrows indicate the calorimetric  $T_g$ . (c) Temperature dependence of the loss modulus of the LaCe MGs system at 1 Hz with a constant heating rate of 3 K/min, normalized by the maximum peak value. The arrows indicate the  $\alpha$ -relaxation temperature ( $T_\alpha$ ), and the inset shows the evolution of  $T_g$  and  $T_\alpha$  with the components.

Hidemi Kato (Non-Equilibrium Materials Research Laboratory)

E-mail: hikato@tohoku.ac.jp

URL: <http://www.nem2.imr.tohoku.ac.jp/index-e.html>

# Mechanism of Grain Boundary Cracking in Non-Weldable Superalloy Alloy713ELC Fabricated with Powder Bed Fusion Additive Manufacturing Using an Electron Beam

Grain boundary cracking is a major problem limiting the fabrication of non-weldable superalloy with powder bed fusion additive manufacturing using an electron beam (PBF-EB). This study has revealed the cracking mechanisms and demonstrated a process-parameter-dependent cracking criterion for guiding the process design of PBF-EB to achieve crack-free samples of Alloy713ELC.

The  $\gamma'-(\text{Ni,Ti})_3\text{Al}$  precipitation-strengthened Ni-base superalloys, e.g. Alloy713ELC, are capable of serving at temperatures near their melting points and have been widely used in the hot sections of gas turbine engines. However, this class of superalloy with a high volume fraction of  $\gamma'$  precipitates is classified as non-weldable superalloy, and usually exhibits a large grain boundary (GB) cracking propensity in additive manufacturing. This has severely limited the application of powder bed fusion additive manufacturing using an electron beam (PBF-EB), which is one kind of 3D printing technology enabling near-net shaping of metallic components with complex shapes, in processing the non-weldable superalloys.

Although processing non-weldable superalloys with PBF-EB has been extensively studied in recent years, the mechanism of GB cracking is still unclear. GB cracking in non-weldable superalloy fabricated with PBF-EB is affected by the interaction of multiple factors including mechanical and compositional effects. Despite the liquation mechanism having been studied in-depth, there is not an in-depth understanding of the mechanical effect that triggers GB cracking, due to the complexity of the high-dimensional process parameter space and scan strategy in the PBF-EB process. In addition, it is necessary to correlate the GB cracking mechanisms with the criterion of non-weldability based on the content of (Al+0.8Ti).

This study [1] applied a method based on machine learning to optimize the high-dimensional PBF-EB parameter space for Alloy713ELC. This approach enabled fabricating and comparing many cracked and crack-free PBF-EB samples, which have various cracking factors and few process defects.

Although the grain refinement was considered to be effective for inhibiting GB cracking, this study indicates experimentally that fine-grained samples can be cracked, while coarse-grained samples can be crack-free. The cracking propensity in the optimized samples can be ranked by using a quasi-total plastic strain index (QTPSI), which is defined and calculated via thermo-mechanical analysis. The total plastic strain level is a critical cracking factor, and a larger scan speed tends to elevate the total plastic strain level, exhibiting a larger deviation beyond the QTPSI. In addition, through comparing Alloy713ELC with the weldable superalloy Alloy718 via thermo-mechanical analysis based on the mechanical property values measured at elevated temperatures, it was found that the non-weldability in Alloy713ELC can be attributed to its thermal expansion effect. This thermal expansion effect, combined with the liquation effect and the strain-age cracking effect, reveals the intrinsic cause of non-weldability in Alloy713ELC.

## References

- [1] Y. Lei, K. Aoyagi, K. Aota, K. Kuwabara, and A. Chiba, *Acta Mater.* **208**, 116695 (2021).

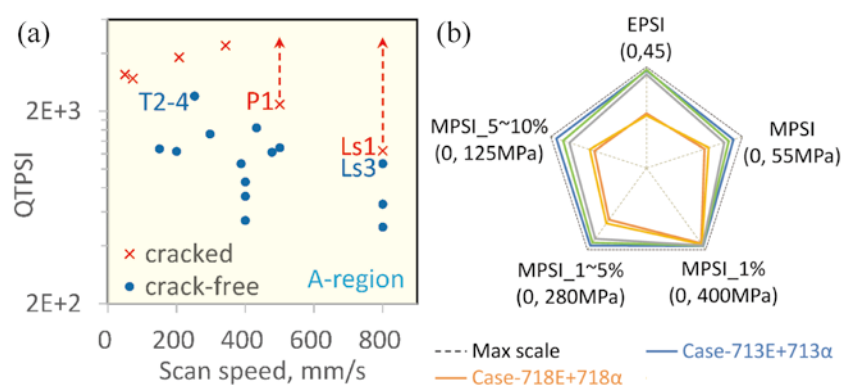


Fig. 1 (a) Cracked vs crack-free: PBF-EB samples with various QTPSI and scan speed. (b) Non-weldable Alloy713ELC vs weldable Alloy718: Five indexes calculated via thermo-mechanical analysis, reflecting the non-weldability.  $E$  and  $\alpha$  denote effective elastic modulus and thermal expansion coefficient respectively [1].

Kenta Aoyagi (Deformation Processing Research Laboratory)

E-mail: kenta.aoyagi.e7@tohoku.ac.jp

URL: <http://www.chibalab.imr.tohoku.ac.jp/english/index.html>



# Mechanism of Enhancement of Cathodoluminescence Intensity of Free Lime in Steelmaking Slag by Reheating and Quenching

We have recently developed a method to determine free lime content in steelmaking slag from the illuminated areas related to free lime in a cathodoluminescence (CL) image. To detect the illumination, the slag must be previously quenched from 1000°C to room temperature. The factors determining the enhancement of luminescence of free lime were investigated. We found that the enhancement of the CL intensity of the free lime is attributed to the increase in the oxygen vacancies by the quench.

Iron and steel manufacturing industries have aggressively tackled the reduction and reuse of byproducts to comply with current environmental regulations. The steelmaking process leads to the worldwide production of huge amounts of steelmaking slag as byproduct. Steelmaking slag has been mostly reused in road construction. Free lime in steelmaking slag causes road fracturing owing to a volumetric expansion upon reacting with the moisture and carbon dioxide in the air [1]. Thus, determining the free lime content in steelmaking slag is crucial for its safe reuse in road construction.

To meet the demand for a simple method to determine the free lime content, a method has been recently developed to rapidly derive this value by CL imaging of steelmaking slag, previously quenched from 1000°C to room temperature, according to the illuminated areas corresponding to free lime (luminescence peak at 600 nm) [2]. This quenching is required to obtain intense CL from free lime, but the mechanism of such signal enhancement is still unknown. Therefore, the present study investigated the mechanism by comparing the microstructures, CL images, and CL spectra of free lime in quenched and unquenched steelmaking slag.

A significant number of dislocations were detected in the quenched slag sample, which could be responsible for the intense luminescence at 600 nm (2.07 eV), whereas the unquenched sample, which showed no clear luminescence at 600 nm (2.07 eV), exhibited much fewer dislocations (Fig. 1). The results of this study [3] and previous reports on the luminescence of CaO suggest that the luminescence related to the free lime, which originated from  $\text{Mn}^{2+}$  ions substituting  $\text{Ca}^{2+}$  ones, is probably excited by the luminescence from oxygen vacancies ( $\text{F}^+$  center) in the free lime (Fig. 2). Therefore, the increase in oxygen vacancies enhances the intensity of this CL peak after quenching.

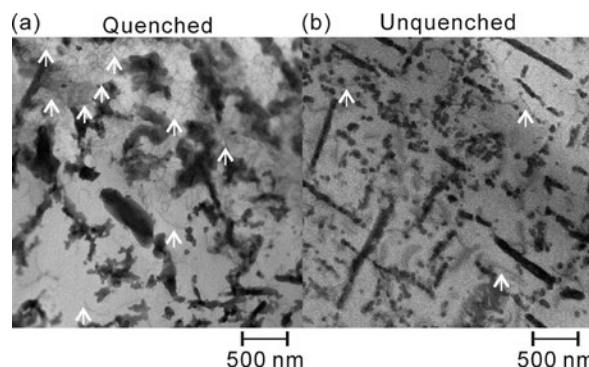


Fig. 1 Scanning transmission electron (bright field) micrographs of the cross-sections of free lime from (a) a slag sample quenched from 1000 °C and (b) an as-received one. Some of the dislocations are indicated by the arrows.

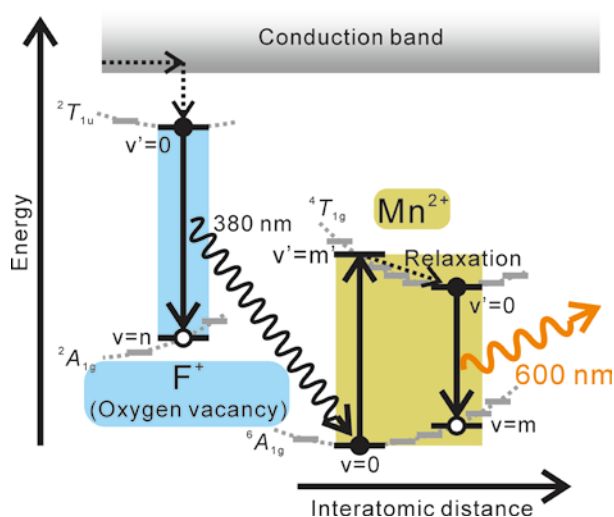


Fig. 2 Schematic diagram of the radiative transition related to luminescence from the  $\text{F}^+$  centers and  $\text{Mn}^{2+}$  ions in free lime.

## References

- [1] S. Chatterji, *Cem. Concr. Res.*, **25**, 51 (1995).
- [2] S. Imashuku and K. Wagatsuma, *Metall. Mater. Trans. B*, **51B**, 2003 (2020).
- [3] S. Imashuku, M. Nagasako, and K. Wagatsuma, *Microsc. Microanal.*, **27**, 484 (2021).

## Visible-Light–Induced Photocatalytic Activity of Nitrogen-doped TiO<sub>2</sub>

Titanium and its alloys are frequently used as biomaterials because of their good biocompatibility and high corrosion resistance. In this study, N-doped TiO<sub>2</sub> was formed on a Ti substrate, and the antibacterial activity and reactive oxygen species resulting from the visible-light–induced photocatalytic activity of the N-doped TiO<sub>2</sub> were investigated.

Titanium dioxide (TiO<sub>2</sub>) forms on surfaces of titanium (Ti) implants and plays an important role in the osseointegration between Ti and bone. Numerous studies have reported that anatase-type TiO<sub>2</sub> exhibits high photocatalytic activity; when it is irradiated with ultraviolet light, it reacts with water or O<sub>2</sub> surrounding it and generates reactive oxygen species (ROS). In addition, hydrogen peroxide (H<sub>2</sub>O<sub>2</sub>) and hydroxyl radicals are known to be generated as ROS on TiO<sub>2</sub> photocatalysts. N-doped TiO<sub>2</sub> also exhibits visible-light–induced photocatalytic activity. N-doped TiO<sub>2</sub> subjected to NaOH and hot water and heated in an ammonia (NH<sub>3</sub>) gas atmosphere showed visible-light–induced antimicrobial activity and biocalcification ability [1], [2]. We have previously investigated Cu-doped TiO<sub>2</sub> prepared by the alkaline and heat treatment of Ti metal [3].

The objective of this study is to investigate the antibacterial activity and the ROS generated via visible-light–induced photocatalytic activity on N-doped TiO<sub>2</sub>.

To prepare N-doped TiO<sub>2</sub>, we polished commercial-grade pure Ti (cp Ti) plates and soaked them in NaOH solution and hot water. These plates were subsequently heated at 600°C for 3 h under an NH<sub>3</sub> gas atmosphere in a tubular electric furnace. Measurements confirmed the formation of hydroxyl radicals. Electron-spin resonance (ESR) spectroscopy was performed to quantify the ROS.

Figure 1 shows the measurement results of hydroxyl radicals generated by the visible-light photocatalysis of cp Ti or N-doped TiO<sub>2</sub> (600°C, 3 h). The results show that more hydroxyl radicals were generated with a N-doped TiO<sub>2</sub> plate than with a cp Ti plate.

Figure 2 presents the antibacterial effect toward *Escherichia coli* (*E. coli*) of the samples of cp Ti and N-doped TiO<sub>2</sub> plates (600°C, 3 h) subjected to visible-light irradiation. The count of viable *E. coli* was much lower after the treatment with a N-doped TiO<sub>2</sub> plate than after the treatment with a cp Ti plate. A significant difference between them was inferred.

N-doped TiO<sub>2</sub> prepared in this study exhibited photocatalytic activity under visible-light irradiation,

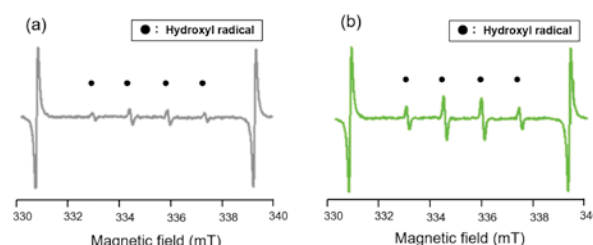


Fig. 1 ESR spectra under visible-light irradiation of (a) a pure Ti plate (cp Ti) and (b) a N-doped Ti plate (600°C, 3 h).

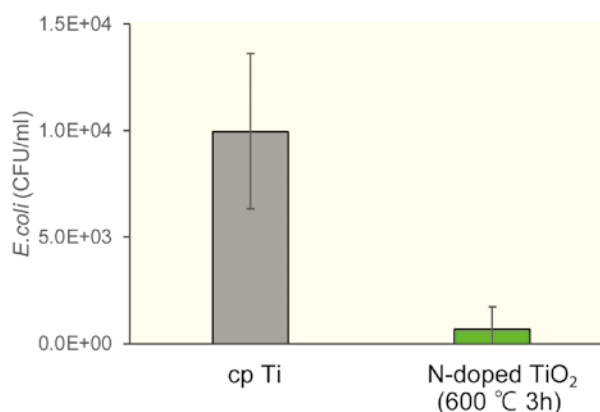


Fig. 2 Viable count of *E. coli* on cp Ti and N-doped TiO<sub>2</sub> plates (600°C, 3 h) under visible-light irradiation (mean ± standard deviation; n = 3).

and hydroxyl radicals were generated. The results suggested that ROS (especially hydroxyl radicals) generated by the photocatalytic reaction contributed to the antibacterial effects toward *E. coli*.

### References

- [1] M. Kawashita, N. Endo, T. Watanabe, T. Miyazaki, M. Furuya, K. Yokota, Y. Abiko, H. Kanetaka, and N. Takahashi, *Colloids and Surfaces, B: Biointerfaces* **145**, 285 (2016).
- [2] M. Iwatsu, H. Kanetaka, T. Mokudai, T. Ogawa, M. Kawashita, and K. Sasaki, *J. Biomed. Mater. Res. B: Applied Biomaterials* **108**(2), 451 (2020).
- [3] K. Suzuki, T. Yokoi, M. Iwatsu, M. Furuya, K. Yokota, T. Mokudai, H. Kanetaka, and M. Kawashita, *J. Asian Ceram. Soc.*, **9**(4) 1448 (2021).

Takayuki Mokudai (Design & Engineering by Joint Inverse Innovation for Materials Architecture)

E-mail: tmokudai@tohoku.ac.jp

Hidemi Kato (Project Leader of Design & Engineering by Joint Inverse Innovation for Materials Architecture)

E-mail: hidemi.kato.b7@tohoku.ac.jp

URL: <http://www.imr.tohoku.ac.jp/en/about/divisions-and-centers/research-division/29.html>

# Development of the Integrated Program for Special Education in Computational Materials Science and Human Skills Training Before/With/After COVID-19

Professional development Consortium for Computational Materials Scientists (PCoMS) supports young researchers in computational materials science (CMS) by attempting to broaden their view and extensive knowledge of interdisciplinary areas such as materials science (MS), condensed matter physics, molecular science, and materials design. Introduced below is a recent activity by key members of PCoMS. Prof. Terada and coauthors are developing an integrated program for special education in CMS and human skills and are analyzing its effectiveness.

We aim to develop the PCoMS Innovative Professional Development program and support graduate students and young researchers in materials science (MS) to help overcome the gaps between fundamental research, applied research, and practical applications.

An onsite PCoMS 3-day seminar before COVID-19 was one of the unique subjects in our program where three objectives could be achieved at once: obtain a broad knowledge of CMS; learn high-performance computing techniques, and human skills and transferable skills (HS) needed for researchers in both industry and academia [1]. In this seminar, we integrated “scientific lectures” with “HS trainings and group discussion”. The discussion about the research proposal was conducted in groups of several participants with different backgrounds, affiliations, and positions. It was required for research proposals to be related to the topics covered during the seminar and the research of each individual participant, which enabled the participants to have professional scientific discussions with other participants in different fields. On the final day, each group presented its proposal. Depending on the progress of a group discussion, we provided training on necessary human skills, such as tips for team building, methods of brainstorming, presentation tips, etc. The satisfaction of the participants for the lectures is typically low when the difficulty level of the lectures is not appropriate. However, based on surveys, we found that most participants were satisfied with group discussions, even though they think it is a difficult task. We also found that some participants believed that they did not need HS training before attending the seminar. However, after completing HS training and group discussion, they recognized the importance of improving HS. This result suggests that the integrated education program is effective in motivating participants to broaden their scientific knowledge of MS and improve their HS. Implementing such an integrated program requires the program coordinator and the

facilitator of the group discussion who have CMS expertise and human skill training knowledge. The limited implementation of such seminars is a different issue. Another finding is the importance of encouraging the participants to be active and participate in the discussion. The lecturers felt that they could convey the content sufficiently during their lecture to receive positive feedback from the participants only when there was an active discussion between the participants and the lecturers.

We are now developing the online and/or hybrid seminar with/after COVID-19 [2]. After 2020, PCoMS held only online lecture-type seminars. These online seminars attracted a wider range of participants compared to on-site seminars before COVID-19. In particular, the ratio of participants working in the industry increased. Based on a participants’ survey, we found that the satisfaction levels remained almost unchanged, regardless of the seminar format (online lecture-type seminars vs. on-site/hybrid lecture-type seminars). These results suggest that online lecture-style seminars are effective. However, there were some problems; for example, the participants had some difficulties asking questions. Furthermore, the lecturers could not gauge the level of understanding of the participants in some cases. We will need to overcome these problems and develop the materials and contents suitable for the online group discussion and HS training.

## References

- [1] Y. Terada, “Development of the short-term integrated program for engineering education and human skills training -Case study of Professional development Consortium for Computational Materials Scientists”, The 69th Japanese Society for Engineering Education Annual Conference, Sep 9, 2021.
- [2] Y. Terada, T. Kawakatsu, M. Kubo, T. Takagi, and I.-C. Chen, “Support for young researchers in computational materials science under COVID-19 -case report: seminar activities of PCoMS”, JIM Fall Meeting 2021, Sep 17, 2021.

---

Yayoi Terada (Professional development Consortium for Computational Materials Scientists)

E-mail: yayoi.terada.b8@tohoku.ac.jp

Momoji Kubo (Project Leader of Professional development Consortium for Computational Materials Scientists)

E-mail: momoji@tohoku.ac.jp

URL: [http://pcoms.imr.tohoku.ac.jp/index\\_e.html](http://pcoms.imr.tohoku.ac.jp/index_e.html)

## *Energy-Related Materials*

IMR KINKEN Research Highlights 2022





# Molecular Dynamics Simulation for High Functional Materials Design and High-Performance System

Recent materials design for high-functional materials and high-performance systems requires a deep understanding of multiphysics phenomena including chemical reaction, friction, impact, fluid, and heat. We applied our developed multiphysics computational simulator based on the molecular dynamics method and found the multiphysics phenomena contributing to materials design for mechanical engineering applications such as power plants and electronics.

High-functioning and high-performance materials are necessary for a wide variety of fields including power plants, electronics, and tribology, to addressing energy and environmental problems and for development of high-performance systems. A detailed understanding of multiphysics phenomena including chemical reactions, friction, impact, fluid, and heat, are required for design of the materials. However, traditional simulation methods such as first-principles calculations and fluid mechanics cannot simulate the above multiphysics phenomena. We therefore developed a multiphysics simulator using methods including reactive molecular dynamics, and tight-binding quantum chemical molecular dynamics (TB-QCMD), for developing next-generation materials designs [1-3].

In next-generation power plants, supercritical water (i.e., water with a temperature above 374 °C and a pressure above 22 MPa) is used to increase the energy conversion efficiency. However, supercritical water degrades body centered cubic (BCC) iron-based alloys, leading to potential dangers. To reveal the effect of supercritical water on the fracture of iron-based alloy materials, we performed a tensile simulation of BCC iron in a supercritical water environment using the reactive molecular dynamics method [1]. The results show that tensile strain along the  $[1\bar{1}0]$  direction of BCC iron may exhibit a much higher tensile strength and lower sensitivity to the environment compared with other directions. This is because yielding of iron along the  $[1\bar{1}0]$  direction originates from the homogenous generation of hexagonal close packed (HCP) precursors inside the bulk iron rather than at the surface (Fig. 1), which limits the effects of surface chemical reactions with supercritical water on the yielding behavior.

To elucidate the chemical mechanical polishing (CMP) mechanism of diamond, we performed CMP simulation of a diamond surface with OH radicals using the tight-binding quantum molecular dynamics method [2]. We clarified that the diamond CMP mechanism consists of the coupled phenomena of (i) generation and desorption of gas molecules such as CO<sub>2</sub> and H<sub>2</sub>CO<sub>3</sub> (Fig. 2b,c), and (ii) generation and removal of

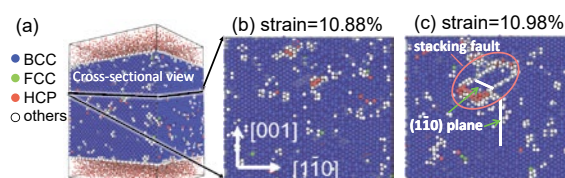


Fig. 1 Cross-sectional view of a BCC iron bulk in the supercritical water environment at strains of (a) and (b) 10.88% and (c) 10.98%.

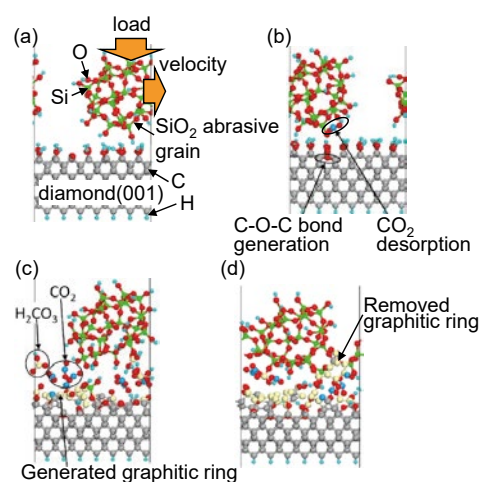


Fig. 2 Snapshots of the CMP process of the diamond (001) surface with a SiO<sub>2</sub> abrasive grain and OH radicals at (a) 0.0, (b) 16.4, (c) 317.0, and (d) 355.8 ps. The water molecules and OH radicals are not displayed for clarity.

graphitic rings (Fig. 2c,d). Based on these results, we proposed that the graphitization of the diamond surface induced by oxidation is important to improve efficiency of the diamond CMP.

## References

- [1] Q. Chen, J. Zhang, Z. Liu, Y. Wang, Y. Ootani, J. Xu, N. Ozawa, and M. Kubo, *Scr. Mater.* **202**, 113997 (2021).
- [2] K. Kawaguchi, Y. Wang, J. Xu, Y. Ootani, Y. Higuchi, N. Ozawa, and M. Kubo, *ACS Appl. Mater. Interfaces* **13**, 41231 (2021).
- [3] Y. Wang, K. Hayashi, Y. Ootani, S. Bai, T. Shimazaki, Y. Higuchi, N. Ozawa, K. Adachi, M.-I. De Barros Bouchet, J.M. Martin, and M. Kubo, *Langmuir* **37**, 6292 (2021).

Momoji Kubo (Materials Design by Computer Simulation Research Laboratory)

E-mail: momoji@tohoku.ac.jp

URL: <http://www.simulation.imr.tohoku.ac.jp/eng/index.html>

## Radiation Tolerance of ODS Alloys for Advanced Nuclear Systems

Oxide dispersion strengthened (ODS) alloys are used in advanced nuclear fission and fusion reactor systems because of their excellent radiation tolerance through the fine dispersion of nano-scale oxide particles. We found that the coarsening and/or segregation at grain boundary of Y-Zr oxide particles in the alumina scale of ODS ferritic alloy occurred after Fe-ion irradiation. Our ultra-small testing technologies have an advantage in evaluating the interfacial bonding strength of thin-coating/substrate systems, even after irradiation experiments.

Materials resistant to extreme environments, such as oxide dispersion strengthened (ODS) alloys [1,2] and ceramics [3], are crucial for realizing advanced nuclear systems.

In particular, Al-added ODS ferritic alloys have been developed as an accident-tolerant fuel cladding for commercial light water reactors, Generation IV systems, and as blanket structural materials of fusion reactors, because of their excellent high-temperature oxidation resistance through the formation of stable alumina scale. While ODS alloys are known to have superior radiation resistance against void-swelling and irradiation hardening, there have been no studies on the effect of radiation on the alumina scale formed on the Al-added ODS ferritic alloys. In this study [1], Fe-ion-irradiation experiments were performed on pre-oxidized Al-added ODS ferritic alloy. The depth profile of nanoindentation hardness in Fig.1(a) showed that irradiation softening occurred in the alumina layer. Transmission electron microscopy indicated that the Y-Zr oxide particles inside the alumina scale were coarsened and/or segregated along grain boundaries by the ion irradiation, as shown in Fig.1(b,c). This is believed to be derived from the irradiation-induced dissolution-precipitation of the Y-Zr oxide particles. Further studies are needed to clarify the stability and corrosion resistance of the alumina scale in Al-added ODS ferritic alloys under irradiation in a corrosive environment. For example, the interfacial bonding strength between alumina scale and ferritic matrix is an important factor for judging the availability in harsh

environments.

To directly evaluate the interfacial bonding strength of such a thin coating on the substrate materials, a micro-double notch shear compression test was developed and carried out on tungsten-coated ferritic steels that can be used for the inner walls of fusion reactors, as shown in Fig.1(d) [4]. Focused ion beam (FIB) and nanoindentation techniques have enabled ultra-small testing technologies (USTT) to evaluate the mechanical properties of small areas. The micrometer-size compressive specimens made by FIB were examined by micro-shear compression tests to obtain load-displacement curves. Observations of the bonding microstructure and fracture surface indicated that the obtained shear strength with  $1 \mu\text{m}^2$  specimens in their shearing plane corresponded to the interface bonding shear strength between tungsten and ferritic steel. USTTs will also help to investigate the availability of ODS ferritic alloys as a radiation-tolerant anti-corrosion material, even after irradiation experiments.

### References

- [1] H. Yu, H. Wang, S. Kondo, Y. Okuno, R. Kasada, N. Oono-Hori, and S. Ukai, *Nucl. Mater. Ener.* **29**, 101102 (2021).
- [2] Y. Liu, S. Kondo, H. Yu, K. Yabuuchi, and R. Kasada, *Nucl. Mater. Ener.* **26**, 100903 (2021).
- [3] Y. Jimba, S. Kondo, H. Yu, H. Wang, Y. Okuno, and R. Kasada, *Ceram. Inter.* **47**, 21660 (2021).
- [4] X. Wu, S. Kondo, H. Yu, Y. Okuno, M. Ando, H. Kurotaki, S. Tanaka, K. Hokamoto, R. Ochiai, S. Konishi, and R. Kasada, *Mater. Sci. & Eng. A* **826**, 141995 (2021).

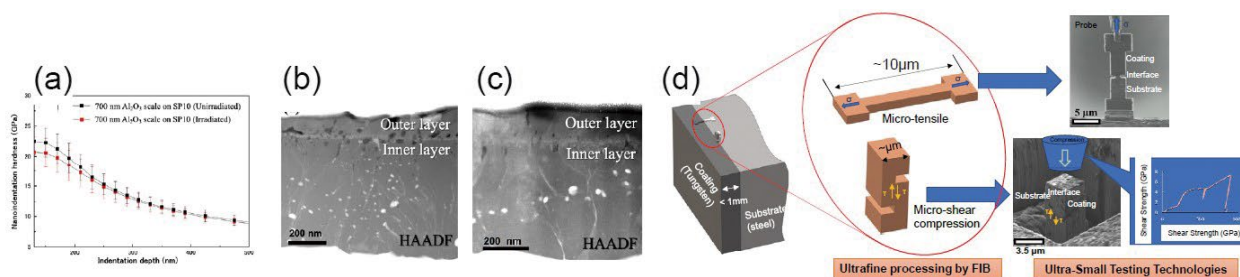


Fig.1 (a) irradiation softening of Al<sub>2</sub>O<sub>3</sub> surface layer in ODS ferritic alloy, its cross-sectional images (b) before and (c) after ion-irradiation, and (d) micro-double notch shear testing procedure for coating

Ryuta Kasada, Sosuke Kondo, Hao Yu, and Yasuki Okuno (Nuclear Materials Engineering Research Laboratory)

E-mail: ryuta.kasada.e7@tohoku.ac.jp

URL: <http://www.imr.tohoku.ac.jp/en/about/divisions-and-centers/research-division/13.html>

## ScAlMgO<sub>4</sub> as a Promising Substrate for the Epitaxial Growth of GaN

Herein, high-resolution rocking curve measurement and topography were conducted on ScAlMgO<sub>4</sub> substrates. A narrow rocking curve width of 7.2 arcsec was obtained, and the 3D-configuration of dislocations in the interior of the crystal structure was analyzed through 3D section topography. Burgers vectors of dominating dislocations with slip planes of (0001) were found to be parallel to the *a*-axis.

GaN-based thin films are promising materials for the production of a variety of energy-saving devices because the performance of these devices depends on the quality of GaN films. In this context, the homoepitaxial growth of GaN and related films on bulk GaN substrates is essential; however, the commercial availability of the substrates is limited due to the difficulties associated with growing bulk GaN crystals. Generally, epitaxial GaN film devices are fabricated on foreign substrates, such as  $\alpha$ -Al<sub>2</sub>O<sub>3</sub> and Si; however, the differences in the lattice mismatch and thermal expansion coefficients between GaN and these foreign substrates have a significant effect on the device performance. ScAlMgO<sub>4</sub> (SAM), developed by the Bell Laboratory, can be used as a substrate for GaN growth during the fabrication of blue LEDs. SAM has attracted considerable attention because of the small lattice mismatch and the small difference in thermal expansion coefficients between GaN and SAM. Recently, it was reported that high-quality SAM substrates, with a diameter of 2 inch, were grown by the Czochralski (CZ) method in Japan [1,2].

High-resolution rocking curve measurement in reflection geometry was conducted using a Ge440 (4-bounce) incident beam conditioner. A significantly narrow rocking curve width of 7.2 arcsec was obtained for the SAM 00018 reflection; this indicates the high quality of SAM wafers grown by the CZ method. Figure 1 shows a transmission XRT image for SAM 2240 reflection together with the rocking curve mapping profile. The SAM wafer can be ranked into two growth areas of the central area just below the seed crystal and the diameter-expanding area. The central part of the wafer with a diameter of 15–20 mm was free from striation patterns; however, it contained a relatively large curvature of lattice planes. This is in contrast to that observed at the outer striation-containing area. Although the relatively low spatial resolution of a digital X-ray camera did not allow us to show the details of isolated dislocations, the overall image with respect to the crystal quality and the dislocation distribution and arrays is discussed. In the central part of the wafer, striation patterns were not detected. The formation of striation patterns may be correlated with the thermal gradient environment at the onset of crystallization together with

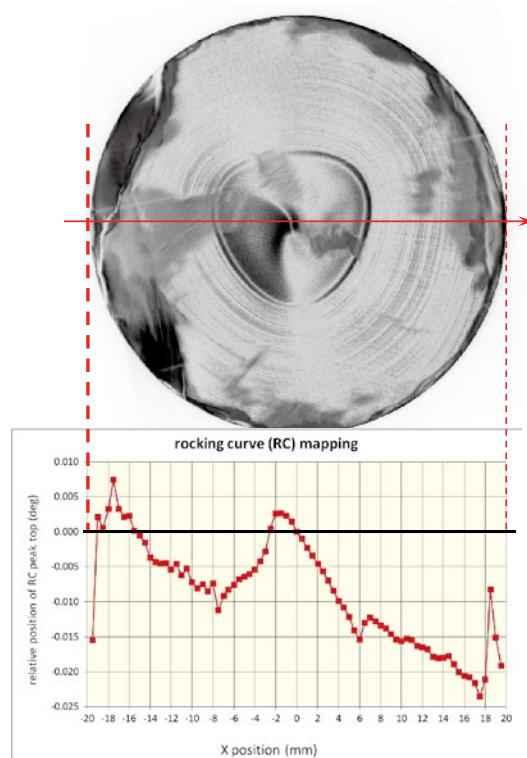


Fig. 1 Correlation of XRT image for SAM 2240 and HR-RC mapping result.

the non-stoichiometric elements absorbed at the growth front. Dark-colored regions close to the outer rim of the sample are areas that were damaged due to the grinding process during wafer fabrication. Dislocations at the striation-free central area appear to form bundles and the observed dislocation line is parallel to the  $[01\bar{1}0]$  axis. Further analysis, with respect to the XRT image for the  $03\bar{3}0$  reflection, revealed that the Burgers vectors of these dislocations are parallel to the  $[\bar{2}110]$  axis. This fact suggests that the dominant dislocations in the SAM crystal are edge-type dislocations with  $\mathbf{b} \parallel [\bar{2}110]$  slipping on the (0001) plane.

### References

- [1] K. Inaba, K. Sugiyama, T. Fujii, and T. Fukuda, *J. Cryst. Growth* **574**, 126322 (2021).
- [2] T. Fukuda, Y. Shiraishi, T. Nanto, T. Fujii, K. Sugiyama, R. Simura, H. Iechi and K. Tadamoto, *J. Cryst. Growth* **574**, 126286 (2021).

Kazumasa Sugiyama (Chemical Physics of Non-Crystalline Materials Research Laboratory)  
E-mail: kazumasa.sugiyama.e6@tohoku.ac.jp  
URL: <http://www.imr.tohoku.ac.jp/en/about/divisions-and-centers/research-division/15.html>



# Lattice-Misfit Strain Evolution at the Surface of Pt-Ni Nanoparticles During Electrochemical Reaction Detected by Bragg Coherent Diffraction Imaging

Enhancement of the sluggish oxygen reduction reaction (ORR) is required to realize efficient electrochemical devices such as fuel cells and metal-air batteries. Nanoparticles of platinum and its alloys are used as catalysts for ORR, in which elastic strain at the surface of the nanoparticles potentially enhances their catalytic activity. Strain evolution of Pt-Ni alloy nanoparticles during electrochemical operation was quantitatively examined using a novel imaging technique, Bragg coherent diffraction imaging (BCDI). The strain induced at the surface of the nanoparticles, observed in the present study, successfully explains the composition dependence of the catalytic activity of the ORR in Pt-Ni alloy.

The practical efficiency of fuel cells and metal-air batteries is impeded by the sluggish oxygen reduction reaction (ORR), in which Pt and its alloys are used as the electrochemical catalysts. In Pt-*M* (*M*: other metal elements) alloys, a nearly pure Pt "shell" is formed by dissolving the alloyed metal (*M*) from the surface of the nanoparticles during the reaction, eventually covering the surface. The catalytic activity of these particles is therefore expected to be similar to that of pure Pt. Interestingly, however, the catalytic activity of "dealloyed" Pt-*M* with a Pt shell shows better catalytic activity, which is attributed to the strain induced at the surface of the nanoparticles. Thus, it is important to reveal the strain distribution on the Pt shell in order to exploit this mechanism to design new alloy catalysts. However, evaluating the strain on the shell is challenging because it requires a technique that can image the strain field of the nanoparticles in situ.

In this study [1], details of the strain of exemplary Pt-Ni alloy nanoparticles were revealed from 3D images obtained using a novel synchrotron technique, Bragg Coherent X-ray Diffraction Imaging (BCDI) [2], which enables the detection of strain inside a particle using X-ray coherence. Pt-Ni nanoparticles with compositions of Pt<sub>2</sub>Ni<sub>3</sub> (Ni-rich), Pt<sub>1</sub>Ni<sub>1</sub> (moderate Ni), and Pt<sub>3</sub>Ni<sub>2</sub> (Ni-poor) were observed by BCDI during cyclic voltammetry cycles, in which the less noble metal Ni is known to dissolve electrochemically from the surface. The evolution of tensile strain inside the particles was observed in all the compositions, strongly indicating the formation of a Pt shell on the surface to mitigate the overall internal stress by utilizing the lattice mismatch between the Pt-Ni core and Pt shell. Thus, a core-shell elastic model was used to evaluate the strain in the Pt shell based on the parameters obtained from

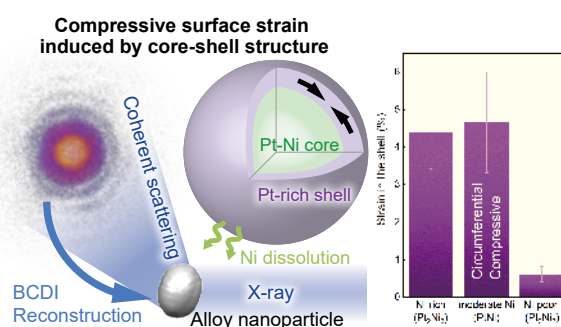


Fig. 1 A schematic of Bragg coherent diffraction imaging and core-shell Pt-Ni alloy nanoparticle (left). Observed compressive strain in the Pt-shell (right) [1]

the 3D images.

Compressive circumferential strain in the shell was observed for all compositions. The Pt<sub>2</sub>Ni<sub>3</sub> particles exhibited the largest compressive circumferential strain of 5%. Since it was reported that compressive strain facilitates ORR [3], this is in excellent agreement with the previously reported composition dependence of the catalytic activity of nm-sized particles among a wide range of compositions.

The present study demonstrated that BCDI enables quantitative determination of the strain on alloy nanoparticles during electrochemical reactions, which will eventually lead to rational catalyst design by exploiting the strain-induced enhancement of the catalytic activity in a wide range of electrocatalysts.

## References

- [1] T. Kawaguchi, V. Komanicky, V. Latyshev, W. Cha, E. R. Maxey, R. Harder, T. Ichitsubo, and H. You, *Nano Lett.* **21**, 5945 (2021).
- [2] I. Robinson and R. Harder, *Nat. Mater.* **8**, 291 (2009).
- [3] P. Strasser et al., *Nat. Chem.* **2**, 454 (2010).

Tetsu Ichitsubo, Norihiko L. Okamoto, Hiroshi Tanimura, Tomoya Kawaguchi, and Hongyi Li (Structure-Controlled Functional Materials Research Laboratory)

E-mail: tichi@tohoku.ac.jp

URL: <http://ilab.imr.tohoku.ac.jp>

## Enhanced Anomalous Nernst Effect in Ni/Pt Epitaxial Superlattice

The anomalous Nernst effect (ANE), where the electric field appears in the cross-product direction of magnetization and temperature gradient in a magnet, has attracted considerable attention as an environmentally-friendly technology for energy harvesting. We found an enhancement of ANE in metallic superlattices consisting of Ni and Pt layers, and revealed that the large transverse thermoelectric conductivity plays a major role in the enhanced ANE.

Spin caloritronics, the research field of the interconversion between charge current ( $\mathbf{J}_c$ ) and heat current ( $\mathbf{J}_q$ ) mediated by spin current ( $\mathbf{J}_s$ ) and/or magnetization ( $\mathbf{M}$ ), has attracted much attention not only for academic interest but also for practical applications. Newly discovered spin caloritronic phenomena have stimulated renewed interest in the thermoelectric phenomena in ferromagnets. One of the thermoelectric phenomena in ferromagnets is the anomalous Nernst effect (ANE), in which  $\mathbf{J}_c$  appears in the cross-product direction of  $\mathbf{M}$  and the temperature gradient ( $\nabla T$ ). Although ANE has been known for a long time, the microscopic physical picture of ANE has not been fully understood. In addition to the fundamental point of view, this magneto-thermoelectric effect may be beneficial for thermoelectric conversion applications. The key to ANE-based thermoelectric conversion is to find a material with a large anomalous Nernst coefficient ( $S^{\text{ANE}}$ ).

We previously reported the enhancement of ANE in Fe-based metallic multilayers [1], implying that the low dimensionality of the layer and/or the existence of an interface plays a role in the increase in ANE. This suggests that metallic multilayers or superlattices with a number of interfaces are promising for achieving a large ANE.

Here, we focus on the combination of ferromagnetic Ni and paramagnetic Pt because Ni is an interesting material for ANE [2] and Pt is a representative paramagnet with a large spin-orbit interaction. Perpendicularly magnetized Ni/Pt (001) epitaxial superlattices were fabricated directly on a non-conductive  $\text{SrTiO}_3$  substrate [3], and the Ni layer thickness dependence of ANE was investigated for  $[\text{Ni} (t \text{ nm}) / \text{Pt} (1.0 \text{ nm})]_x \text{N}$ .

Figure 1a shows the measurement setup for the ANE. By heating one side of the substrate,  $\nabla T$  was induced along the in-plane  $x$  direction. An external magnetic field ( $H$ ) was applied along the out-of-plane  $z$  direction. As a result, the electric field of the ANE ( $E_{\text{ANE}}$ ) was detected along the  $y$ -direction. Figure 1b shows the  $H$  dependence of the  $E_{\text{ANE}}$  divided by  $\nabla T$  for  $t = 3.0 \text{ nm}$ . A square-shaped

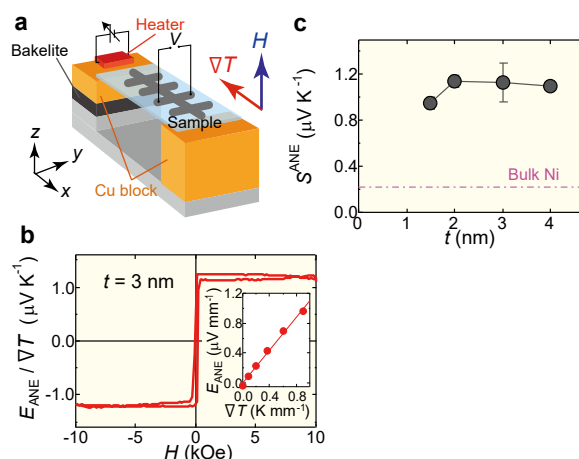


Fig.1 (a) Measurement setup for ANE. (b)  $H$  dependence of  $E_{\text{ANE}}$  divided by  $\nabla T$  for  $[\text{Ni} (t \text{ nm}) / \text{Pt} (1.0 \text{ nm})]$  superlattice with  $t = 3.0 \text{ nm}$ . Inset: the plot of  $E_{\text{ANE}}$  as a function of  $\nabla T$ . (c)  $t$  dependence of  $S^{\text{ANE}}$ .

hysteresis of  $E_{\text{ANE}} / \nabla T$  was observed.  $S^{\text{ANE}}$  was calculated from the slope of the linear fit to  $E_{\text{ANE}}$  as a function of  $\nabla T$ . Figure 1c shows the  $t$  dependence of  $S^{\text{ANE}}$ . All the samples exhibited large values of  $S^{\text{ANE}} \geq 0.9 \mu\text{V K}^{-1}$ , and the maximum  $S^{\text{ANE}} = 1.14 \pm 0.05 \mu\text{V K}^{-1}$  was obtained at  $t = 2.0 \text{ nm}$ . It is noted that the  $S^{\text{ANE}}$  for the Ni/Pt superlattice is one order of magnitude larger than that for bulk Ni [2]. From a detailed investigation, the enhanced ANE is attributable to the large transverse thermoelectric conductivity. We successfully demonstrated the enhancement of the ANE owing to the formation of Ni/Pt superlattices [4].

### References

- [1] K. Uchida, T. Kikkawa, T. Seki, T. Oyake, J. Shiomi, Z. Qiu, K. Takanashi and E. Saitoh, *Phys. Rev. B* **92**, 094414 (2015).
- [2] A. Miura, R. Iguchi, T. Seki, K. Takanashi, and K. Uchida, *Phys. Rev. Mater.* **4**, 034409 (2020).
- [3] T. Seki, M. Tsujikawa, K. Ito, K. Uchida, H. Kurebayashi, M. Shirai, and K. Takanashi, *Phys. Rev. Mater.* **4**, 064413 (2020).
- [4] T. Seki, Y. Sakuraba, K. Masuda, A. Miura, M. Tsujikawa, K. Uchida, T. Kubota, Y. Miura, M. Shirai, and K. Takanashi, *Phys. Rev. B* **103**, L020402 (2021).

Koki Takanashi and Takeshi Seki (Magnetic Materials Research Laboratory)

E-mail: koki.takanashi.d2@tohoku.ac.jp, takeshi.seki@tohoku.ac.jp

URL: <http://magmatelab.imr.tohoku.ac.jp/>

# Complex Hydride-Based Electrolyte with Hydrogen Cluster Anion for Room-Temperature Calcium Rechargeable Battery

Calcium batteries are cost effective and possess high battery performance, making them a suitable substitute for Li-batteries. Still, many challenges remain before calcium batteries can be realized due to a lack of suitable electrolytes with reductive/oxidative stability and high ionic conductivity. In this study, we developed a new fluorine-free calcium electrolyte based on a hydrogen cluster (monocarborane) anion that could potentially realize rechargeable calcium batteries.

Current Li-ion batteries with high energy densities are indispensable in applications such as portable electronic devices, electric vehicles, and grid-scale storage. However, they are approaching their limits of theoretical energy density and cost, and Li is not naturally plentiful. Ca is the fifth most abundant element in the Earth's crust and its metal anode has a low reduction potential ( $-2.87$  V vs. SHE) and high volumetric capacities of  $2072 \text{ mAh cm}^{-3}$ , giving it a comparable cell voltage and energy density to that of Li. Ca batteries are therefore cost effective and possess high battery performance, making them a suitable substitute for Li-batteries [1].

Still, many challenges remain before Ca batteries can be realized due to a lack of suitable electrolytes which possess reductive/oxidative stability and high ionic conductivity. Moreover, realizing a fluorine-free system is desirable for practical Ca electrolytes because a fluorine-containing electrolyte intrinsically induces  $\text{CaF}_2$  formation on the electrode, which hinders Ca diffusion as well as the Ca plating and stripping processes.

In this study, we developed a highly stable and efficient fluorine-free Ca electrolyte of  $\text{Ca}[\text{CB}_{11}\text{H}_{12}]_2$  based on a hydrogen cluster (monocarborane, complex hydride) anion (Fig. 1a) for room-temperature Ca batteries [2]. The hydrogen cluster anion is known as a weakly coordinating anion with high reductive and oxidative stabilities, indicating that an electrolyte with the anion could also be highly compatible with Ca batteries [3]. The  $\text{Ca}[\text{CB}_{11}\text{H}_{12}]_2$ , which was successfully prepared via simple cation exchange and heating processes, exhibited low solubilities in tetrahydrofuran (THF) and 1,2-dimethoxyethane (DME), but high solubility in the mixed solvent of DME/THF. The  $0.5 \text{ M}$   $\text{Ca}[\text{CB}_{11}\text{H}_{12}]_2$  electrolyte showed the most promising electrochemical performances, viz., a high conductivity, wide potential window, and reversible Ca plating/stripping behavior with high Coulombic efficiency (Fig. 1b). In a feasibility study, we used the this electrolyte in a Ca battery with a sulfur cathode exhibiting reversible discharge and charge abilities, demonstrating that the  $\text{Ca}[\text{CB}_{11}\text{H}_{12}]_2$  electrolyte is compatible with a Ca battery system.

The development of a promising electrolyte candidate based on complex hydrides compatible with

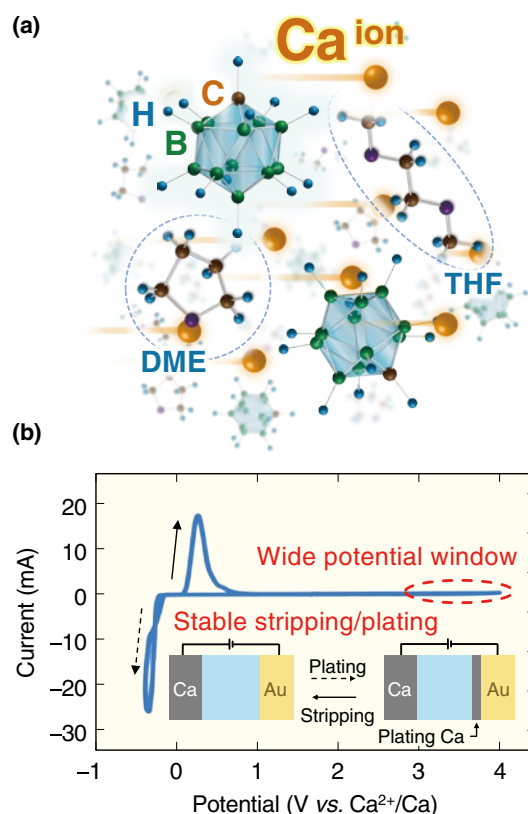


Fig. 1 (a) Graphical image of the new developed calcium battery electrolyte  $\text{Ca}[\text{CB}_{11}\text{H}_{12}]_2$  in DME/THF, (b) Cyclic voltammograms of Ca plating/stripping with a three-electrode setup at room temperature with graphical image of Ca plating/stripping (inset).

Ca batteries will create future opportunities for exploring other related complex hydride compounds. In addition, the absence of fluorine and  $\text{CaF}_2$  formation in these materials will pave the way for achieving high cyclability in Ca batteries.

## References

- [1] M. E. Arroyo-de Dompablo, A. Ponrouch, P. Johansson, and M. R. Palacin, *Chem. Rev.* **120**, 6331 (2020).
- [2] K. Kisu, S. Kim, T. Shinohara, K. Zhao, A. Zuttel, and S. Orimo, *Sci. Rep.* **11**, 7563 (2021).
- [3] R. Mohtadi and S. Orimo, *Nat. Rev. Mater.* **2**, 16091 (2017).

Kazuaki Kisu and Shin-ichi Orimo (Hydrogen Functional Materials Research Laboratory)

E-mail: kazuaki.kisu.b2@tohoku.ac.jp

URL: <http://www.hydrogen.imr.tohoku.ac.jp/en/index.html>



## *Electronic Materials*

IMR KINKEN Research Highlights 2022





## Exotic Pairing States in a Spin-Polarized Quantum-Hall Insulator

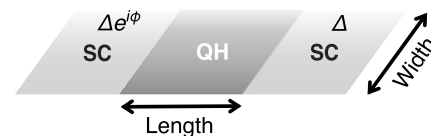
Emergent physics appears in hybrid systems composed of differently ordered materials. For Cooper pairs, a heterojunction of a quantum Hall insulator and a conventional superconductor is an unusual environment, which leads them to have exotic pairing symmetry. Our study revealed possible pairing states induced in the metallic edge of a spin-polarized quantum Hall insulator and showed that these pairing states can be detected via the Josephson effect.

Topological orders and topological phases are a field of current active research in condensed matter physics. The quantum Hall effect is a prominent example of a phenomenon associated with topological materials and is realized in a two-dimensional electronic system subject to a strong magnetic field. The most remarkable behavior of the electronic states in topological materials appears at the edge or surface. A quantum Hall system has metallic edge states, where electrons flow unidirectionally, while the bulk is an insulator.

The surface or edge states of topological materials such as topological insulators and quantum spin Hall insulators can be engineered by attaching conventionally ordered materials, e.g., superconductors and ferromagnets. Unlike these examples, it is known that the edge states of quantum Hall insulators are less affected by attached materials due to the unidirectional flow. Based on this, our study focuses on the electronic behavior at the interface between a spin-polarized quantum Hall insulator and a superconductor from the perspective of pairing symmetry.

Superconductivity is categorized by the symmetry of Cooper pairs. In general, this property is intrinsic to materials. However, a junction with non-superconducting materials can transform pairing symmetry depending on the electronic structure of the materials. We showed that Cooper pairs induced in a spin-polarized quantum Hall edge are (i) spin-triplet, (ii) a combination of even- and odd-frequency components, and (iii) have a finite momentum [1].

These exotic pairing states can be confirmed via the Josephson effect. The spin-triplet pairing can be detected by the sensitivity to the interface magnetization. In addition, the momentum of Cooper pairs can be detected by the vanishing of the critical current, which is defined by the maximum Josephson current. The critical current vanishes when the Cooper pair momentum  $2k_F$  is commensurate with the length of the interface (= the junction width).



By the rotation of the interface magnetization, the current-phase relation is shifted as

$$I(\phi) = I_c \sin(\phi + \pi) \rightarrow I_c \sin \phi$$

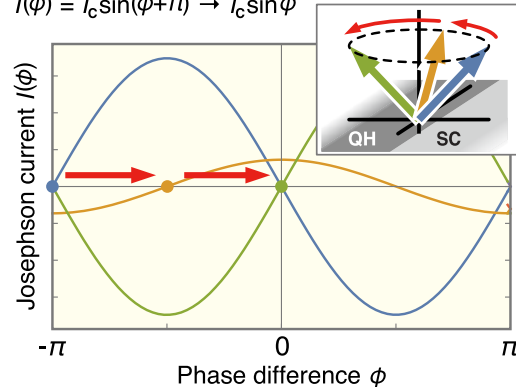


Fig. 1 The geometry of the Josephson junction (top) and detection of the triplet Cooper pairing (bottom).

The critical current vanishes when the Cooper pair momentum  $2k_F$  is commensurate with the sample width  $W$ .

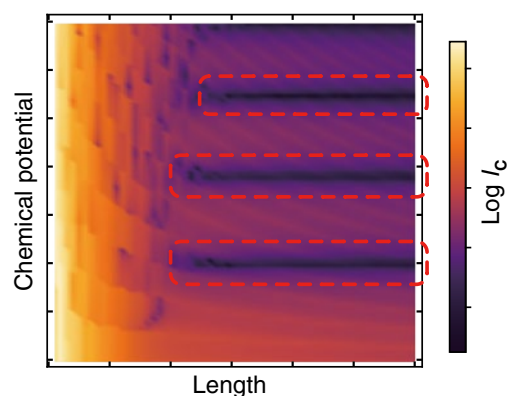


Fig. 2 Detection of the Cooper pair momentum by the vanishing critical current.

### References

- [1] R. Nakai, K. Nomura, and Y. Tanaka, *Phys. Rev. B* **103**, 184509 (2021).

Kentaro Nomura and Ryota Nakai (Theory of Solid State Physics Research Laboratory)

E-mail: ryota.nakai.b6@tohoku.ac.jp

URL: [http://www.bauer-lab.imr.tohoku.ac.jp/home\\_en.html](http://www.bauer-lab.imr.tohoku.ac.jp/home_en.html)

# Twin Boundary Formation at Grain-boundary Groove During Directional Solidification of Compound Semiconductor InSb

The formation of twin boundaries at the grain-boundary groove of InSb was experimentally observed in situ. It was shown that the twin boundaries are generated when rapid growth occurs at the grain-boundary groove bounded by facet planes. By calculating the relationship between the probability of twinning and the degree of undercooling required for twinning, we proved that the twin nucleation in InSb occurs preferentially at the bottom of the grain-boundary groove.

Formation of twin boundaries is detrimental in both bulk single-crystal growth and bulk poly-crystal growth of semiconductors, because the density of grain boundaries in the crystal significantly influences the quality of substrates cut from a bulk crystal. Recently, in the directional growth of Si, it was observed that a faceted groove formed at the junction of a crystal-melt interface and a grain boundary, and that twin nucleation occurred at the bottom of the grain-boundary groove [1,2]. A twinning model at the grain-boundary groove has also been proposed [3]. While the occurrence of twinning at the grain-boundary groove during solidification of Si has been discussed, twinning during the solidification of compound semiconductors has been less studied. In this study, to understand the effect of the grain-boundary groove on twinning during the solidification of compound semiconductor, we observed a crystal-melt interface of InSb [4].

Figure 1(a) shows the crystal-melt interface during directional solidification of InSb. It was clearly observed that a groove bounded by facet planes was formed at the crystal-melt interface due to the existence of a grain boundary. The depth of the groove increased with time. When the depth of the groove reached approximately 100  $\mu\text{m}$ , the groove was filled by the rapid growth. This shows that the

degree of undercooling in the groove was large locally. We confirmed that twin boundaries were formed during this process, as schematically shown in Fig. 1(b). We calculated the probability of twin nucleation  $P_{\text{twin}}$  at the grain-boundary groove as a function of undercooling  $\Delta T$ . We assumed simultaneous multiple nucleation at the groove as illustrated in Fig. 1(c). As seen in Fig. 1(d),  $\Delta T$  at  $P_{\text{twin}} = 10^{-6}$  for  $N = 2, 5$  and  $30$  is calculated as 16.6 K, 7.0 K and 2.3 K, respectively. For  $N = 5$ ,  $P_{\text{twin}}$  becomes  $3 \times 10^{-6}$  at  $\Delta T = 7.0$  K, which is 100 times the value at  $\Delta T = 6.9$  K. This means that a difference of 0.1 K in  $\Delta T$  significantly influences the twinning probability.

In summary, we showed that preferential twin nucleation in InSb occurs at the bottom of grain-boundary grooves.

## References

- [1] M.G. Tsoutsouva, T. Riberi-Béridot, G. Regula, G. Reinhart, J. Baruchel, F. Guittonneau, L. Barrallier, and N. Mangelinck-Noël, *Acta Mater.* **115**, 210 (2016).
- [2] K. Fujiwara, R. Maeda, K. Maeda, and H. Morito, *Scr. Mater.* **133**, 65 (2017).
- [3] T. Duffar and A. Nadri, *Scr. Mater.* **62**, 955 (2010).
- [4] K. Shiga, A. Takahashi, L.-C. Chuang, K. Maeda, H. Morito, and K. Fujiwara, *J. Crystal Growth* **577**, 126403 (2022).

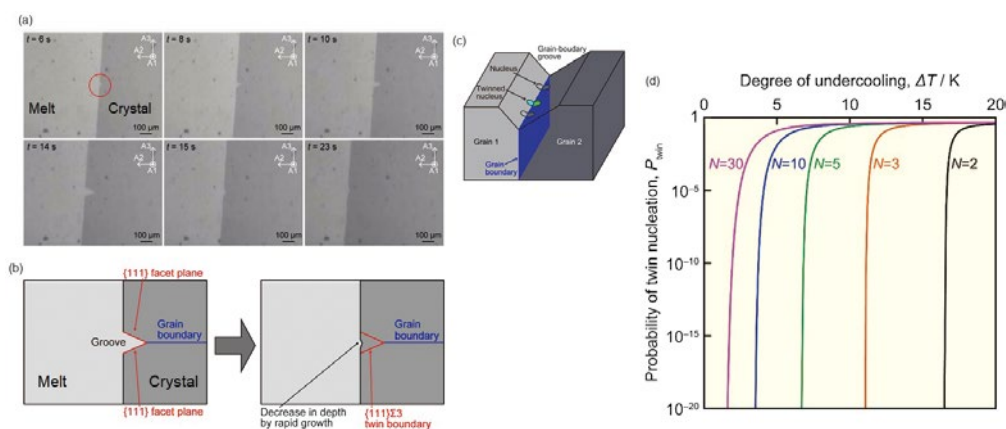


Fig. 1 (a) Snapshots of the crystal/melt interface of InSb, (b) schematic illustration of twin boundary formation at the groove, (c) twinning model at the groove, and (d) calculating results of twin nucleation probability.

Kozo Fujiwara (Crystal Physics Research Laboratory)

E-mail: kozo.fujiwara.c6@tohoku.ac.jp

URL: <http://www.imr.tohoku.ac.jp/en/about/divisions-and-centers/research-division/02.html>



## Study of Strong Magnon-Magnon Coupling in High Magnetic Field

Light-matter objects with strong coupling interactions provide a unique platform for studying quantum vacuum phenomena. The mode-mode interaction of magnons can be a good model for such strong coupling systems. One of the unique features of this system is the tuning of the modes using strong magnetic fields. A THz spectrometer combined with a compact pulsed magnetic field generator enables systematic investigation of such systems.

The interaction between matter and light can be enhanced in condensed matter systems by strong many-body correlations, which couple a large number of dipolar moments with light. Owing to this enhancement, the interaction between light and matter may be as large as the frequency of the light itself, and such a state is called an ultra-strong coupling regime. In this area, the anti-resonant interaction is expected to be non-negligible. However, research on these systems is limited. One of the difficulties is finding a system with dominant anti-resonant interactions. In addition, the interactions must be tuned experimentally.

Recently, we found that the canted antiferromagnet  $\text{YFeO}_3$  is a good model material for such a strong coupling system, based on terahertz magneto-spectroscopy in a strong magnetic field [1]. The advantage of this system is that the vacuum Rabi splitting and vacuum Bloch-Siegert shift can be tuned by a magnetic field. In this study, the magnons, especially the coupling between different modes in  $\text{YFeO}_3$ , were experimentally investigated using THz time-domain magneto-spectroscopy.

Two unique experimental techniques were combined, namely single-shot THz detection and a tabletop 30T pulse high magnetic field generator. The tabletop magnet was developed by the Magnetism Research Division of the Institute for Materials Research. It can generate 30T by combining a small capacitor bank power supply and a mini coil. Unlike THz spectrometers that use large superconducting magnets, it has the advantage of being able to use direct optics that are needed for high precision THz spectroscopy. An overview of the instrument is shown in Fig. 1.

$\text{YFeO}_3$  exhibited an antiferromagnetic structure with a propagation vector along the  $a$ -axis. The weak ferromagnetic component is caused by the small canting along the  $c$ -axis.

We found that two peaks with different splitting and intensity ratio appeared when the magnetic field was tilted from the  $c$ -axis. These two peaks, termed the upper and lower modes, are caused by

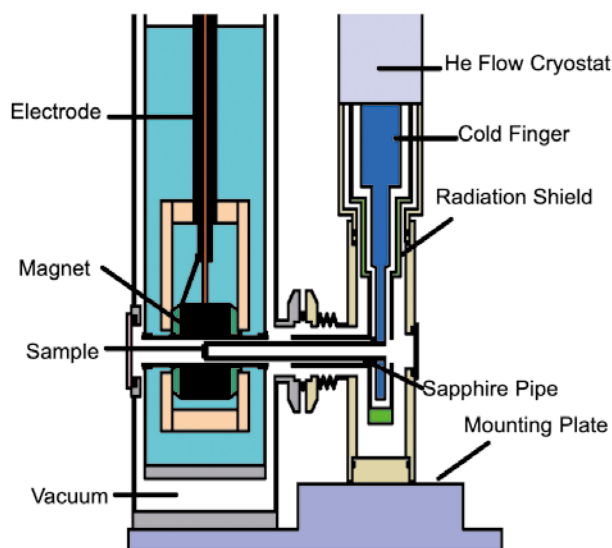


Fig. 1 Schematic view of the tabletop magnet

the hybridization of quasi-ferromagnetic and quasi-antiferromagnetic modes. This major behavior of the anti-crossing can be reproduced by the Landau-Lifshitz-Gilbert equation except for the anomalous large redshift found in the upper frequency mode. Specifically, the frequency of the upper mode is smaller than that of the quasi-antiferromagnetic mode. This shift is the direct consequence of the counter-rotating term.

The full features of the spectra can be reproduced by the Hopfield-like quantum mechanical Hamiltonian with variable co-rotating and counter-rotating coupling strength. We found that the counter-rotating term is dominant, and the simple rotating wave approximation breaks down in the present system. As a result, an exotic behavior such as two-modes vacuum squeezing of the ground state is realized.

### References

- [1] T. Makihara *et al.*, Nat. Commun. **12**, 3115 (2021).

Hiroyuki Nojiri (Magnetism Research Laboratory)

E-mail: hiroyuki.nojiri.e8@tohoku.ac.jp

URL: <http://www.hfpm.imr.tohoku.ac.jp>

## Compact Three-Dimensional Magnetic-Field Sensor

Magnetic-field sensing in three-dimensional (3D) space is one of the essential technologies in automatic vehicle and robotics. We have succeeded in detection of the 3D magnetic-field vectors with a planar-type single Fe-Sn device, where anomalous Hall effect, anisotropic magnetoresistance, and unidirectional magnetoresistance are complementarily functionalized. Demonstration of a compact 3D sensor will contribute to the future of the Internet-of-Things.

Some nanocrystalline or amorphous metal alloys exhibit significant electronic and magnetic properties, as exemplified in high permeability magnets. In this study, we successfully demonstrated three-dimensional (3D) magnetic-field sensing in the nanocrystalline ferromagnetic Fe-Sn thin-film device. Thanks to the use of non-toxic elements and a simple device structure, environmental-friendly and compact 3D sensors based on Fe-Sn films can be implemented for use in various devices.

The demand of magnetic-field sensing technique is increasing in the developing internet-of-things (IoT) society. In particular, 3D detection of the magnetic-field vector ( $\mathbf{H}$ ) is highly desirable for automatic control of objects by determining their position, velocity, and rotation angle [Fig. 1(a)]. Commercially available magnetic sensors such as semiconductor Hall sensors or magnetoresistance sensors generate the output signal against the scalar quantity of  $\mathbf{H}$  along a principal direction. Therefore, to detect the 3D direction of  $\mathbf{H}$ , it is necessary to place three magnetic sensors along the X, Y, and Z directions. By contrast, a planar-type single Fe-Sn Hall sensor [Fig. 1(b)] can detect the 3D direction of  $\mathbf{H}$  [1]. A large anomalous Hall effect (AHE) is utilized for detecting the polar angle ( $\theta_H$ ) of  $\mathbf{H}$  in a similar manner to a semiconductor device [2,3]. The magnetic Fe-Sn sensor has an additional ability not seen in semiconductor devices, to detect the magnetic field through the anisotropic magnetoresistance (AMR) and an unexpectedly large unidirectional magnetoresistance (UMR), where the AMR and UMR show  $180^\circ$  and  $360^\circ$  periodic functions of azimuthal angle ( $\phi_H$ ) of  $\mathbf{H}$ , respectively. By combining AHE, AMR, and UMR, individual and simultaneous determination of the 3D direction of  $\mathbf{H}$  in orthogonal rotation was demonstrated, as shown in Fig. 1(c).

Further improvement of the sensing performance is expected by Fermi-level tuning via impurity doping [4] or device structure design [5]. Determination of  $\mathbf{H}$  in the 3D space with a planar-type simple device geometry would accelerate the miniaturization of 3D magnetic sensors, which would

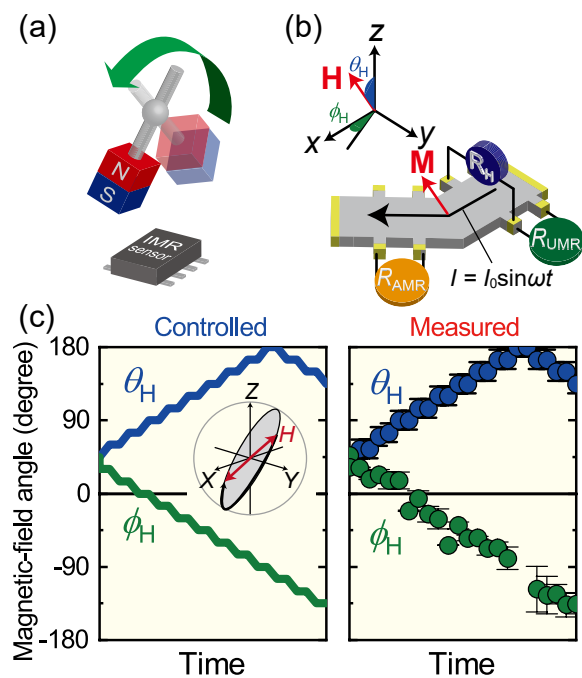


Fig. 1 (a) Schematic of the device operation. (b) Schematic of the planar-type Fe-Sn Hall-bar sensor, where Hall resistance ( $R_H$ ), anisotropic magnetoresistance ( $R_{AMR}$ ), and unidirectional magnetoresistance ( $R_{UMR}$ ), which depends on magnetization vector ( $\mathbf{M}$ ), are simultaneously measured for determination of the vector ( $\mathbf{H}(\theta_H, \phi_H)$ ). (c) Demonstration of detection of magnetic-field angles  $\theta_H$  and  $\phi_H$ .

in turn contribute to the development of IoT devices composed of large numbers of sensors.

### References

- [1] J. Shiogai, K. Fujiwara, T. Nojima, and A. Tsukazaki, *Commun. Mater.* **2**, 102 (2021).
- [2] Y. Satake, K. Fujiwara, J. Shiogai, T. Seki, and A. Tsukazaki, *Sci. Rep.* **9**, 3282 (2019).
- [3] J. Shiogai, Z. Jin, Y. Satake, K. Fujiwara, and A. Tsukazaki, *Appl. Phys. Express* **12**, 123001 (2019).
- [4] K. Fujiwara, Y. Satake, J. Shiogai, and A. Tsukazaki, *APL Materials* **7**, 111103 (2019).
- [5] J. Shiogai, Z. Jin, Y. Satake, K. Fujiwara, and A. Tsukazaki, *Jpn. J. Appl. Phys.*, (2021) in press.

Junichi Shiogai (Low Temperature Physics Research Laboratory)

E-mail: junichi.shiogai@tohoku.ac.jp

URL: [http://mu.imr.tohoku.ac.jp/index\\_en.html](http://mu.imr.tohoku.ac.jp/index_en.html)

# Charge Ordering and $\pi$ -d Interaction in Electron-Doped 3/4-Filling Molecular System $\alpha''$ -(BEDT-TTF)<sub>2</sub>Rb<sub>2x</sub>Co(SCN)<sub>4</sub> ( $x = 0.6$ )

Charge ordering and band-filling control have been intensively investigated in strongly correlated electron systems. In organic molecular systems, however, band-filling control is usually difficult and is not yet fully understood. Here, we describe a new two-dimensional organic crystal with an intermediate value of band filling. Transport and infrared optical measurements revealed that this compound transits to a charge-ordered state at 100 K, which is the lowest among the isomorphous compounds with commensurate values of band filling.

Two-dimensional organic molecular crystals (BEDT-TTF)<sub>2</sub>X, where BEDT-TTF is bis(ethylenedithio)tetrathiafulvalene and X is an anion, often show insulating states due to the electron correlation. Since X is typically monovalent, the hole filling of the BEDT-TTF molecular band becomes quarter-filled and charge ordering is expected to emerge. Among such materials,  $\theta$ -type crystals  $\theta$ -(BEDT-TTF)<sub>2</sub>AM(SCN)<sub>4</sub> (where A is an alkaline ion, and M is a divalent metal ion) are well studied charge-ordering systems.

In charge-ordering systems, the band filling is an important parameter for the stability of charge ordering. Thus, filling control by chemical doping is the predominant method for studying the charge order e.g., in transition-metal oxides. However, this method is difficult for organic molecular systems, since the impurities tend to be excluded from the crystal during the crystal growing procedure. Only a few crystals with an intermediate band-filling value are known.  $\alpha''$ -(BEDT-TTF)<sub>2</sub>AM(SCN)<sub>4</sub> system (AM = K<sub>1.4</sub>Co ( $\alpha''$ -K<sub>1.4</sub>Co), CsHg ( $\alpha''$ -CsHg)) is one of the candidates for studying the band-filling control of molecular crystals. The above two compounds transit from metal to insulator at low temperatures. The transition temperature of  $\alpha''$ -K<sub>1.4</sub>Co is lower than that of  $\alpha''$ -CsHg, suggesting the instability of charge ordering. A compound with a band-filling value intermediate between these is desirable.

In the course of studying the charge ordering in organic molecular systems, we found a new compound  $\alpha''$ -(BEDT-TTF)<sub>2</sub>Rb<sub>2x</sub>Co(SCN)<sub>4</sub> ( $\alpha''$ -Rb<sub>2x</sub>Co) [1]. From the x-ray diffraction and energy dispersive x-ray spectroscopy measurements, Rb site occupancy  $x$  was determined to be about 0.6 (Fig.1(a)). Thus, we found that  $\alpha''$ -Rb<sub>1.2</sub>Co has an intermediate band-filling value between those of  $\alpha''$ -K<sub>1.4</sub>Co and  $\alpha''$ -CsHg and an intermediate dihedral angle ( $\theta$ ) between two adjacent molecules (see. Fig. 1(b)). This compound also shows metal-insulator transition at about 100 K (Fig.1(c)), similar to the above two compounds. However, the transition temperature is lower. This can be expected from the

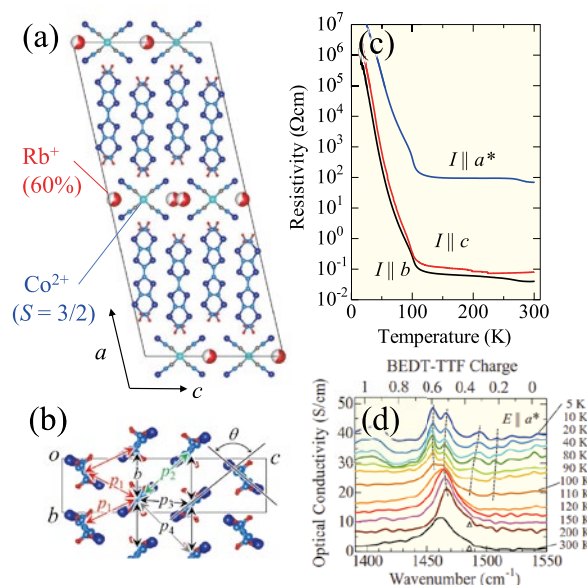


Fig. 1 (a) Crystal structure and (b) two-dimensional BEDT-TTF layer of  $\alpha''$ -Rb<sub>1.2</sub>Co. Temperature-dependence of (c) resistivity and (d)  $\nu_{27}$  vibrational mode.

incommensurate filling of  $\alpha''$ -Rb<sub>1.2</sub>Co and nearly commensurate  $\alpha''$ -K<sub>1.4</sub>Co.

In order to obtain evidence of the charge ordering, we measured the infrared optical spectra. In the wavenumber region of 1400–1550 cm<sup>-1</sup>, vibrational mode  $\nu_{27}$  can be observed for the BEDT-TTF molecule. The peak frequency of the  $\nu_{27}$  mode is very sensitive to the valence and often used in order to detect the charge states of the BEDT-TTF molecule. As shown in Fig.1(d), a splitting of the valence was found. This suggests that the charge-ordering transition occurs at about 100 K.

Reference [1] also discusses the existence of the  $\pi$ -d interaction using magnetic and magneto-dielectric properties.

## References

- [1] S. Iguchi, S. Yamada, R. Kobayashi, K. Morita, Y. Kudo, M. Kurosuo, N. Yoneyama, Y. Ikemoto, T. Moriwaki, and T. Sasaki, J. Phys. Soc. Jpn. **90**, 074701 (2021).

Satoshi Iguchi (Low Temperature Condensed State Physics Research Laboratory)

E-mail: satoshi.iguchi.c8@tohoku.ac.jp

URL: [http://cond-phys.imr.tohoku.ac.jp/index\\_e.html](http://cond-phys.imr.tohoku.ac.jp/index_e.html)

# Superconducting State with Pair Density Wave in $\text{La}_{1.87}\text{Sr}_{0.13}\text{Cu}_{0.99}\text{Fe}_{0.01}\text{O}_4$

The pair density wave (PDW) order, which is an intertwined state among the spin, charge density, and superconducting order parameters, has attracted attention in connection with superconductivity in cuprate oxides. To clarify the necessary conditions for the formation of PDW, we performed resonance X-ray scattering measurements on  $\text{La}_{1.87}\text{Sr}_{0.13}\text{Cu}_{0.99}\text{Fe}_{0.01}\text{O}_4$ . The signature of PDW appeared when the correlation length of the charge density wave exceeded  $\sim 30 \text{ \AA}$  upon cooling, suggesting the crucial role of charge correlation in the formation of PDW.

Since the discovery of high-temperature ( $T_c$ ) superconductivity (HTSC) in cuprate oxides, tremendous progress has been made in the field of strongly correlated electron systems. One recent area of interest regarding HTSCs is the pair density wave (PDW), which forms the spatially modulated spin and charge density (SDW and CDW) and the order parameter of the Cooper pair on the  $\text{CuO}_2$  planes. To experimentally identify the PDW order, the appearance of anisotropic (two-dimensional) superconductivity and the coexistence of spin and charge density wave orders (Fig. 1) need to be clarified [1]. A small amount of Fe substitution in  $\text{La}_{2-x}\text{Sr}_x\text{CuO}_4$  (LSCO) suppresses the superconducting transition temperature ( $T_c$ ) and enhances the stability of SDW and CDW orders [2]. Therefore, Fe-substituted LSCO is a suitable system to study the intertwining of complex orders in high- $T_c$  cuprates.

We performed resistivity and resonant soft X-ray scattering (RSXS) experiments on a high-quality single crystal of  $\text{La}_{1.87}\text{Sr}_{0.13}\text{Cu}_{0.99}\text{Fe}_{0.01}\text{O}_4$  (LSCFO). As shown in Fig. 1, anisotropic resistivity behavior was observed at temperatures between  $\sim 11 \text{ K}$  ( $T_2$ ) and  $\sim 32 \text{ K}$  ( $T_1$ ). Therefore, PDW fluctuations potentially existed between  $T_1$  and  $T_2$ . Furthermore, we observed the signal from the CDW order using RSXS measurements at low temperatures (Fig. 2). The CDW peak grew upon cooling, and the intensity tended to increase more markedly once the SDW order appeared at a low temperature. Thus, the development of CDWs can be enhanced by SDWs through intertwining. The correlation length ( $\xi_{\text{ch}}$ ) of the CDW order evaluated from the peak width increased with decreasing temperature below  $70 \text{ K}$ . The  $\xi_{\text{ch}}$  reached  $\sim 30 \text{ \AA}$ , which is approximately eight times the in-plane lattice constant at  $T_1$ , and remained constant. From the above results, it was found that the signature of PDW starts to appear when  $\xi_{\text{ch}}$  grows over  $\sim 30 \text{ \AA}$ , suggesting the crucial role of charge correlation in the formation of the PDW order in LSCFO. RSXS measurements on other copper oxides are expected to reveal the ubiquitous

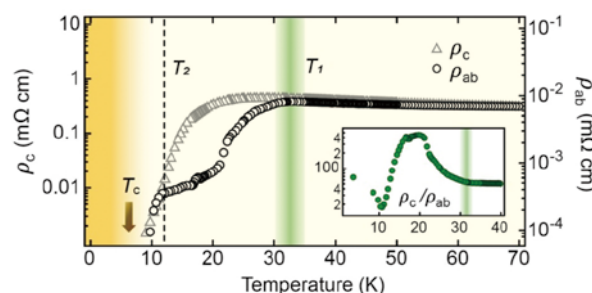


Fig. 1 Temperature dependence of the anisotropic resistivity [1].  $\rho_{ab}$  and  $\rho_c$  represent the in-plane and out-of-plane resistivity.

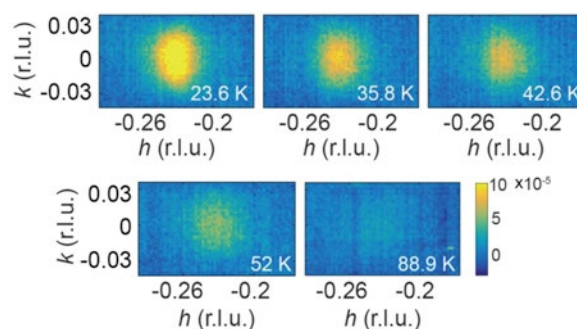


Fig. 2 Signals from charge density waves observed by resonant soft X-ray scattering experiments at various temperatures [1].

nature of PDW in high- $T_c$  cuprates and the universal relationship between CDW and PDW in cuprate oxides [3, 4].

## References

- [1] H. Huang, S.-J. Lee, Y. Ikeda, T. Taniguchi, M. Takahama, C.-C. Kao, M. Fujita, and J.-S. Lee, *Phys. Rev. Lett.* **126**, 167001 (2021).
- [2] M. Fujita, M. Enoki, and K. Yamada, *J. Phys. Chem. Solids* **69**, 3167 (2008).
- [3] S. Asano, K. Ishii, D. Matsumura, K. Kudo, T. Taniguchi, S. Saito, T. Sunohara, T. Kawamata, Y. Koike, and M. Fujita, *Phys. Rev. B* **104**, 214504 (2021).
- [4] H. Yamase, Y. Sakurai, M. Fujita, S. Wakimoto, and K. Yamada, *Nat. Commun.* **12**, 2223 (2021).

Masaki Fujita (Quantum Beam Materials Physics Research Laboratory)

E-mail: masaki.fujita.b5@tohoku.ac.jp

URL: <http://qblab.imr.tohoku.ac.jp/index-e.html>



# Magnetization Control by Angular Momentum Transfer from Surface Acoustic Wave to Ferromagnetic Spin Moments

In solids, there are various forms of angular momentum. Electrons have spin and orbital angular momenta. The circular motion of atoms can be viewed as the angular momentum of phonons. The interconversion between different forms of angular momentum is useful for spin-based information processing. Here, we demonstrate that the phonon angular momentum of surface acoustic waves can control magnetization by means of the phononic-to-electronic conversion of angular momentum in a Ni/LiNbO<sub>3</sub> hybrid device.

The injection of spin current is thought to be an efficient way of magnetization control in a nanoscale ferromagnet. Although rotational symmetry is, strictly speaking, broken in the magnet, the sum of angular momentum is nearly preserved over a short period, and it is transferred from the conduction electrons to magnetic moments in the injection process. Whether or not phononic angular momentum transfer is also effective for magnetization control is an area of interest.

In this work, we show that the phonon angular momentum of a surface acoustic wave can control the magnetization in a Ni/LiNbO<sub>3</sub> hybrid device. A surface acoustic wave is the acoustic wave propagating on a surface. It has ellipsoidal polarization, and the rotational direction is reversed when the wave vector is reversed. Therefore, the wave vector and angular momentum are closely coupled in the surface acoustic wave.

We fabricated a Ni/LiNbO<sub>3</sub> hybrid device, in which surface acoustic waves propagate on the Ni ferromagnet (Fig. 1). The Ni film has an elongated shape, and therefore the magnetization tends to align along the elongated direction at zero magnetic field owing to the shape anisotropy, while there is still up/down degeneracy. In order to demonstrate the magnetization control, we applied a strong magnetic field perpendicular to the elongated direction and decreased it to zero while applying surface acoustic waves. When the angular momentum of the surface acoustic wave is effectively transferred to the Ni ferromagnet, the magnetization direction after the application of the perpendicular magnetic field should be controlled by the angular momentum of the surface acoustic wave coupled to the wave vector (Fig. 2). We observed that the magnetization after this process depended on the wave vector of the surface acoustic wave.

The present results experimentally demonstrate an important functionality of angular momentum, the conversion to ferromagnetic spin moments, which shows the validity of phonon angular

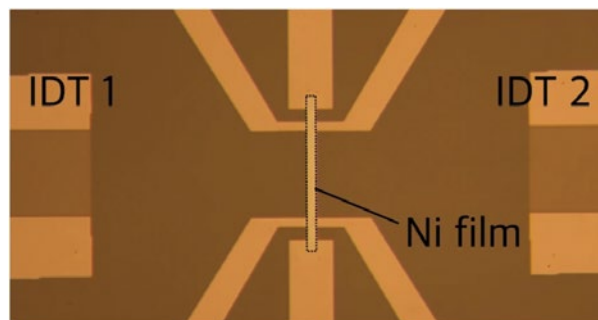


Fig. 1 An optical micrograph of the surface acoustic wave device used in this work [1].

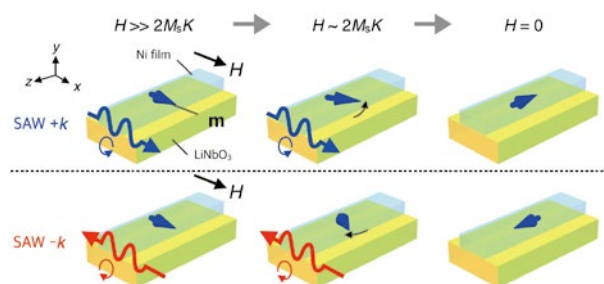


Fig. 2 Schematic illustrations of the magnetization control by angular momentum of surface acoustic wave [1].

momentum. The control of magnetization by the surface acoustic wave is useful to transfer the information carried by the microwave signal to the magnetic storage. In this sense, it is expected to provide a bridge between telecommunication technology and spintronics because surface acoustic devices are indispensable in contemporary telecommunications technology.

## References

- [1] R. Sasaki, Y. Nii, Y. Onose, Nat. Commun. **12**, 2599 (2021).

Yoshinori Onose (Quantum Functional Materials Physics Research Laboratory)

E-mail: yoshinori.onose.b4@tohoku.ac.jp

URL: <http://www.imr.tohoku.ac.jp/en/about/divisions-and-centers/research-division/08.html>



# Circular Polarized Light Induced Zero-Bias Photocurrent in Chiral 2D Organic-Inorganic Hybrid Perovskites

Noncentrosymmetry opens the door to a large variety of advanced properties in functional materials, such as ferroelectricity and nonlinear optics. In this study, a chirality-dependent circular photogalvanic effect, which is a zero-bias photocurrent-generating phenomenon by circular polarized light, was successfully discovered for the first time in a pair of chiral 2D organic-inorganic hybrid perovskites.

Breaking spatial inversion symmetry in materials leads to opportunities for the development of novel functionalities [1]. In particular, noncentrosymmetry in optoelectronics presents potential applications in the field of material science [2,3].

The circular photogalvanic effect (CPGE) is a novel optoelectronic phenomenon induced in noncentrosymmetric materials, in which a helicity-dependent steady-state photocurrent is generated by irradiation of circularly polarized light (CPL) without applying an external bias voltage. Although the CPGE has attracted growing interest as an efficient technique for the detection of novel chiral electronic states in opaque samples such as Weyl semimetals, the chirality dependence of CPGE has not been confirmed so far in enantiomorphous materials. This is due to the difficulty of designing chiral inorganic materials composed of heavy atoms with strong spin-orbit coupling (SOC). SOC in chiral systems affording a spin-splitting band is necessary for the induction of the CPGE.

To solve this issue, we have utilized two-dimensional (2D) organic-inorganic hybrid perovskites (OIHPs), introducing chiral organic cations between inorganic lead-iodide layers with strong SOC. Here, a pair of chiral 2D-OIHP lead iodides with space groups of  $P4_1(3)2_12$  were

investigated.

Under CPL exposure, the CPL helicity dependent zero-bias photocurrent, which is a feature of CPGE, was observed. Furthermore, the CPGE photocurrent apparently showed sign reversal depending on the chirality of the materials for the first time. This could be elucidated by the radial spin texture formed by “spin-momentum locking” in  $\mathbf{k}$ -space for a chiral system. From the microscopic viewpoint, the chiral 2D OIHP lead(II) halide-based material is a promising platform for opto-spintronics applications.

## References

- [1] K. Taniguchi, M. Nishio, N. Abe, P.-J. Huang, S. Kimura, T. Arima, and H. Miyasaka, *Angew. Chem. Int. Ed.* **60**, 14350 (2021).
- [2] P.-J. Huang, K. Taniguchi, M. Shigefuji, T. Kobayashi, M. Matsubara, T. Sasagawa, H. Sato, and H. Miyasaka, *Adv. Mater.* **33**, 2008611 (2021).
- [3] P.-J. Huang, K. Taniguchi, and H. Miyasaka, *J. Am. Chem. Soc.* **141**, 14520 (2019).

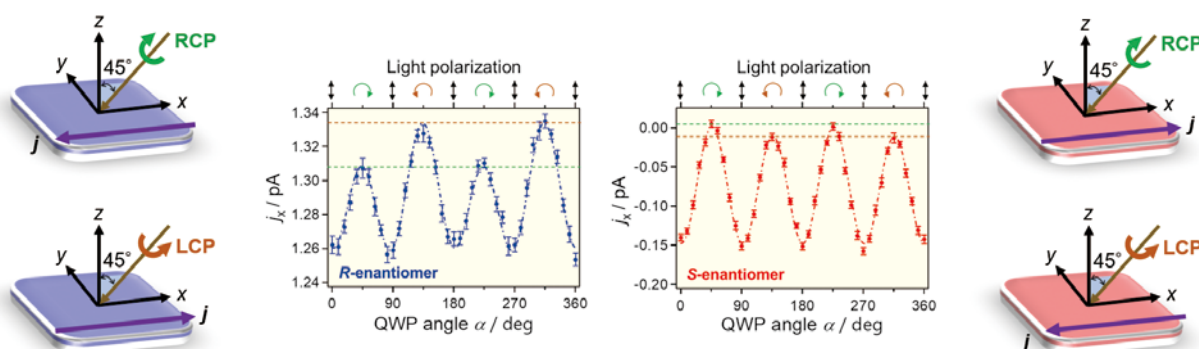


Fig. 1 Schematics of measurement configuration and photocurrent ( $j$ ) versus quarter-wave plate (QWP) angle for *R*- and *S*-enantiomers.

Po-Jung Huang, Kouji Taniguchi, and Hitoshi Miyasaka (Solid-State Metal-Complex Chemistry Research Laboratory)  
E-mail: [huang.po.jung.c8@tohoku.ac.jp](mailto:huang.po.jung.c8@tohoku.ac.jp), [koji.taniguchi.e2@tohoku.ac.jp](mailto:koji.taniguchi.e2@tohoku.ac.jp), [hitoshi.miyasaka.e7@tohoku.ac.jp](mailto:hitoshi.miyasaka.e7@tohoku.ac.jp)  
URL: <http://www.miyasaka-lab.imr.tohoku.ac.jp/cn5/HOME-Eng.html>

## Chiral Crystallization Assisted by Chiral Near-Field Force

It has been previously reported that giant crystal enantiomeric excess can be obtained by inducing chiral crystallization of NaClO<sub>3</sub> from an Au triangle trimer plasmonic nanostructure excited by a circularly polarized laser. However, its mechanism remains unclear. We showed that chiral optical force originating from the strong superchiral plasmonic near-field of the plasmonic nanostructure enantioselectively influences the kinetics of chiral nucleation.

Recent progress in plasmonics has shown that the chiral near-field generated by the excitation of localized surface plasmon resonance of metal nanoparticles can significantly boost intrinsically weak chiral light-matter interaction between circularly polarized light and chiral matter [1]. Recently, it has been discovered that chiral crystallization of NaClO<sub>3</sub> from a Au triangle trimer plasmonic nanostructure excited by a circularly polarized laser (CPL) yields the giant crystal enantiomeric excess, which cannot be achieved only by CPL [2, 3] (Fig. 1). However, the mechanism leading to the giant crystal enantiomeric excess remains unclear. We have performed a numerical analysis of the optical chirality density, which is a measure of chirality in an electromagnetic field, in the plasmonic near-field generated by CPL irradiation to the Au nanostructure to evaluate the contribution of the chiral optical force exerted on NaClO<sub>3</sub> chiral crystalline pre-critical clusters [4]. The analysis showed that a strong enhancement of optical chirality density, approximately 40-fold that of CPL, can be observed locally in the nanogap at the center of the Au nanostructure on a scale of a few tens of nanometers. This 'chiral hotspot' of the plasmonic near-field was found to be capable of producing the enantioselective chiral optical force, which acts on the chiral crystalline clusters. The magnitude of the chiral optical force was found to be comparable to that seen in previous experiments on laser-trapping-induced crystallization [5], where crystallization was induced by optical trapping of crystalline clusters, even in unsaturated solutions. These analyses indicate that enantioselective chirally biased diffusion of the chiral crystalline clusters induced by the chiral optical force can occur. The diffusion may cause fluctuations in the frequency of attachment of chiral building units onto crystal nuclei or in the concentration of chiral building units around the nuclei between both enantiomorphs, leading to the giant chiral enantiomeric excess.

### References

- [1] M. Hentschel, M. Schäferling, X. Duan, H. Giessen, and N. Liu, *Sci. Adv.* **3**, e1602735 (2017).
- [2] A. C. Cheng, H. Niinomi, T. Omatu, S. Ishida, K. Sasaki, and

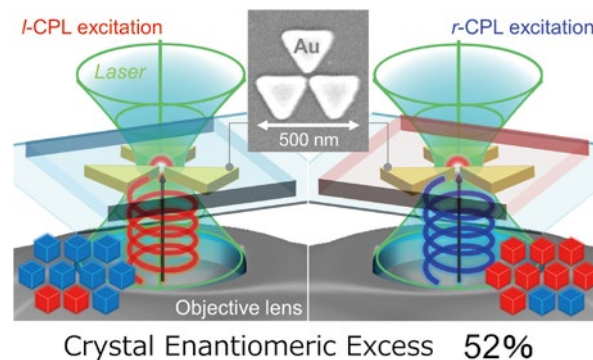


Fig. 1 Schematic of the NaClO<sub>3</sub> chiral crystallization experiment using a triangle trimer plasmonic nanostructure, which yielded a giant crystal enantiomeric excess [2].

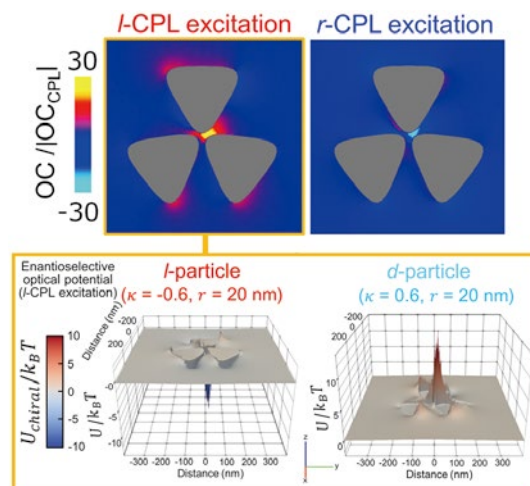


Fig. 2 Optical chirality density distribution analyzed by finite-difference time-domain method (upper). OC and OC<sub>CPL</sub> represents optical chirality density of near-field and of incident CPL, respectively. Enantioselective optical potential exerted on chiral nanoparticles (lower).  $\kappa$  is chirality parameter of chiral particle and  $r$  is radius of the particle.

T. Sugiyama, *J. Phys. Chem. Lett.* **11**, 4422 (2020).

- [3] H. Niinomi, T. Sugiyama, M. Tagawa, K. Murayama, S. Harada and T. Ujihara, *CrystEngComm* **18**, 7441 (2016).
- [4] H. Niinomi, T. Sugiyama, A.-C. Cheng, M. Tagawa, T. Ujihara, H. Y. Yoshikawa, R. Kawamura, N. Nozawa, J.T. Okada and S. Uda, *J. Phys. Chem. C* **125**, 6209 (2021).
- [5] T. Sugiyama, K. Yuyama and H. Masuhara, *Acc. Chem. Res.* **45**, 1946 (2012).

Hiromasa Niinomi (Crystal Chemistry Research Laboratory)

E-mail: hiromasa.niinomi.b2@tohoku.ac.jp

URL: <http://www.uda-lab.imr.tohoku.ac.jp/index-e.html>



## Field-Induced Superconductivity in UTe<sub>2</sub> with Spin-Triplet State

Field-induced superconductivity was observed in the spin-triplet superconductor UTe<sub>2</sub> when the pressure was tuned above the critical pressure. The magnetic ordered phase at low field collapsed above 10T, and superconductivity abruptly appeared, continuing above our highest field of 28T in the spin-polarized state.

Unconventional superconductivity in UTe<sub>2</sub> is of current interest in condensed matter physics; six papers related to UTe<sub>2</sub> were selected as “Most cited 10 articles in 2020” in JPSJ. A highlight of UTe<sub>2</sub> is the emergence of multiple superconducting phases under pressure and magnetic fields owing to the spin and orbital degrees of freedom, indicating the spin-triplet state. Spin-triplet superconductivity is expected to be topological superconductivity. Thus UTe<sub>2</sub> also provides a good opportunity to study “bulk” topological superconductivity.

Another important characteristic of UTe<sub>2</sub> is the large upper critical field,  $H_{c2}$ , which is much higher than the so-called “Pauli limit” expected from the weak-coupling BCS theory. Therefore, an unconventional superconducting mechanism, namely, the spin-triplet state, is in effect. In particular, when the field is applied along the  $b$ -axis in the orthorhombic structure, field-reentrant superconductivity is observed up to an extremely high field of 35T. This field-robust superconductivity has also been studied through spin susceptibility using NMR to clarify the superconducting mechanism from a microscopic point of view [1]. Low-temperature magnetization measurements [2] revealed that the lower critical field  $H_{c1}$  is also unusually anisotropic compared to the anisotropy of  $H_{c2}$ , implying a peculiar vortex state.

Here, we present another unusual superconducting property of the UTe<sub>2</sub>. Figure 1(a) shows the magnetoresistance of the  $H \parallel b$ -axis in UTe<sub>2</sub> when the pressure was tuned just above the critical pressure  $P_c$ . No superconductivity is detected at zero field, whereas a magnetically ordered phase (MO) appears. Surprisingly, when a high magnetic field above 10T was applied, field-induced superconductivity was detected. The  $H$ - $T$  phase diagram is shown in Fig. 1(b). At high fields, the magnetically ordered phase, most likely due to antiferromagnetism, was suppressed, and then the superconducting phase appeared in the spin-polarized state. These results are compatible with a spin-triplet scenario. Note that the superconductivity in the spin-polarized state resembles that observed above  $H_m \sim 40$ T for  $H \parallel [011]$  at ambient pressure.

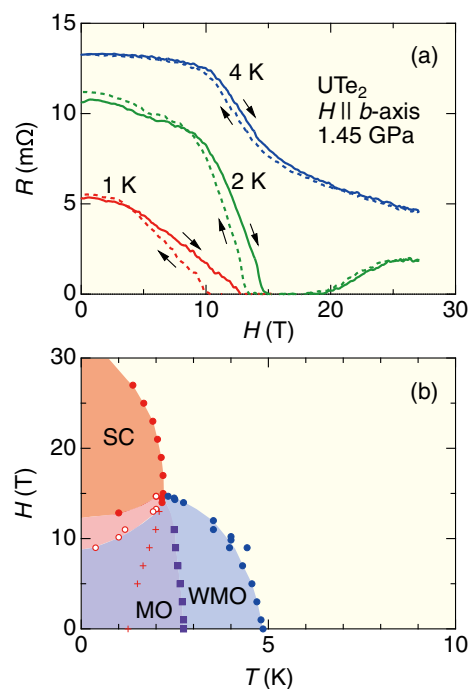


Fig. 1 (a) Magnetoresistance for  $H \parallel b$ -axis at 1.45 GPa just above the critical pressure in UTe<sub>2</sub>. Field-induced superconductivity was detected at 1K and 2K. (b) corresponding  $H$ - $T$  phase diagram. SC, MO and WMO denote superconductivity, magnetic order and weakly magnetic order, respectively [3].

The interplay between the different fluctuations may play a crucial role.

This work was done in collaboration with CEA-Grenoble, LNCMI, High field lab at IMR and Oarai center.

### References

- [1] G. Nakamine, K. Kinjo, S. Kitagawa, K. Ishida, Y. Tokunaga, H. Sakai, S. Kambe, A. Nakamura, Y. Shimizu, Y. Homma, D. Li, F. Honda, and D. Aoki, Phys. Rev. B **103**, L100503 (2021).
- [2] C. Paulsen, G. Knebel, G. Lapertot, D. Braithwaite, A. Pourret, D. Aoki, F. Hardy, J. Flouquet, and J. P. Brison, Phys. Rev. B **103**, L180501 (2021).
- [3] D. Aoki, M. Kimata, Y. J. Sato, G. Knebel, F. Honda, A. Nakamura, D. Li, Y. Homma, Y. Shimizu, W. Knafo, D. Braithwaite, M. Valiska, A. Pourret, J.-P. Brison, and J. Flouquet, J. Phys. Soc. Jpn. **90**, 074705 (2021).

Dai Aoki (Actinide Materials Science Research Laboratory)

E-mail: dai.aoki.c2@tohoku.ac.jp

URL: <http://www.imr.tohoku.ac.jp/en/about/divisions-and-centers/research-division/25.html>

# Effect of Ta Substitution on the Synthesis of (K,Na)(Nb,Ta)O<sub>3</sub> Powders by Hydrothermal Reaction

Ta-substituted (K,Na)NbO<sub>3</sub> powders with K-rich composition across a polymorphic phase boundary were synthesized at 200°C by a hydrothermal method. It was found that the synthesis behavior of (K,Na)(Nb,Ta)O<sub>3</sub> is strongly dependent on the combination of alkaline solution and raw powder.

The morphological control of ferroelectric powders with a perovskite-type structure has been widely investigated as an important technique for developing high-performance materials and devices. Pb(Zr,Ti)O<sub>3</sub> is the most widely investigated ferroelectrics material because of its excellent electrical properties. The best performance of Pb(Zr,Ti)O<sub>3</sub> is achieved at the morphotropic phase boundary (MPB), a discontinuous change in the crystalline phase from a tetragonal phase to a rhombohedral one.<sup>9)</sup> However, due to the toxicity of lead in the environment and the human body, there is an ongoing demand for lead-free ferroelectrics. (K,Na)NbO<sub>3</sub> has attracted much attention as a promising candidate to replace Pb(Zr,Ti)O<sub>3</sub>. In this study, we synthesized (K,Na)(Nb,Ta)O<sub>3</sub> powders with K-rich composition by the hydrothermal method and investigated their crystal structure and microstructure. In particular, we examined the synthesis behavior of (K,Na)(Nb,Ta)O<sub>3</sub> powders from the viewpoints of the combination of the alkaline solutions and raw powders [1].

Figures 1(a)-1(g) show Scanning Electron Microscope (SEM) images of the powders obtained in the range of  $C = 0-1$ . As seen, the morphology of powder changed from polymorphic to square at  $C = 0.3$ , and a smooth powder surface was observed. This observation suggests that the {100}<sub>c</sub> planes of the oxide become energetically stable as Ta content increases. In addition, the size of the square-shaped powder decreased with increasing nominal composition. SEM images of Nb<sub>2</sub>O<sub>5</sub> and Ta<sub>2</sub>O<sub>5</sub> powders are shown in Fig. 1(h) and 1(i). Rod-shaped particles were observed in Nb<sub>2</sub>O<sub>5</sub>, while Ta<sub>2</sub>O<sub>5</sub> particles had round shapes. These morphologies were significantly different from those observed with (K,Na)(Nb,Ta)O<sub>3</sub>. In addition, the particle size of Ta<sub>2</sub>O<sub>5</sub> powder was much smaller than that of Nb<sub>2</sub>O<sub>5</sub> powder. Therefore, it is considered that the particle size of the (K,Na)(Nb,Ta)O<sub>3</sub> powder decreased with increasing the nominal composition.

Figure 2 summarizes the volume fraction of perovskite phase estimated from the intensity ratio. As shown here, the synthesis behaviors of stoichiometric KOH-Nb<sub>2</sub>O<sub>5</sub>, NaOH-Nb<sub>2</sub>O<sub>5</sub>, KOH-Ta<sub>2</sub>O<sub>5</sub>, and NaOH-Ta<sub>2</sub>O<sub>5</sub> systems indicated that the formation of an

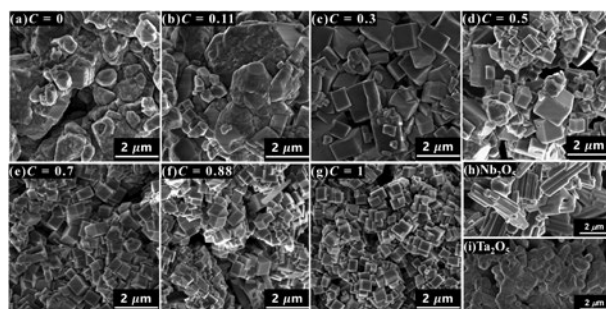


Fig. 1 SEM images of (a)-(g) (K,Na)(Nb,Ta)O<sub>3</sub>, (h) Nb<sub>2</sub>O<sub>5</sub>, and (i) Ta<sub>2</sub>O<sub>5</sub> powders.

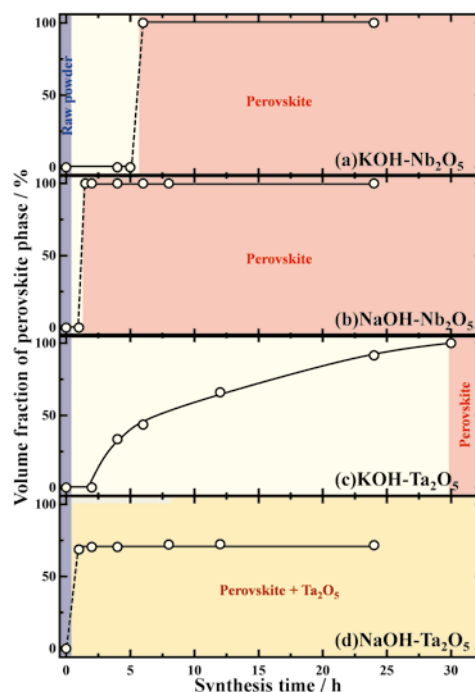


Fig. 2 Synthesis time dependence of volume fraction of perovskite phase: (a) KOH-Nb<sub>2</sub>O<sub>5</sub>, (b) NaOH-Nb<sub>2</sub>O<sub>5</sub>, (c) KOH-Ta<sub>2</sub>O<sub>5</sub>, and (d) NaOH-Ta<sub>2</sub>O<sub>5</sub>.

intermediate phase is the key factor to obtain a perovskite single-phase powder.

## References

- [1] S. Sano, T. Shiraishi, T. Kiguchi, and T.J. Konno, J. Ceram. Soc. Jpn. **129**, 365 (2021).

Toyohiko J. Konno (Materials Science of Non-Stoichiometric Compounds Research Laboratory)

E-mail: tjkonno@tohoku.ac.jp

URL: <http://www.imr.tohoku.ac.jp/en/about/divisions-and-centers/research-division/26.html>



## Tailorable Magnet Creation in a Paramagnetic Metal–Organic Framework Depending on Guest Species

Creation of magnets from nonmagnetic materials induced by external stimuli holds potential applications as magnetic switches, memories, and sensors, yet study of guest-responsive porous magnets remains rare. We demonstrated an electronic-state-flexible paramagnetic metal–organic framework that could change to either the ferrimagnetic or antiferromagnetic phase by accommodating different guest molecules in the lattice.

Magnetic metal–organic frameworks (MOFs), in which one or a few paramagnetic metal nodes and radical organic ligands are used to construct magnetic components, have sparked tremendous interest as switchable magnets due to their high degree of designability and structural diversity. Guest molecules that perturb the crystal lattice of the framework are capable of magnetic modulation in magnetic MOFs; however, guest-driven magnetic ground state (magnetic phase) changes with flexible lattices are surprisingly scarce.

In this study, we synthesized a paramagnetic guest-free framework,  $[\{\text{Ru}_2(2,4\text{-F}_2\text{PhCO}_2)_4\}_2 \text{TCNQ}(\text{OEt})_2]$  (**1**;  $2,4\text{-F}_2\text{PhCO}_2^- = 2,4\text{-difluorobenzoate}$ ;  $\text{TCNQ}(\text{OEt})_2 = 2,5\text{-diethoxy-7,7,8,8-tetracyanoquinodimethane}$ ) (Fig. 1a), which consists of two  $[\text{Ru}_2(2,4\text{-F}_2\text{PhCO}_2)_4]$  units as electron donors (D) and one  $\text{TCNQ}(\text{OEt})_2$  moiety as an acceptor (A) [1]. Compound **1** exhibited a thermally-induced electronic state modulation at 384 K between a two-electron-transferred state of  $[\text{D}^+-\text{A}^{2-}-\text{D}^+]_\infty$  ( $T < 384$  K) and a one-electron-transferred state of  $[\text{D}^+-\text{A}^{\cdot-}-\text{D}^+]_\infty$  ( $T > 384$  K), indicating flexible charge states towards the external stimuli.

Furthermore, the crystal structure of **1** was porous and flexible. Several guest molecules such as benzene (PhH), *p*-xylene (PX), dichloromethane (DCM), 1,2-dichloroethane (DCE), and carbon disulfide ( $\text{CS}_2$ ), could be accommodated into **1** to obtain solvated

compounds (**1-solv**) concomitant with an intralattice electron transfer from  $\text{A}^{2-}$  to one of the  $\text{D}^+$  moieties to form a  $[\text{D}^+-\text{A}^{\cdot-}-\text{D}^+]_\infty$  repeating unit and a structural modulation. This change in charge distribution allowed for intralayer ferrimagnetic ordering with spin sets of  $S = 3/2$  ( $\uparrow$ ),  $1$  ( $\uparrow$ ), and  $1/2$  ( $\downarrow$ ) for  $\text{D}^+$ , D, and  $\text{A}^{\cdot-}$ , respectively. Consequently, **1-solv** with PhH, PX, DCM, and DCE became a ferrimagnet with interlayer ferromagnetic interactions at Curie temperatures ( $T_c$ ) ranging from 70 to 92 K (Fig. 1b); meanwhile, with  $\text{CS}_2$ , it became an antiferromagnet with a Neel temperature ( $T_N$ ) of 78 K, owing to the presence of interlayer antiferromagnetic interactions (Fig. 1b). The magnetic ground state of ferrimagnet or antiferromagnet was influenced by the interlayer packing environment.

This work demonstrates an “alchemy for magnets”, in which bulk magnets are made from a nonmagnetic material by inserting diamagnetic guest molecules. The variable magnetism actuated by the electronic state modulation and structural change not only makes such strong electron-correlated MOFs candidates for future application as chemical sensors, but will also inspire the development of new magnetically and electronically functional materials.

### References

- [1] J. Zhang, W. Kosaka, H. Sato, and H. Miyasaka, *J. Am. Chem. Soc.* **143**, 7021 (2021).

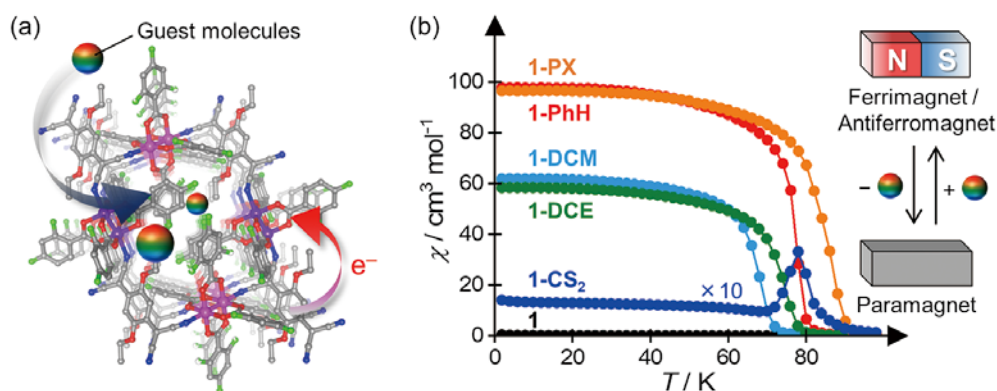


Fig. 1 (a) Crystal structure of paramagnetic compound **1**. (b) Temperature dependence of  $\chi$  measured at 100 Oe for **1** (black), **1-CS<sub>2</sub>** (blue), **1-DCE** (green), **1-DCM** (cyan), **1-PhH** (red), and **1-PX** (orange).

Jun Zhang (Exploratory Research Laboratory)

E-mail: jun.zhang.d2@tohoku.ac.jp

URL: <http://www.imr.tohoku.ac.jp/en/about/divisions-and-centers/research-division/33.html>



## *Research Centers*

IMR KINKEN Research Highlights 2022





# Longitudinal Magnetic Fluctuations Near the Superconducting Phase in Ferromagnetic Superconductor UGe<sub>2</sub>

International Research Center for Nuclear Materials and Science

The mechanism of superconductivity emerging in the ferromagnetic state has attracted much attention because it deviates from the conventional one induced by electron-phonon coupling. We clarified that longitudinal magnetic fluctuations develop near the superconducting phase in UGe<sub>2</sub>. Our observation strongly supports a consensus that superconductivity in ferromagnets is mediated by anisotropic magnetic fluctuations.

The emergence of superconductivity in ferromagnets was first observed in UGe<sub>2</sub> two decades ago [1].

In ferromagnets, the Cooper pairs must be formed on the degeneracy-lifted Fermi surfaces, which deviates from the conventional theory of superconductivity mediated by the electron-phonon interaction. Such unusual superconductivity has previously been theoretically predicted to be induced by Ising-like magnetic fluctuations [2]; however, experimental evidence has been absent in UGe<sub>2</sub>.

In UGe<sub>2</sub>, superconductivity was observed near the first-order quantum phase transition between the FM1 and FM2 phases, as shown in Fig. 1. The first-order line terminates at the critical point (CP) at around 7 K (a red point). This temperature is low enough to expect that magnetic fluctuations induced at the CP would survive even at low temperatures. However, the corresponding fluctuations have not been observed in the previous measurements of the nuclear spin-lattice relaxation rate,  $1/T_1$ , using nuclear magnetic resonance (NMR) [3].

Recently, we performed measurements of the spin-echo decay rate,  $1/T_2$ , to clarify a connection between superconductivity and magnetic fluctuations [4]. The term  $1/T_1$  corresponds to the transverse magnetic fluctuations against the nuclear quantization axis, that is, normal to the direction of the magnetization, while  $1/T_2$  includes the longitudinal magnetic fluctuations. Figure 1 shows the pressure dependence of  $1/T_2$  at ~1.6 K. The result demonstrates that  $1/T_2$  is enhanced near the first-order line. Absence of such anomaly in  $1/T_1$  suggests that longitudinal magnetic fluctuations develop near the quantum phase transition. Remarkably, the enhancement of  $1/T_2$  is not symmetric but predominant in the high-pressure FM1 phase. This also supports the connection

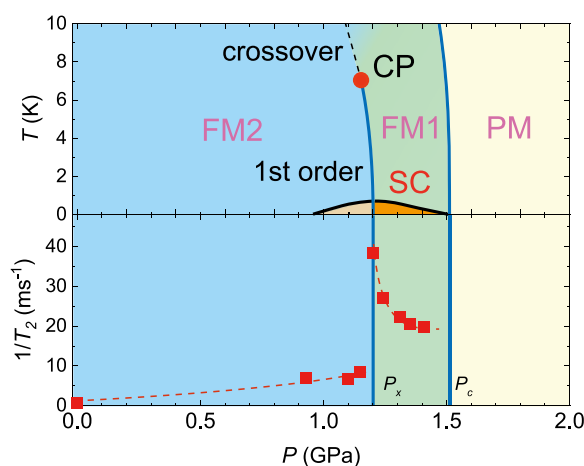


Fig. 1 Pressure-temperature phase diagram of UGe<sub>2</sub> near the superconducting (SC) phase (top). Pressure dependence of  $1/T_2$  (bottom).

between superconductivity and magnetic fluctuations in UGe<sub>2</sub>, because a realization of bulk superconductivity has been suspected in the low-pressure FM2 phase. Our study provided a clear indication that superconductivity is mediated by anisotropic magnetic fluctuation in FM superconductors.

## References

- [1] S. S. Saxena, P. Agarwal, K. Ahilan, F. M. Grosche, R. K. W. Haselwimmer, M. J. Steiner, E. Pugh, I. R. Walker, S. R. Julian, P. Monthoux, G. G. Lonzarich, A. Huxley, I. Sheikin, D. Braithwaite, and J. Flouquet, *Nature* **406**, 587 (2000).
- [2] D. Fay and J. Appel, *Phys. Rev. B* **22**, 3173 (1980).
- [3] H. Kotegawa, A. Harada, S. Kawasaki, Y. Kitaoka, Y. Haga, E. Yamamoto, Y. Ōnuki, K. M. Itoh, E. E. Haller, and H. Harima, *J. Phys. Soc. Jpn.* **74**, 705 (2005).
- [4] Y. Noma, H. Kotegawa, H. Tou, H. Harima, Y. Haga, E. Yamamoto, Y. Ōnuki, K. M. Itoh, A. Nakamura, Y. Homma, F. Honda, and D. Aoki, *J. Phys. Soc. Jpn.* **90**, 073707 (2021).

Hisashi Kotegawa (Corresponding Author, Department of Physics, Kobe University)

E-mail: kotegawa@crystal.kobe-u.ac.jp

Yasuyoshi Nagai (Head of International Research Center for Nuclear Materials and Science)

E-mail: yasuyoshi.nagai.e2@tohoku.ac.jp

URL: <http://www.imr-oarai.jp/en/>

# Unique Behavior of Martensitic Transformation at Low-Temperature in Ti-Ni-Cu Based Shape Memory Alloys

Cooperative Research and Development Center for Advanced Materials

The Center contributes to research and development of new materials and their fabrication processes to explore the possibility of their application as multi-functional materials for future technology, in collaboration with universities and government organizations. Here, we highlight our recent research on the precursor phenomena in Ti-Ni-Cu based shape memory alloys at low temperatures.

The thermodynamics of martensitic transformation and mechanical property at low temperatures in Ti-Ni based shape memory alloys has been reported previously [1-3]. A unique structural phase transition called “the Commensurate-Incommensurate (C-IC) transition” exists at low temperatures in Ti-Ni-based alloys [4], and we reported that the existence of the C-IC transition for the first time in Ti-Ni-Cu based alloys [1]. Here, we introduce the characteristics of C-IC transition by transmission electron microscope (TEM) observation in Ti-Ni-Cu based alloys.

The B2/B19 martensitic transformation temperature decreases with increasing Ni content. In  $\text{Ti}_{50.0-x}\text{Ni}_{40.0+x}\text{Cu}_{10.0}$  alloys with Ni compositions over  $x = 1.4$ , a pre-martensitic “intermediate” phase was detected by thermoanalysis measurements [1]. Here, the C phase in the C-IC transition corresponds to the Intermediate (I) phase. In the bright field image and selected-area diffraction pattern (SADP) obtained in the  $111_{\text{B2}}$  direction, the diffraction point derived from the B19 phase was observed at  $T = 87\text{K}$  and the B19 martensite plate was confirmed (Fig. 1).

The SADPs were observed at each temperature from the region shown in Fig. 1, and the temperature dependence of the diffraction point ( $0\zeta\zeta$ ) due to diffuse scattering was investigated. Figure 2 shows the temperature dependence of the diffuse scattering position ( $0\zeta\zeta$ ) of the  $x = 1.8$  alloy. It was clarified that the intensity of ( $0\zeta\zeta$ ) decreases with increasing temperature. On the low temperature side, the position of diffuse scattering is  $\zeta \approx 1/3$ , and it was clarified that the position of diffuse scattering deviates from  $1/3$  as the temperature rises. This tendency is in good agreement with previous studies [2], and it is considered that the C-IC transition occurs even at low temperature in Ni-rich Ti-Ni-Cu based alloy. However, changes in the microstructure at the C-IC transition are a topic for future study.

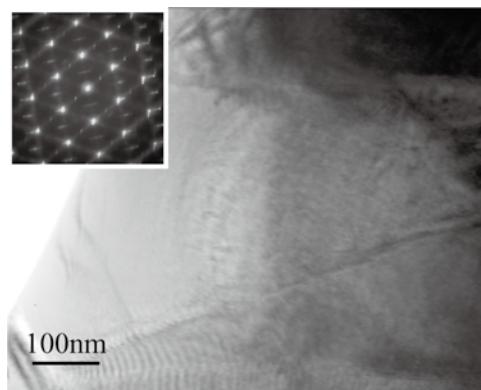


Fig. 1 The bright field image and selected-area electron diffraction pattern taken from  $111_{\text{B2}}$  direction at  $T = 89\text{K}$  in  $\text{Ti}_{48.2}\text{Ni}_{41.8}\text{Cu}_{10.0}$  alloy.

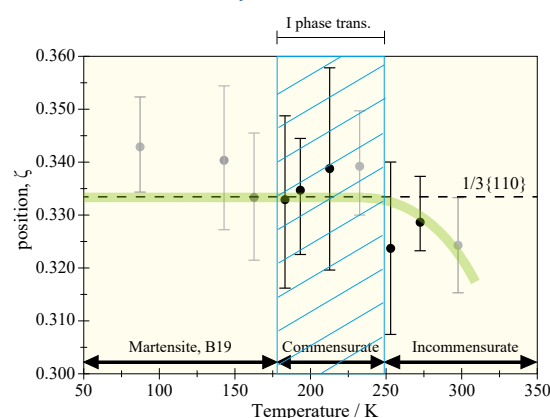


Fig. 2 Temperature dependence of ( $0\zeta\zeta$ ) position in  $\text{Ti}_{48.2}\text{Ni}_{41.8}\text{Cu}_{10.0}$  alloy.

## References

- [1] Y. Kimura, X. Xu, K. Niitsu, T. Omori, and R. Kainuma, *Mater. Trans.* **57**, 269 (2016).
- [2] K. Niitsu, H. Date, and R. Kainuma, *Scr. Mater.* **186**, 263 (2020).
- [3] E. E. Timofeeva, T.Y. Panchenko, A. I. Tagiltsev, N. G. Larchenkova, A. B. Tokhmetova, Y. I. Chumlyakov, and M. N. Volochaev, *Mater. Lett.* **282**, 128677 (2021).
- [4] M. S. Choi, T. Yamamoto, T. Fukuda, and T. Kakeshita, *Philos. Mag.* **88**, 2449 (2008).

Yuta Kimura (Corresponding Author, Cooperative Research and Development Center for Advanced Materials)

E-mail: yuta.kimura.b6@tohoku.ac.jp

Naoya Masahashi (Head of Cooperative Research and Development Center for Advanced Materials)

E-mail: naoya.masahashi.e6@tohoku.ac.jp

URL: <http://www.crdam.imr.tohoku.ac.jp/en/index-en.html>

# Development of YBa<sub>2</sub>Cu<sub>3</sub>O<sub>y</sub> Based Superconducting Wire Production for Fusion

## High Field Laboratory for Superconducting Materials

For a compact fusion system, 2nd Generation-High Temperature Superconductor (2G-HTS) wire was developed successfully with a formulation based on YBCO material with Y<sub>2</sub>O<sub>3</sub> nanoparticles acting as random pinning centers, which were specially optimized for a maximum performance at 20-25 T in the temperature range of 4.2-20 K. The wire consistently demonstrated the expected properties, while the best performing samples exhibited  $J_e$  (20K, 20T) > 1000 A/mm<sup>2</sup> and  $J_e$  (4.2K, 20T) > 2000 A/mm<sup>2</sup>.

The compact fusion system SPARC, which is currently under construction by the joint team of Massachusetts Institute of Technology (MIT) and Commonwealth Fusion Systems (CFS) relies on the availability of HTS wire with an engineering current density  $J_e$  of at least 700 A/mm<sup>2</sup> at 20K and 20T. Two years ago, even short laboratory samples with such characteristics were difficult to obtain, while the consistent production of thousands of kilometers of such wire at reasonable cost seemed unrealistic from the viewpoint of current science and engineering. Our team successfully developed a highly reproducible approach for the fabrication of 2G-HTS wire with a formulation based on YBCO material, with Y<sub>2</sub>O<sub>3</sub> nanoparticles acting as random pinning centers, specially optimized for a maximum performance at 20-25T in the temperature range of 4.2-20K. In total, over 300 km of HTS wire with a typical piece length of 300-600 m were delivered for the fusion application. The wire consistently demonstrated the expected properties, while the best performing samples exhibited  $J_e$  (20K, 20T) > 1000 A/mm<sup>2</sup> and  $J_e$  (4.2K, 20T) > 2000 A/mm<sup>2</sup>, as shown in Fig. 1. The consistency of the  $J_c$  performance was confirmed by  $J_c$  measurements at different facilities including the University of Geneva, National High Magnetic Field Laboratory (NHMFL), and Tohoku University, as shown in the inset of Fig. 1, where the Lift Factor is  $J_c$  under specified conditions normalized by  $J_c$  at 77K and a self field,  $J_c(B)/J_c(77K, sf)$ . Very good agreement of Lift Factors were confirmed at 20 and 4.2 K for B//c, leading to a consistent demonstration of  $J_c$  properties. The detailed angular dependence of  $J_c$  could be evaluated at high magnetic fields up to 20 T and 20 K as shown in Fig 2. This is important for the design of superconducting magnets for high field compact fusion reactors. Recently CFS have succeeded in the achievement of 20 T in a toroidal field coil with 2G-HTS wire [2].

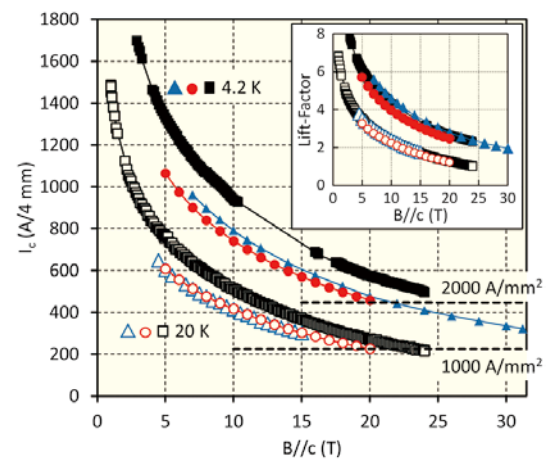


Fig. 1 Field dependence of  $J_c$  at 20 and 4.2 K measured by different facilities, University of Geneva (red), Tohoku University (black) and NHMFL (blue). The inset shows Lift Factor,  $J_c(B)/J_c(77K, sf)$  [1].

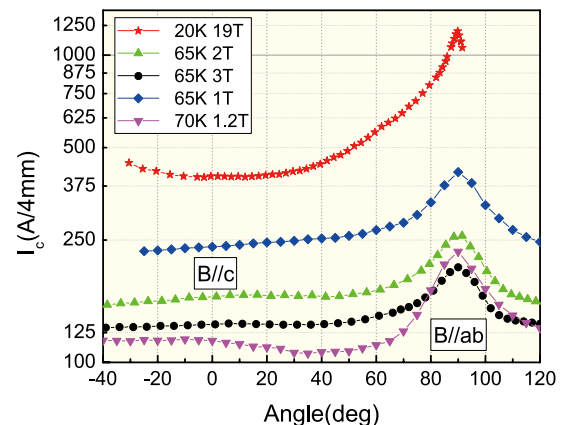


Fig. 2 Angular dependence of  $J_c$  at various temperatures and magnetic fields [1].

### References

- [1] A. Molodyk *et al.*, Scientific Reports **11**, 2084 (2021).
- [2] <https://news.mit.edu/2021/MIT-CFS-major-advance-toward-fusion-energy-0908> (2021).

Valery Petrykin (Corresponding Author, SuperOx Japan LLC)

E-mail: valery.petrykin@superox.co.jp

Hiroyuki Nojiri (Head of High Field Laboratory for Superconducting Materials)

E-mail: hiroyuki.nojiri.e8@tohoku.ac.jp

URL: <http://www.hflsm.imr.tohoku.ac.jp/cgi-bin/index-e.cgi>

## Creation of New Industrial Materials

### Trans-Regional Corporation Center for Industrial Materials Research

The Institute for Materials Research (IMR) has launched the Trans-Regional Corporation Center, a comprehensive Institute-wide effort that pairs the research groups at IMR across the innovation spectrum to solve industrial challenges of the present and address global energy problems for the future. The Center was established in 2016 based on an agreement between the IMR, Osaka Prefecture Government, and enterprises sponsored by the government, taking over Osaka and Kansai Center projects.

The Trans-Regional Corporation Center was established in Osaka as a special unit of the Institute for Materials Research (IMR), Tohoku University, in April 2016 based on an agreement with the Osaka Prefecture Government. The Center is sponsored by the Ministry of Education, Culture, Sports, Science, and Technology, and takes over the Kansai Center, which carried out its functions from 2012 to 2016. The Center has three goals. The first is to address the technical problems that industries have struggled to resolve. Secondly, the Center introduces academic output to industry, with the aim of applying these outputs to issues faced by society. Third, the Center helps to educate the next generation of materials scientists and researchers. We have organized a bimonthly forum called “Monodukuri Kisokoza”, which focuses on special topics regarding materials and processing. Projects are conducted through broad collaborations between the government, universities, research institutions, and other organizations. The Center has four venues in the Kansai and Tohoku area, namely, the Osaka office at the Osaka Prefecture University, the Hyogo office at the University of Hyogo, the Sendai office at the IMR, and the Monozukuri Business Information Center Osaka at the Creation Core Higashi-Osaka.

The Center has developed various materials and processes under collaboration with industry, university and government organizations. One of these is to fabricate Cu-Ni-Al alloys for Voice Coil Motor (VCM) systems in smartphone cameras, as shown in Fig. 1. These have been developed by IMR and DOWA METALTECH CO., LTD [1]. The alloys are fabricated by a unique thermo-mechanical processing comminuting severe cold-deformation and age heat-treatment, which promotes precipitation of fine-dispersed  $\gamma'$ -Ni<sub>3</sub>Al particles in the matrix phase of  $\gamma$ -Cu, as shown in Fig. 2 [2]. Ordering of the  $\gamma'$ -Ni<sub>3</sub>Al intermetallic phase can be controlled by final aging at a low temperature. As a result, the Cu-Ni-Al alloy plates yields excellent mechanical properties, with an ultimate tensile strength of more than 1,400 MPa and a Vickers hardness of 430 Hv. In addition,

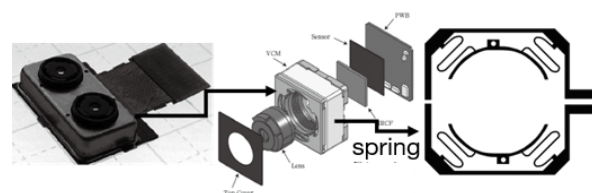


Fig. 1 Structure of VCM module and shape of leaf spring [1].

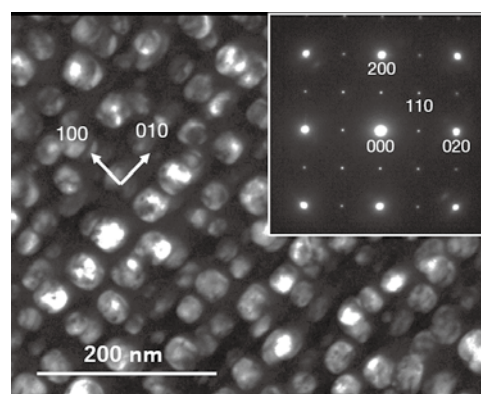


Fig. 2 Transmission electron microscopy-dark field image, together with the corresponding selected area electron diffraction pattern (inset), taken from the parent grains of Cu-Ni-Al alloy specimens developed in our study [2].

the Cu-Ni-Al alloys exhibit favorable features for VCM systems such as good stiffness, springiness, corrosion-resistance, and discoloration-resistance.

Similar collaborative research for practical applications utilizing academic knowledge and industrial technology are in progress. The Trans-Regional Corporation Center will make efforts to innovate in metallic material industry through alliances with partners and to promote scientific research in materials science.

#### References

- [1] T. Shuto, S. Kasatani, H. Hyodo, H. Watanebe, H. Narieda, A. Sugawara, and S. Semboshi, *Materia Jpn.* **60**, 119 (2021).
- [2] S. Semboshi, R. Hariki, T. Shuto, H. Hyodo, Y. Kaneno, and N. Masahashi, *Metall. Mat. Trans. A*, **52**, 4934 (2021).

Satoshi Semboshi (Corresponding Author, Trans-Regional Corporation Center for Industrial Materials Research)

E-mail: satoshi.semboshi.c8@tohoku.ac.jp

Naoya Masahashi (Head of Trans-Regional Corporation Center for Industrial Materials Research)

E-mail: naoya.masahashi.e6@tohoku.ac.jp

URL: <http://www.imr.tohoku.ac.jp/en/about/divisions-and-centers/facilities/04.html>



# Investigation of the Excited States and Intramolecular Charge-Transfer Transitions in Porphyrin-Based Nanostructures

Collaborative Research Center on Energy Materials

Porphyrins have attracted research interest for many years due to their relevance in biology, catalysis and medicine. The application of functional dyes relies on their optoelectronic properties, and the accurate prediction of excited states in such systems is important for design of new synthetic porphyrins with desirable optical properties. Our study provided a significant improvement in accuracy of the agreement between theoretical prediction and experiment of the localized  $\pi-\pi^*$  and intramolecular charge transfer (ICT) transitions, thus allowing confident interpretation of UV–vis–NIR spectra.

For fully conjugated oligoporphyrins (see Fig. 1a), a systematic red-shift in the near-infrared absorption has been demonstrated which can potentially be used in photodynamic therapy (PDT) against cancer. These oligomers have three optical windows: the lowest energy near-infrared or infrared transition region (I), the low energy visible range transition region (II) and the transition region (III) located on the edge of the ultraviolet zone. Therefore, the accurate assignment and theoretical prediction of the major optical transitions is important in order to identify the features of these absorption bands for molecular electronics and biomedical applications.

Recently, it was shown that for a large variety of phthalocyanines and their analogues, the time-dependent density functional theory (TDDFT)-predicted energies of the  $Q_x$ - and  $Q_y$ -bands and their splitting correlate well with the amount of Hartree–Fock exchange present in the specific exchange–correlation functional (ECF), with the LC-BP86 and LC-wPBE ECFs providing the best agreement between theory and experiment ( $<0.05$  eV). The pure GGA (BP86) exchange–correlation functional severely underestimated, while long-range corrected LC-BP86 and LC-wPBE ECFs strongly overestimated, the intramolecular charge-transfer (ICT) transitions experimentally observed in the 450–650 nm region for the-OR-, -SR-, and -NR<sub>2</sub>substituted phthalocyanines and their analogues. Hybrid CAM-B3LYP/PCM, PBE1PBE/PCM, and B3LYP/PCM ECFs were found to be much better in predicting the energies of such ICT transitions. Moreover, a single exchange–correlation functional was not found that could accurately predict the energies and the splitting of the  $Q_x$ - and  $Q_y$ -bands as well as the energies of ICT transitions [1].

Based on previous results, our current investigation showed a good agreement between theory and experiment with respect to the transition

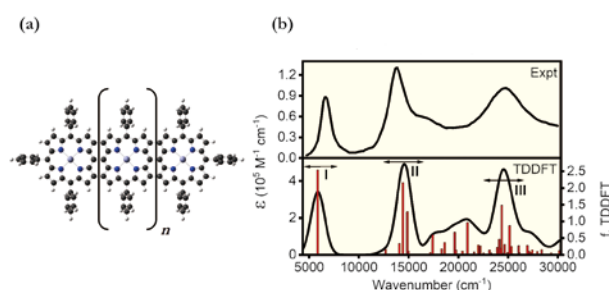


Fig. 1 (a) Structure porphyrin tapes ( $n=1-10$ ); (b) experimental and TDDFT-predicted UV-vis spectrum of tetramer.

energies and intensities (Fig. 1b).

This afforded band assignments which are more reliable than anything reported previously. It was confirmed that with increasing size of the porphyrin tape, there was an increase in ICT states between spectral regions II and I. Moreover, the spectral region III was dominated by a single transition state that originated almost exclusively from a HOMO to LUMO excitation. A quantitative correlation was shown between the x-polarized Soret-type transition and the most intense band that was experimentally observed in region II [2]. We also demonstrated, at least for the shorter tapes (**2-4**), that spectral region I was dominated by the y-polarized Soret-type transition, as shown in Fig. 1b. In the cases of porphyrins **1-12**, our calculations agreed well with the semi-empirical ZINDO/S spectral predictions and available experimental MCD data reported previously. In particular TDDFT-based sum-over-states calculations correctly predicted the signs of the MCD A- and B-terms in the Q-band region.

## References

- [1] R. V. Belosludov, D. Nevonen, H. Rhoda, J. Sabin, and V. N. Nemykin, *J. Phys. Chem. A* **123**, 132 (2019).
- [2] R. V. Belosludov, D. Nevonen and V. N. Nemykin, *J. Phys. Chem. A*, **125**, 2480 (2021).

Rodion Belosludov (Corresponding Author, Collaborative Research Center on Energy Materials)

E-mail: rodion@tohoku.ac.jp

Tetsu Ichitsubo (Head of Collaborative Research Center on Energy Materials)

E-mail: tichi@tohoku.ac.jp

URL: <http://www.imr.tohoku.ac.jp/en/about/divisions-and-centers/facilities/05.html>



# Magnetic Materials Design with Theoretical Analysis Tools for Magnetic and Electronic Structures

Center for Computational Materials Science

Magnetic materials with complex magnetic structures exhibit various physical phenomena, such as the anomalous Hall effect and the magnetoelectric effect. The occurrence of physical phenomena is dominated by the order parameters, symmetry of magnetic states, and topology of electronic structures. We developed a new framework to predict physical phenomena in magnetic materials by suggesting new theoretical tools for analyzing magnetic and electronic structures.

The diversity of the physical properties of magnets provides a fascinating area of research in condensed matter physics. Transport phenomena in antiferromagnets have essential advantages in comparison with ferromagnets because there is no unexpected coupling at the interface and no perturbing stray field in the devices. There are many restrictions imposed by magnetic structures on the physical properties of magnets. Representing a magnetic structure using symmetry, order parameters, and topology is therefore useful for identifying possible transport phenomena in magnetic states and discovering functional magnetic materials. For example, it is known that the occurrence of response phenomena, such as the anomalous Hall effect, anomalous Nernst effect, and magnetoelectric effect, is dominated by the magnetic point group, which characterizes the macroscopic symmetry of the magnetic structure.

The major challenge in first-principles calculations for magnetic materials is the prediction of the experimental magnetic structure for a given material. We recently established a theory to generate possible high-symmetry magnetic structures for given crystal systems [1] and developed a framework to predict stable magnetic structures using magnetic-structure generation theory combined with first-principles calculations [2] (see Fig. 1). We benchmarked the predictive power of the new framework on the supercomputing system, MASAMUNE-IMR, at the Center for Computational Materials Science in IMR, and showed the high accuracy of the framework for reproducing experimental magnetic structures [2].

The mechanisms to enhance the anomalous Hall effect, anomalous Nernst effect, and spin Hall effect in magnetic materials were also investigated based on electronic structure analysis of magnetic materials. We investigated in detail the contribution of the Berry curvature around the topological degeneracy to transport phenomena in hole-doped shandite compounds  $\text{Co}_3\text{In}_x\text{Sn}_{2-x}\text{S}_2$  [3], which are representative magnetic Weyl semimetals, and in orthorhombic  $\text{CuMnAs}$  [4] (Fig. 2), which is proposed as an antiferromagnetic semimetal hosting nodal lines and Dirac points. With these analyses, we predicted a large anomalous Nernst effect in  $\text{Co}_3\text{In}_x\text{Sn}_{2-x}\text{S}_2$  and a large spin Hall effect in orthorhombic  $\text{CuMnAs}$  caused by specific topological

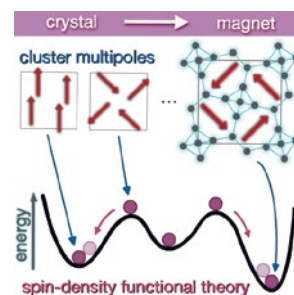


Fig.1 A schematic view of magnetic structure prediction by cluster multipole method combined with the first-principles calculations based on spin-density functional theory.

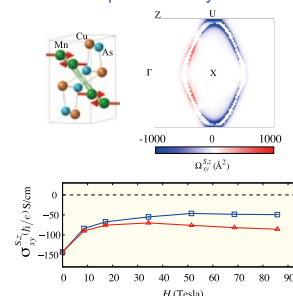


Fig.2 Berry curvature analysis for a magnetic ordered state of  $\text{CuMnAs}$ , showing magnetic structure, spin-Berry curvature originated from the gapped nodal line, and the spin-Hall conductivity under the magnetic fields along different directions.

degeneracies of the electronic structure around the Fermi surfaces. The large transport phenomena with a dominant contribution from topological bands paves the way for the discovery of new functional magnetic materials in the field of spintronics.

## References

- [1] M.-T. Suzuki, T. Nomoto, R. Arita, Y. Yanagi, S. Hayami, and H. Kusunose, *Phys. Rev. B* **99**, 174407 (2019).
- [2] M.-T. Huebsch, T. Nomoto, M.-T. Suzuki, and R. Arita, *Phys. Rev. X* **11**, 011031 (2021).
- [3] Y. Yanagi, J. Ikeda, K. Fujiwara, K. Nomura, A. Tsukazaki, and M.-T. Suzuki, *Phys. Rev. B* **103**, 205112 (2021).
- [4] V. T. N. Huyen, Y. Yanagi, and M.-T. Suzuki, *Phys. Rev. B* **104**, 035110 (2021).

Michi-To Suzuki (Corresponding Author, Center for Computational Materials Science)

E-mail: mts@tohoku.ac.jp

Momiji Kubo (Head of Center for Computational Materials Science)

E-mail: momiji@tohoku.ac.jp

URL: <http://www.sc.imr.tohoku.ac.jp/eng/>

## Current Status of Collaborative Research Programs of CNSAM

### Center of Neutron Science for Advanced Materials

The Center of Neutron Science for Advanced Materials is a neutron facility with a background in novel materials science in IMR. This center manages four neutron instruments at the research reactor facility JRR-3 and the spallation neutron source J-PARC MLF. Here, we report the current status of the research program and the outcomes obtained from the JRR-3, which has recently started reoperation.

The Center of Neutron Science for Advanced Materials (CNSAM) was established in 2010 to promote novel material science research using neutrons. CNSAM operates one diffractometer (HERMES) and two neutron spectrometers (TOPAN and AKANE) in the JRR-3 research reactor of the Japan Atomic Energy Agency. HERMES can precisely determine the arrangement of atoms and spins, while their motions are examined by AKANE and TOPAN. These are used for the target energy and momentum transfer regimes. POLANO, located at the Materials and Life Science Experimental Facility (MLF) at the Japan Proton Accelerator Research Complex (J-PARC), is a new spectrometer designed to perform polarization analysis in higher-energy regions beyond those measured by conventional triple-axis spectrometers. POLANO and TOPAN are equipped with polarized options and can disentangle the nuclear and magnetic contributions. We aim to contribute to condensed matter physics and materials science with the multipurpose neutron instruments of PATH, which is a collective term for the neutron instruments managed by the CNSAM.

To achieve this purpose, we established an international collaborative research program in IMR from FY 2019. We provide opportunities not only for experiments with neutron beams but also for the development of neutron devices and analysis methods, and even for theoretical work using our neutron data. Proposals can be submitted under several categories, such as “Neutron experiment at MLF/JRR-3,” “Instrumental development,” “Development in analysis method,” “Structural analysis and data handling,” and “Others”. Under the category “Others,” proposals on the complementary use of neutron and other quantum beams, such as X-ray and muon beams, are accepted. In FY 2021, we received 20 and three proposals from domestic and overseas researchers, respectively. Furthermore, the research reactor JRR-3 started reoperation in February 2021, and we received 29 proposals for our neutron instrument at

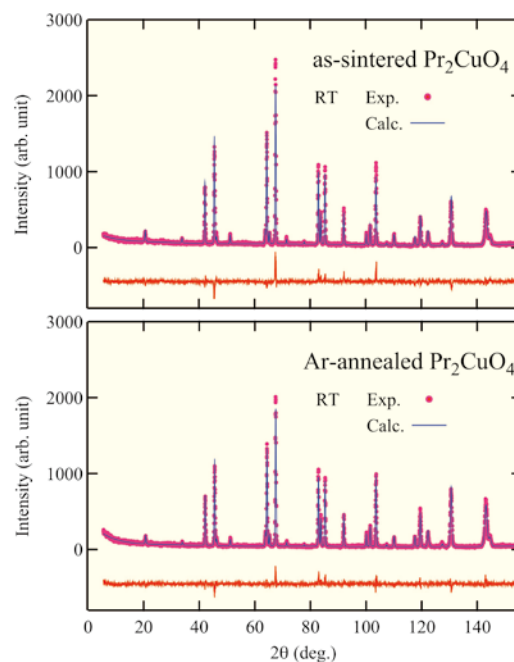


Fig. 1 Powder diffraction patterns of as-sintered and reduction annealed  $\text{Pr}_2\text{CuO}_4$ .

JRR-3 through the user program managed by the Institute for Solid State Physics, the University of Tokyo.

Figure 1 shows the neutron diffraction profiles of  $\text{Pr}_2\text{CuO}_4$ , the parent compound of a high-transition-temperature superconductor, which was obtained at HERMES. The structural changes due to reduction annealing were clarified using Rietveld analysis. Combined with the results of structural refinement for superconducting  $\text{La}_{1.8}\text{Eu}_{0.2}\text{CuO}_4$ , we reported the annealing effects on the crystal structure of  $R_2\text{CuO}_4$  (R: rare earth atom) and its relationship with the appearance of superconductivity [1]. This is the first publication from JRR-3 since it began reoperation.

#### References

- [1] M. Fujita, T. Taniguchi, T. Wang, S. Torii, T. Kamiyama, K. Ohashi, T. Kawamata, T. Takamatsu, T. Adachi, M. Kato, and Y. Koike, J. Phys. Soc. Jpn. **90**, 105002 (2021).

Masaki Fujita (Head of Center of Neutron Science for Advanced Materials)

E-mail: masaki.fujita.b5@tohoku.ac.jp

URL: <http://nc-imr.imr.tohoku.ac.jp/index-e.html>

# Spin Dynamics Studied by Inelastic Neutron Scattering Experiments in Spin-Triplet Superconductor UTe<sub>2</sub>

International Collaboration Center

Superconductivity in UTe<sub>2</sub> has attracted significant attention. The large upper critical field and multiple superconducting phases support a scenario for the spin-triplet state. In contrast to ferromagnetic superconductors with a spin-triplet state, ferromagnetic fluctuations were not experimentally detected in UTe<sub>2</sub>. We investigated the spin dynamics through inelastic neutron scattering experiments and detected antiferromagnetic fluctuations with an incommensurate wave vector.

Recently discovered superconductivity in UTe<sub>2</sub> is a current research topic in condensed matter physics. It is believed that UTe<sub>2</sub> is located in the proximity of the ferromagnetic order; thus, spin-triplet superconductivity is expected. In fact, the observed large upper critical field  $H_{c2}$ , which greatly exceeds the Pauli paramagnetic limit, supports a spin-triplet scenario. Superconductivity in the spin-triplet state is already known in ferromagnetic superconductors, namely UGe<sub>2</sub>, URhGe, and UCoGe, which are categorized as weak ferromagnets with a 5f-itinerant nature. Superconductivity coexists microscopically with ferromagnetism. Therefore, ferromagnetic fluctuations are expected to be the mechanism of superconducting Cooper pairs; indeed, ferromagnetic fluctuations have been experimentally detected. On the other hand, UTe<sub>2</sub> is a heavy fermion paramagnet; thus, the ferromagnetic fluctuations are not trivial, although they are inferred from the  $\mu$ SR experiments.

To clarify the magnetic fluctuations, we performed inelastic neutron scattering experiments at ILL using a large single crystal of high-quality UTe<sub>2</sub> [1]. As shown in Fig.1(c), antiferromagnetic fluctuations with an incommensurate wave vector  $k_1=(0, 0.57, 0)$  were detected. These fluctuations saturate below  $T^*\sim 15$  K, implying a possible relationship with the NMR results, thermal expansion [2], and resistivity measurements. A quasi-elastic signal was detected, indicating that the magnetic moment was parallel to the a-axis with sine-wave modulations with  $k_1$ . These low-dimensional fluctuations are probably due to the unique crystal formation with a ladder structure as shown in Fig.1(a).

The ferromagnetic fluctuations were not detected within energy transfers from 0.6 to 7.5 meV down to 2 K. These results constitute constraints for models of magnetically mediated superconductivity in UTe<sub>2</sub>.

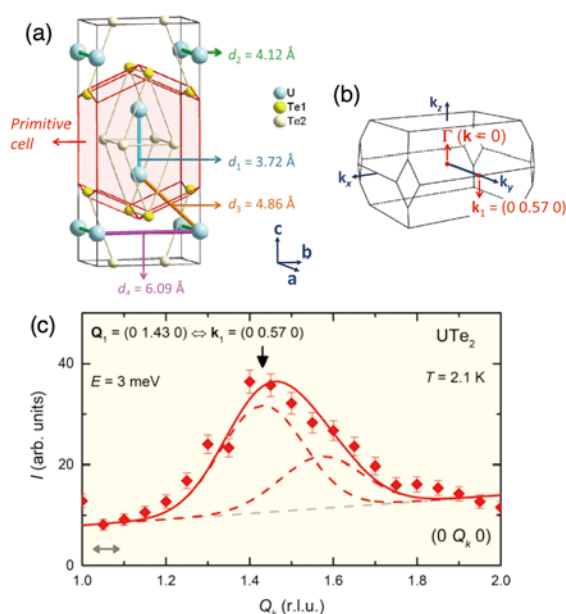


Fig.1 (a) body-centered orthorhombic structure and (b) its Brillouin zone of UTe<sub>2</sub>. (c)  $(0, Q_x, 0)$  scan of UTe<sub>2</sub> at 2.1 K above  $T_c$ .

At temperatures below  $T_c \sim 1.7$  K, a modification of the excitation spectrum at  $k_1$  was observed, indicating the feedback of superconductivity on the magnetic excitation [3].

This work was done in the framework of international collaboration project of ICC-IMR with CEA-Grenoble and LNCMI.

## References

- [1] W. Knafo, G. Knebel, P. Steffens, K. Kaneko, A. Rosuel, J.-P. Brison, J. Flouquet, D. Aoki, G. Lapertot, and S. Raymond, *Phys. Rev. B* **104**, L100409 (2021).
- [2] K. Willa, F. Hardy, D. Aoki, D. Li, P. Wiecki, G. Lapertot, and C. Meingast, *Phys. Rev. B* **104**, 205107 (2021).
- [3] S. Raymond, W. Knafo, G. Knebel, K. Kaneko, J.-P. Brison, J. Flouquet, D. Aoki, and G. Lapertot, *J. Phys. Soc. Jpn.* **90**, 113706 (2021).

Dai Aoki (Corresponding Author, Actinide Materials Science Research Laboratory)

E-mail: dai.aoki.c2@tohoku.ac.jp

Hiroyuki Nojiri (Head of International Collaboration Center)

E-mail: icc-imr@grp.tohoku.ac.jp

URL: <http://www.icc-imr.imr.tohoku.ac.jp/>

## Local Structure of Sn in $\beta$ -Ga<sub>2</sub>O<sub>3</sub>

Center for Advanced Light Source and Materials Science

Sn-doped  $\beta$ -Ga<sub>2</sub>O<sub>3</sub> single crystals were grown by the floating-zone method. We successfully investigated the local structural features of Sn in  $\beta$ -Ga<sub>2</sub>O<sub>3</sub> by X-ray absorption fine structure (XAFS) analysis. The XAFS analysis indicated the preference of Sn<sup>4+</sup> at the octahedral sites in the  $\beta$ -Ga<sub>2</sub>O<sub>3</sub> structure.

$\beta$ -Ga<sub>2</sub>O<sub>3</sub> has recently attracted attention as an excellent candidate for transparent conductive oxides because of its high transmittance of more than 80% in the wavelength range of 300–1000 nm. The electrical and optical properties of the  $\beta$ -Ga<sub>2</sub>O<sub>3</sub> could be controlled by introducing the appropriate dopants. In this context, the interesting properties of Sn-doped  $\beta$ -Ga<sub>2</sub>O<sub>3</sub> have been studied; however, the structural analysis, including the determination of the valence and environmental structure of the doped elements, has not been revealed. The crystal structure of  $\beta$ -Ga<sub>2</sub>O<sub>3</sub> is monoclinic with a space group of *C2/m* and consists of two crystallographically distinct Ga sites denoted as Ga1 and Ga2, with four- and six-fold coordination environments, respectively. X-ray absorption fine structure (XAFS) analysis with ab initio multiple-scattering calculations using the FEFF code is among the most effective methods for elucidating the environmental structure of trace elements. Herein, we conducted an advanced analysis and characterization of Sn-doped  $\beta$ -Ga<sub>2</sub>O<sub>3</sub> [1].

Single crystals of Sn-doped  $\beta$ -Ga<sub>2</sub>O<sub>3</sub> were grown by the floating-zone (FZ) method using a double ellipsoid mirror furnace. The crystalline phase of the grown crystals was confirmed using single crystal X-ray diffraction. The amounts of Sn were determined using inductively coupled plasma mass spectrometry (ICP-MS). XAFS spectra at the Sn *K*-absorption edges were recorded at the Photon Factory (Institute of Material Structure Science, High Energy Accelerator Research Organization (KEK), Tsukuba, Japan). Transparent and crack-free Sn-doped  $\beta$ -Ga<sub>2</sub>O<sub>3</sub> single crystals were successfully grown, as shown in Fig. 1. The Sn-doped samples were bluish in color. The concentration in the Sn-doped sample was below the detection limit of electron probe micro analysis (EPMA), and the ICP-MS results showed a value of 570 ppm.

The *K*-absorption edge energy of Sn in the Sn-doped  $\beta$ -Ga<sub>2</sub>O<sub>3</sub> was identical to that of Sn in SnO<sub>2</sub>, suggesting that the Sn atoms are in the tetravalent state. The Sn doping increased the vacancies of the Ga sites and changed the optical properties. To



Fig. 1 Photograph of Sn doped  $\beta$ -Ga<sub>2</sub>O<sub>3</sub> crystals grown by FZ method.

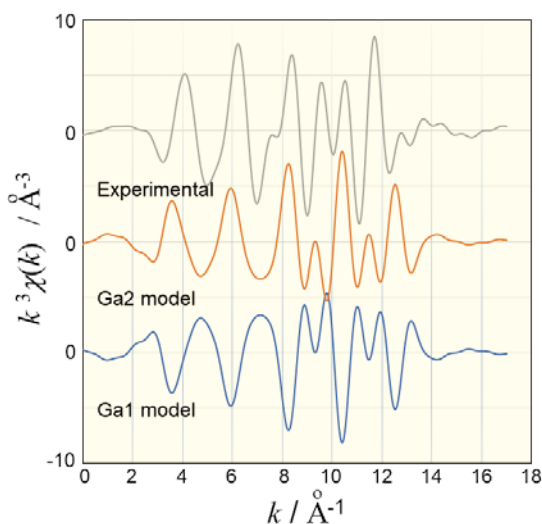


Fig. 2 Experimental and simulated profiles of Sn *K*-edge  $k^3$ -weighted  $\chi(k)$  functions.

directly determine the site preference for Sn, multiple-scattering EXAFS simulations were conducted. Figure 2 shows the EXAFS spectra, and the two models of the Sn environmental structure, where Sn is present in either Ga1 or Ga2 sites. The oscillation profile analysis, as shown in Fig. 2, suggests that the oscillation peak position and intensity of the Ga2 model, in which Sn occupied the octahedral site, are in good agreement with the experimental signal. Similar structural analysis was also performed for Mn-doped  $\beta$ -Ga<sub>2</sub>O<sub>3</sub>. Mn *K*-edge XAFS spectra analysis revealed an overall preference of Mn<sup>2+</sup> at tetrahedral sites.

### References

- [1] H. Arima-Osonoi, K. Yamazaki, R. Simura, T. Sugawara, K. Yubuta, K. Sugiyama, and A. Yoshiasa, *J. Cryst. Growth* **570**, 126223 (2021).

Kazumasa Sugiyama (Head of Center for Advanced Light Source and Materials Science)

E-mail: kazumasa.sugiyama.e6@tohoku.ac.jp

URL: <http://www.imr.tohoku.ac.jp/en/about/divisions-and-centers/collaboration/08.html>



# Demonstration of BCS-BEC Crossover in a Two-Dimensional Superconductor with Diluted Carrier Density

Laboratory of Low Temperature Materials Science

Bardeen-Cooper-Schrieffer (BCS) condensation and Bose-Einstein condensation (BEC) are the two limiting cases describing the superfluid states of paired fermions. Recently, we have succeeded in inducing the crossover between them in a two-dimensional superconductor,  $\text{Li}_x\text{ZrNCl}$ . It has been demonstrated that a pseudogap phase appears far above the superconducting transition temperature, which reaches 12% of the Fermi temperature.

The condensation of paired fermions is a fundamental phenomenon observed in various systems, such as neutron stars, ultracold atomic gases, and superconductors. There are two limiting cases for the phenomenon in terms of the coupling strength (Fig. 1(a)). Bardeen-Cooper-Schrieffer (BCS) condensation is the weak-coupling or high-density limiting case in which the pairing and superfluidity occur almost simultaneously. Bose-Einstein condensation (BEC) is the strong-coupling or low-density limiting case in which the fermion pairs that are formed at a high temperature condense as the superfluid bosons at low temperature. The intermediate state is referred to as the BCS-BEC crossover. It is intriguing as well as challenging to realize the BCS-BEC crossover using superconductors from the BCS side by controlling the carrier density and the coupling strength. This is because localization effects and magnetic ordering of electrons would impede the realization of such an experiment.

Recently, we have overcome this difficulty with a lithium-intercalated layered nitride,  $\text{Li}_x\text{ZrNCl}$ , where  $\text{Li}^+$  supplies conduction electrons. In this system, the superconducting transition temperature  $T_c$  enhances for lower electron doping concentrations, which is crucial for inducing the BCS-BEC crossover [1]. We performed the simultaneous measurements of resistivity and tunneling spectra using an ionic-gating device with a single crystalline  $\text{ZrNCl}$  (Fig. 1(b)), which was designed for electrochemical intercalation of  $\text{Li}^+$  in the extremely low range ( $0.0038 \leq x \leq 0.28$ ) and showed the maximum  $T_c = 19$  K at  $x = 0.011$  [2]. From these experiments, we obtained the electric phase diagram as shown in Fig. 1 (c), where  $T/T_F$  is the temperature normalized by the Fermi temperature  $T_F$  and  $\Delta/E_F$  is the coupling strength which increases with decreasing  $x$ . Here,  $\Delta$  is the superconducting gap energy at  $T \rightarrow 0$  K and  $E_F$  is the Fermi energy. Notable features include a remarkable increase in the gap opening temperature  $T^* \gg T_c$ , indicating the

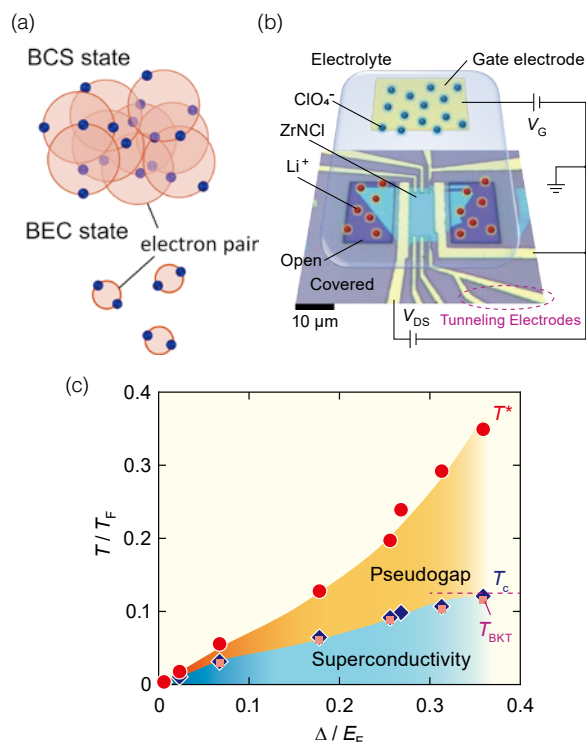


Fig. 1 (a) Schematic concept of BCS state (upper) and BEC state (lower). (b) Ion-gating device designed for  $\text{Li}$  electrochemical intercalation. (c) The phase diagram of the BCS-BEC crossover in  $\text{Li}_x\text{ZrNCl}$  [2].

appearance of a pseudogap phase, and  $T_c/T_F$  approaching 0.125, which is the theoretical upper limit for two-dimensional systems. The findings prove the occurrence of BSC-BEC crossover, indicating that the gate-doped semiconductor provides an ideal platform for observing such exotic phenomena.

## References

- [1] Y. Nakagawa, Y. Saito, T. Nojima, K. Inumaru, S. Yamanaka, Y. Kasahara, and Y. Iwasa, *Phys. Rev. B* **98**, 064512 (2018).
- [2] Y. Nakagawa, Y. Kasahara, T. Nomoto, R. Arita, T. Nojima, and Y. Iwasa, *Science* **372**, 190 (2021).

Tsutomu Nojima (Corresponding Author, Laboratory of Low Temperature Materials Science)

E-mail: t.nojima@tohoku.ac.jp

Takahiko Sasaki (Head of Laboratory of Low Temperature Materials Science)

E-mail: takahiko.sasaki.d3@tohoku.ac.jp

URL: <http://ltsd.imr.tohoku.ac.jp/index-e.html>



# Research Facility for Physics and Chemistry of Radioactive and Nuclear Materials

## Laboratory of Alpha-Ray Emitters

More than 170 species of radioisotopes and nuclear materials are available for study at the Laboratory of Alpha-Ray Emitters. This laboratory is one of the most important centers worldwide for studying the physical and chemical properties of radioactive materials such as actinide compounds. Researchers from many leading universities and institutes all over Japan visit this facility every year to prepare a variety of materials and conduct chemical and physical experiments.

The Laboratory of Alpha-Ray Emitters provides a research environment for the study of 170 radionuclides and elements, especially alpha-ray emitters, such as actinide. This lab functions as a source for the preparation of pure crystals of actinide compounds, providing them to other universities and to synchrotron particle accelerators. In the past decade, actinium-225 (Ac-225), one of the actinides, has been provided as an inter-university collaboration to other universities and research centers. The radiation-controlled area of this laboratory includes three chemical rooms, three physical rooms, and other facilities that are equipped with local exhaust ventilation systems, making the handling of various kinds of radioactive material possible. Many spectrometers, including those for gamma rays and alpha rays, are available.

Hydrothermal synthesis in supercritical water has been widely used to produce nanoparticles of single and complex metal oxides. The size, shape, and physical properties of the nanoparticles were adjusted by adding bases or acids to the starting solutions. Based on this knowledge, a modified hydrothermal synthesis is useful for the preparation of  $\text{UO}_2$  with a fluorite-type crystal structure, which is widely used as a fuel in light-water nuclear reactors because of its high melting point.

In the present work, a series of syntheses of  $\text{UO}_2$  in supercritical water using ethanol and other organic substances as additives were demonstrated, and the possibility of controlling the particle size and shape was studied [1]. In the absence of organic additives, uranium(IV) was oxidized to uranium(VI) by nitrate ions, and  $\text{UO}_3$  was formed. In contrast, the oxidation of uranium(IV) was suppressed in the presence of additives such as aldehydes, and  $\text{UO}_{2+x}$  was formed (Fig. 1). Oxidation reduction of uranium occurred in the presence of aldehydes, which buffered the nucleation and crystal growth. As a result,  $\text{UO}_{2+x}$  crystals grew, whereas  $\text{ThO}_2$  did not. From these results, a reaction mechanism for the formation of uranium dioxide from uranyl nitrate with the intervention of organic additives such as aldehydes was proposed, as shown in Fig. 2. Finally, in the presence of

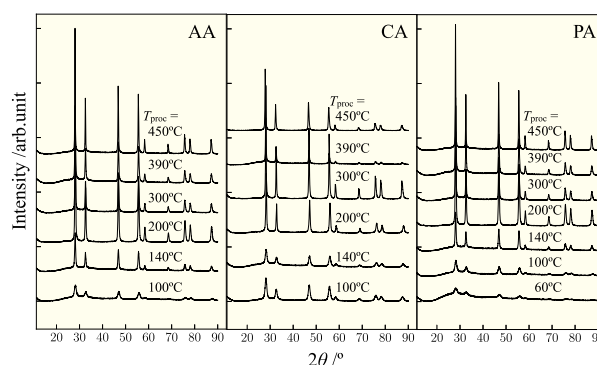


Fig. 1 XRD patterns of prepared  $\text{UO}_{2+x}$  with various organic additives.

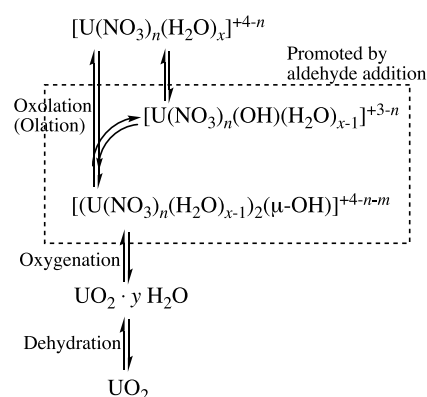


Fig. 2 Proposed reaction mechanism for the formation of  $\text{UO}_2$  from uranyl nitrate via the intervention of organic additives such as aldehydes.

propionaldehyde (PA), acetaldehyde (AA), or cyclohexanecarboxaldehyde (CA), oxygenation to form  $\text{UO}_{2+x}$  occurred at 100 °C. By contrast, the addition of an organic additive did not promote the hydrothermal reaction of  $\text{ThO}_2$ . In the hydrothermal synthesis of  $\text{UO}_{2+x}$ , an oxygenation mechanism accompanied by oxidation-reduction played an important role.

## References

- [1] C. Tabata, K. Shirasaki, A. Sunaga, H. Sakai, D. Li, M. Konaka, and T. Yamamura, *CrystEngComm* **23**, 8660 (2021).

Kenji Shirasaki (Head of Laboratory of Alpha-Ray Emitters)  
E-mail: kenji.shirasaki.e4@tohoku.ac.jp  
URL: <http://alpha.imr.tohoku.ac.jp/en.html>

# Accurate and Precise Chemical Characterizations for Advanced Materials Using Appropriate Sample Preparations in Instrumental Analyses

## Analytical Research Core for Advanced Materials

The Analytical Research Core for Advanced Materials (ARCAM) measures elemental composition data of metal and inorganic materials. Analytical procedures frequently need to be improved to obtain better sensitivity and reliability.

The ARCAM assays major, minor, and trace elements in consigned samples (e.g., Ref. [1]) by using various instrumental analyses (Table 1) and conventional chemical analyses (i.e., gravimetric and titrimetric methods). This report describes recent contributions to improving the analytical procedures.

Specimen pre-treatment of pure iron and stainless-steel samples for low-content oxygen analysis (Fig. 1) have been tested [2]. Chemical and electrochemical polishings were superior to physical polishing for obtaining reliable analytical results.

Appropriate eluents for itaconic acid column in ion chromatography have been confirmed [3]. Nitric acid/18-crown-6-ether was suitable for monovalent and high-content divalent cation, whereas low-content divalent cation required another eluent of copper sulfate/iminodiacetic acid.



Fig. 1 Elemental analyzer for oxygen and nitrogen model ON836 (LECO Corp., United States).

Kawaguchi, H. Tanimura, S. Imashuku, M. Fichtner, and T. Ichitsubo, *Chem. Mater.* **33**, 6983 (2021).

[2] T. Chiba, *Tech. Res. Rep. Tech. Serv. Cent. IMR* **29**, 33 (2020).

[3] Y. Kabasawa, *Tech. Res. Rep. Tech. Serv. Cent. IMR* **29**, 41 (2020).

## References

[1] T. Hatakeyama, H. Li, N. L. Okamoto, K. Shimokawa, T.

Table 1 Methods for chemical characterization.

Analytical method	Instrument
Inductively coupled plasma atomic emission spectrometry (ICP-AES) [1]	AROCS FHM22 MV130 (SPECTRO Analytical Instruments GmbH, Germany) and IRIS Advantage DUO (Thermo Jarrell Ash Corp., United States)
Inductively coupled plasma mass spectrometry (ICP-MS)	iCAP TQ (Thermo Fisher Scientific Inc., United States)
Atomic absorption spectrometry (AAS) [1]	contrAA 800 D (Analytik Jena AG, Germany)
Microwave induced plasma atomic emission spectrometry (MIP-AES)	4210 MP-AES (Agilent Technologies, Inc., United States)
Gaseous analyses (hydrogen, carbon, nitrogen, oxygen, and sulfur) [2]	CS844 (LECO Corp., United States) for carbon and sulfur; ON836 (LECO Corp., United States) for nitrogen and oxygen; and EMGA-821 (HORIBA, Ltd., Japan) for hydrogen
Spectrophotometry	U-2910 (Hitachi, Ltd., Japan)
Ion chromatography [3]	850 Professional IC (Metrohm AG, Switzerland)

Kenichi Nakayama (Corresponding Author, Analytical Research Core for Advanced Materials)

E-mail: ken1naka@tohoku.ac.jp

Toyohiko J. Konno (Head of Analytical Research Core for Advanced Materials)

E-mail: tjkonno@tohoku.ac.jp

URL: <http://www.imr.tohoku.ac.jp/en/about/divisions-and-centers/service-divisions/03.html>



## *International Collaborative Research*

IMR KINKEN Research Highlights 2022



## Giant Spin Hetero-Spin Complex with $S=48$

The third largest spin achieved on a single molecule, of  $S=48$ , was synthesized as a heterometallic system coupling Cr and Gd ions with sizable antiferromagnetic interactions. The structure contained two magnetic cores of  $\text{Cr}_5\text{Gd}_6$ , in which each Cr ion bridged the neighboring Gd ions. The two units were coupled by two additional Gd ions, resulting in an  $S=48$  ground state. The dominant antiferromagnetic interaction and anisotropy were determined by high-field magnetization.

The creation of a giant artificial spin beyond that of natural elements has been an important target of molecular-based compounds. For larger spins, the uncertainty originating from quantum mechanics is smaller, and thus, quantum mechanical manipulation is easier. Moreover, such a giant spin can be a candidate for molecular-based magnetic memory with sizable anisotropy.

There have been several recipes for giant spin synthesis. 3d mixed-valence compounds with ferromagnetic interactions have contained successful examples, such as  $\text{Fe}_{42}$  [1]. The use of rare-earth ions has provided another route for achievement of large molecular moments. Despite the rare successes of homometallic compounds associated with weak exchange interactions, heterometallic compounds are more promising because of their larger exchange interactions. The concept of a heterometallic complex is extended to a radical rare-earth compound, where the radical spins contribute to the connecting block rather than to the size of the total spin.

Here, we investigated a  $\text{Cr}_{10}\text{Gd}_{18}$  cluster consisting of two magnetic cores of  $\text{Cr}_5\text{Gd}_6$ , as shown in Fig. 1. In each core, two Gd ions of  $S=7/2$  were coupled to the  $S=3/2$  Cr ion, and then four  $\text{CrGd}_2$  units were connected through a Cr ion at the center. Strong magnetic coupling between Cr and Gd caused the entire molecule to be an  $S=48$  giant spin cluster.

To examine the magnetic parameters of the system, we measured the magnetization at 0.4 K up to 25 T. The magnetization curve shows two distinct features, namely the low field saturation at around 95  $\mu\text{B}$  and the increase above 8 T. The former shows that the Cr and Gd are antiferromagnetically aligned and form a ferrimagnetic ground state. The latter shows the strength of the antiferromagnetic interactions. The analysis using classical Monte Carlo simulation with a four exchange coupling parameter model shows that the two types of exchange couplings between Cr and Gd are antiferromagnetic and the other two exchange couplings between Gd ions are ferromagnetic. The

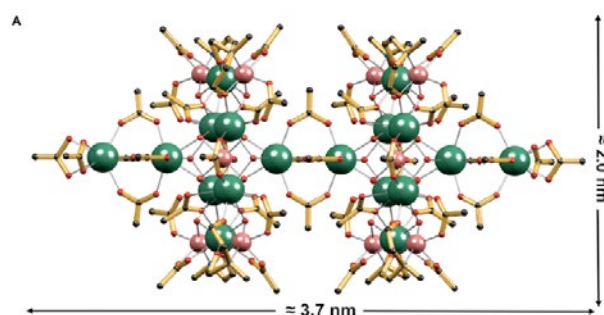


Fig. 1 Schematic view of the  $\text{Cr}_{10}\text{Gd}_{18}$  cluster [2]. Green and pink balls are Gd and Cr ions, respectively.

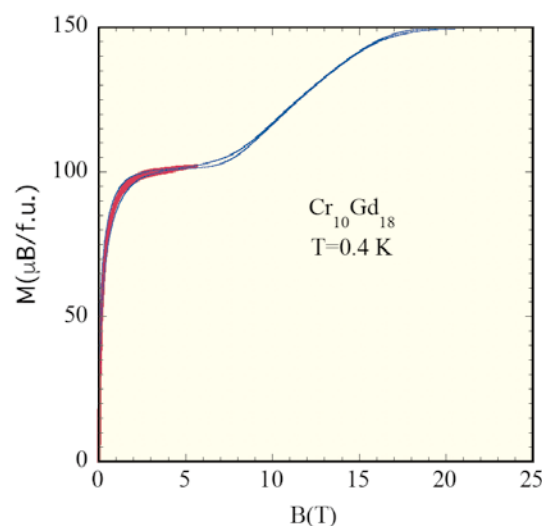


Fig. 2 Magnetization curve of  $\text{Cr}_{10}\text{Gd}_{18}$  cluster at 0.4 K [2].

presence of four different exchange coupling as well as the anisotropy causes the magnetization curve to be linear between 8 and 18 T.

It is notable that both Cr and Gd have very isotropic spins and thus the total spin of  $S=48$  represents the ground state of the system. This is an advantage of using Gd without orbital moments.

### References

- [1] S. Kang *et al.*, Nat. Commun. **6**, 5955 (2015).
- [2] L. Qin, H.-L. Shang, Y.-Q. Zhai, H. Nojiri, C. Schröder, and Y.-Z. Zheng, iScience **24**, 102350 (2021).



# Role of Cementite and Retained Austenite in Austenite Reversion from Martensite and Bainite in Fe-2Mn-1.5Si-0.3C Alloy

The effect of cementite ( $\theta$ ) and retained austenite (RA) on the morphology and kinetics of reverted austenite ( $\gamma$ ) in Fe-Mn-Si-C alloys and its mechanisms have not been well understood yet. Therefore, the  $\gamma$  reversion behaviors were comparatively investigated by changing  $\theta$  and RA distributions in initial microstructures in this study. Pre-tempering or prolonged austempering coarsened the  $\theta$  particles, which promoted the formation of globular austenite. Retained austenite inhibited the formation of globular austenite, and the acicular austenite was formed by its thickening.

It is possible to improve fuel consumption and electric power efficiencies as well as the collision safety of automobiles by developing higher strength steels. One of the candidates is the transformation-induced plasticity (TRIP) steel, which contains a large amount of retained austenite (RA) and yields high strength; in addition, it has good ductility for absorption of energy in a collision. TRIP steels are produced by austenite reversion treatment followed by austempering. The mechanical properties of TRIP steel largely depend on the phase fraction and stability of the RA formed during austempering, which are strongly influenced by the composition, size, and morphology of the reverted austenite ( $\gamma$ ). In  $\gamma$  reversion from lath martensite, two typical morphologies, namely, fine acicular and coarse globular, which have different crystal structures and alloying element partitioning were widely observed [1-4]. It was reported that cementite ( $\theta$ ) particles and pre-existed RA play crucial roles in the  $\gamma$  reversion from martensite.  $\theta$  precipitates during the heating of the as-quenched martensite, which can act as a nucleation site for globular  $\gamma$  [4]. Meanwhile, RA enhances the  $\gamma$  memory effect by promoting the formation of acicular  $\gamma$  in the reversion process from martensite.

Therefore, the effects of  $\theta$  and RA on the kinetics and microstructure evolution in austenite reversion of an Fe-2Mn-1.5Si-0.3C (mass%) alloy have been studied by investigating the  $\gamma$  reversion from as-quenched martensite, tempered martensite, and bainite [5].

As shown in Fig. 1, pre-tempering or prolonged austempering coarsened the  $\theta$  particles, which promoted the formation of globular  $\gamma$ . Theoretical calculation showed that the larger  $\theta$  particles with high density increased the nucleation potency of globular  $\gamma$ . Pre-existed RA suppressed the precipitation of  $\theta$  particles, which inhibited the formation of globular  $\gamma$ , and the acicular  $\gamma$  formed by its thickening.

High-temperature pre-tempering or prolonged austempering retarded the reversion kinetics, while low-temperature pre-tempering or the presence of RA have negligible influences on the kinetics. Thermodynamical calculation suggests that the suppression of reversion kinetics by pre-tempering or austempering was not due to its suppression upon nucleation but due to the growth of reverted  $\gamma$ .

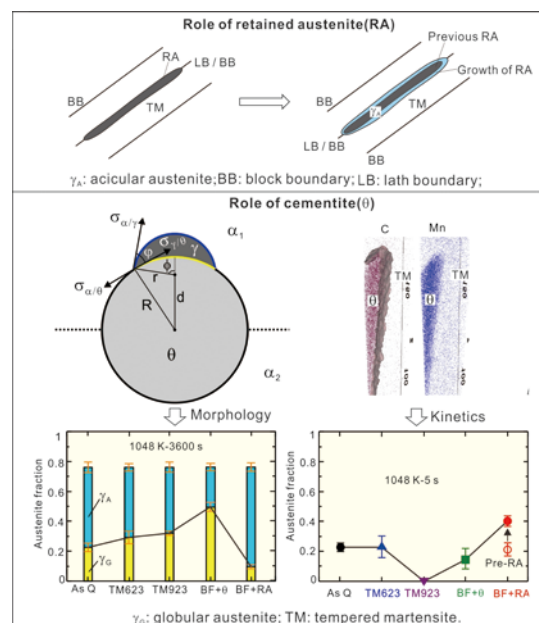


Fig. 1 Schematic illustration of the influences of cementite particles and pre-existed retained austenite on reversion behavior of globular and acicular austenite.

The present results demonstrate that the kinetics and structure of  $\gamma$  reversion can be controlled by changing the microstructure before the reversion treatment, without changing the alloying element or reversion treatment condition. Further, the results guide the design for optimizing the microstructure of the TRIP steels to obtain excellent properties.

## References

- [1] S. Matsuda and Y. Okamura, *Tetsu-to-Hagané* **60**, 226 (1974).
- [2] M. R. Plichata and H. I. Aaronson, *Metall. Trans.* **5**, 2611 (1974).
- [3] X. Zhang, G. Miyamoto, Y. Toji, S. Nambu, T. Koseki, and T. Furuhashi, *Acta Mater.* **144**, 601 (2018).
- [4] X. Zhang, G. Miyamoto, T. Kaneshita, Y. Yoshida, Y. Toji, and T. Furuhashi, *Acta Mater.* **154**, 1 (2018).
- [5] X. Zhang, G. Miyamoto, Y. Toji, Y. Zhang, and T. Furuhashi, *Acta Mater.*, **209**, 116772 (2021).

Goro Miyamoto (Corresponding Author, Microstructure Design of Structural Metallic Materials Research Laboratory)

E-mail: goro.miyamoto.e8@tohoku.ac.jp

Tadashi Furuhashi (Microstructure Design of Structural Metallic Materials Research Laboratory)

E-mail: tadashi.furuhashi.c3@tohoku.ac.jp

URL: <http://www.st-mat.imr.tohoku.ac.jp/en/index.html>

## Development of a Novel Pyrosilicate Scintillator and an Investigation of its Thermal Quenching Mechanism

In order to develop a novel rare-earth (RE) pyrosilicate scintillator, we focused on a complex RE pyrosilicate and grew a Ce-doped  $(\text{La}, \text{Y})_2\text{Si}_2\text{O}_7$  single crystal by the micro-pulling-down method. We succeeded in growing a transparent crystal and found that the thermal quenching of  $\text{Ce}^{3+}$  emission is caused by a combination of thermally activated ionization and thermally activated crossover.

Scintillation crystals convert energy of ionizing radiation to ultra-violet or visible light, and are widely used in radiation detector applications such as oil well logging, medical imaging and high energy physics. We have focused on Ce-doped  $\text{RE}_2\text{Si}_2\text{O}_7$  as promising oxide scintillators, which have excellent scintillation properties but are difficult to grow into single crystals from the melt because of the incongruent melting composition of most  $\text{RE}_2\text{Si}_2\text{O}_7$ . In order to develop  $\text{RE}_2\text{Si}_2\text{O}_7$  single crystals, we designed materials based on Pauling's electrostatic valence rule and demonstrated that a partial substitution of Gd with La in  $\text{Gd}_2\text{Si}_2\text{O}_7$  crystals (Ce:La-GPS) transforms the originally incongruent melting compound to a congruently melting one without any remarkable negative effects [1,2]. In the development of other  $\text{RE}_2\text{Si}_2\text{O}_7$  scintillators, we focused on  $(\text{La}_{0.6}\text{Y}_{0.4})_2\text{Si}_2\text{O}_7$  and tried to grow a single crystal [3].

$(\text{Ce}_{0.015}\text{La}_{0.600}\text{Y}_{0.385})_2\text{Si}_2\text{O}_7$  (Ce:La-YPS) crystal was grown by the micro-pulling-down method and is shown in Fig. 1. The grown crystal was 3.5 mm in diameter and 25 mm in length. In the initially grown section of the crystal (i.e., on the left-hand side of Fig. 1), many micro-cracks were present because of the difference in the lattice constants between the seed crystal and the grown crystal. However, we succeeded in growing a transparent crystal in the central section. The final section of the crystal, as seen on the right-hand side of Fig. 1, was opaque. When the chemical composition of the opaque part in the final section was evaluated, a Si-rich phase and a pyrosilicate phase were detected.

For the evaluation of the thermal quenching

mechanism of Ce:La-YPS, the photoluminescence (PL) decay curves under an excitation by a 339 nm nanosecond LED were measured at different temperatures. These results were fitted with a single-barrier model, and the activation energy of the thermal quenching and the quenching temperature ( $T_{50\%}$ ) were determined to be 0.62 eV and 526 K, respectively. The  $T_{50\%}$  of Ce:La-YPS is relatively high compared to other Ce-doped crystals such as  $\text{Lu}_2\text{SiO}_5$  [4].

The temperature dependence of the background intensity of the PL decay curve is shown in Fig. 2 (a), which indicates that the background intensity increases with an increasing temperature starting from approximately 400 K. This increase is most likely caused by the escape of the electrons from the  $\text{Ce}^{3+} 5d_1$  state into the conduction band, resulting in delayed radiative recombination. Therefore, it is thought that a thermal ionization is one contributor to the thermal quenching mechanism in Ce:La-YPS. Another contributor could be the classical thermal quenching due to the thermally activated nonradiative crossover from the  $\text{Ce}^{3+} 5d_1$  excited level to the 4f ground state.

### References

- [1] A. Yoshikawa, S. Kurosawa, Y. Shoji, V. I. Chani, K. Kamada, Y. Yokota, and Y. Ohashi, *Cryst. Growth Des.* **15**, 1642 (2015).
- [2] M. Nikl and A. Yoshikawa, *Adv. Opt. Mater.* **3**, 463 (2015).
- [3] T. Horiai, J. Paterek, M. Jarosova, J. Rohlicek, S. Kurosawa, T. Hanada, M. Yoshino, A. Yamaji, S. Toyoda, H. Sato, Y. Ohashi, K. Kamada, Y. Yokota, A. Yoshikawa, and M. Nikl, *J. Cryst. Growth* **573**, 126252 (2021).
- [4] V. Babin, V. V. Laguta, M. Nikl, J. Pejchal, A. Yoshikawa, and S. Zazubovich, *Opt. Mater.* **103**, 109832 (2020).



Fig. 1 Grown crystal by micro-pulling-down method

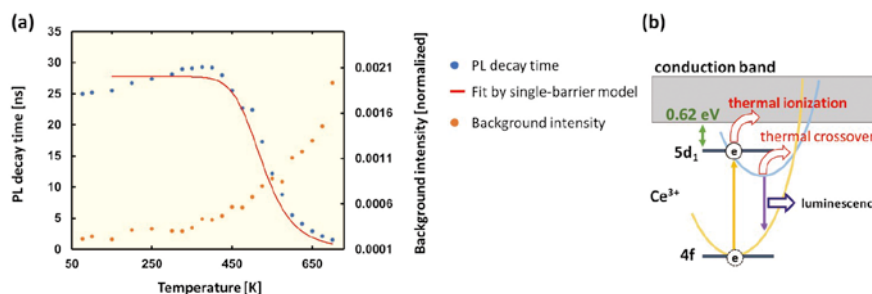


Fig. 2 (a) Temperature dependence of PL decay time and background intensity, (b) schematic view of thermal quenching

Akira Yoshikawa (Advanced Chrystal Engineering Research Laboratory)

E-mail: akira.yoshikawa.d8@tohoku.ac.jp

URL: <http://yoshikawa-lab.imr.tohoku.ac.jp/index-e.html>



## Anomalous Compliance of Interpenetrating-Phase Composite of Ti and Mg Synthesized by Liquid Metal Dealloying

Low modulus biomaterials, which can ensure fast healing of hard tissues are potential candidates for biomedical implants. In this work, a low modulus (17.6 MPa) interpenetrating-phase composite of Ti and Mg, mimicking the elastic behavior of human bone was synthesized. It has been demonstrated that the origin of the low modulus of the composite can be related to a weakened interface between the constituents.

Dealloying-based composites demonstrate a significant deviation of their mechanical behavior from that estimated using various rules of mixtures [1-2]. For example, nanoporous metal and polymer composites are substantially stronger and harder than the individual nanoporous metal or polymer [1]. Moreover, these metal-polymer composites exhibit extremely low Young's modulus values compared with theoretical predictions [1]. In a recent study, it was demonstrated that the Young's modulus of the dealloying-based composite, which contains both Fe and Mg is significantly lower than that of each constituent [2]. This anomalous behavior is associated with interfacial phenomena.

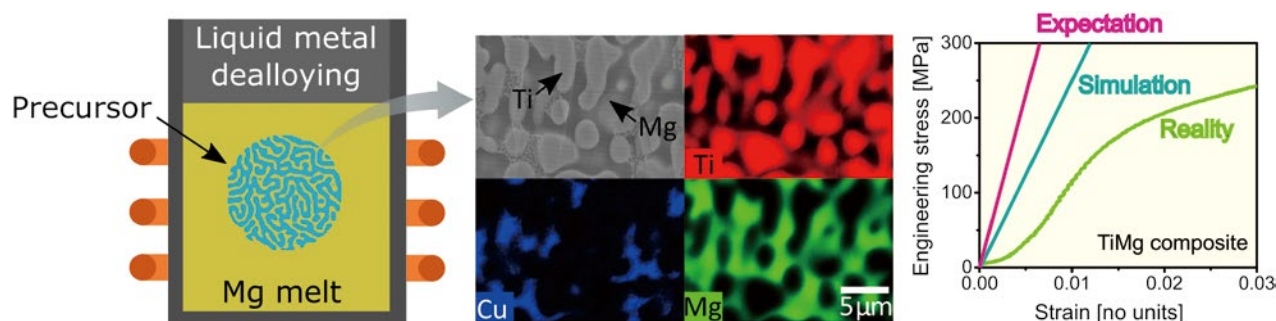
In nanoscale materials, interfaces and interfacial areas play a crucial role in determining the effective mechanical properties of materials. It is possible to account for a significant reduction of Young's modulus compared to perfect cohesion in inclusion composites, which have large interface-to-volume ratios; this is achieved by using interface elasticity theory modeling. The magnitude of the effect depends on the structure morphology and the characteristic length scale; that is, with increasing structure size, the interfacial influence on the effective modulus decreases.

The characteristic length scale in the recent dealloying-based interpenetrating-phase Ti-Mg composite that possesses an anomalously low

effective elastic modulus is in the micron-scale regime [3], which is several orders of magnitude higher compared to the abovementioned nanomaterials; this indicates a different origin of a low modulus value. The composite of Ti and Mg (synthesized by liquid metal dealloying) features an anomalously low Young's modulus of  $17.6 \pm 0.5$  GPa (several times lower than that of each constituent) and moderate yield strength of  $180 \pm 10$  MPa [3]. The origin of the anomalously low modulus is associated with the weak interface between constituent Ti and Mg phases, as confirmed using micromechanical modeling. The result suggests that even moderate porosity in the Ti-Mg composite affects the overall behavior drastically if localized, e.g., homogeneously distributed at the interface. This localized porosity is likely due to the shrinkage of the Mg phase upon solidification and unequal shrinkage of the Ti and Mg phases upon cooling, caused by unequal coefficients of volumetric thermal expansion.

### References

- [1] A.V. Okulov, A.S. Volegov, J. Weissmüller, J. Markmann, and I.V. Okulov, *Scripta Mater.* **146**, 290294 (2018).
- [2] I.V. Okulov, P.-A. Geslin, I.V. Soldatov, H. Ovri, S.-H. Joo, and H. Kato, *Scripta Mater.* **163**, 133136 (2019).
- [3] I.V. Okulov, J. Wilmers, S.-H. Joo, S. Bargmann, H. S. Kim, and H. Kato, *Scripta Mater.* **194**, 113660 (2021).



Ilya Okulov (Corresponding Author, Leibniz-Institut für Werkstofforientierte Technologien – IWT Bremen)

E-mail: i.okulov@iwt.uni-bremen.de

Hidemi Kato (Non-Equilibrium Materials Research Laboratory)

E-mail: hidemi.kato.b7@tohoku.ac.jp

URL: <http://www.nem2.imr.tohoku.ac.jp/index-e.html>

## Evaluation of Edge Domains in Giant Magnetoresistive Junctions

In nanoelectronic devices, miniaturization increases the total length of the current paths and the associated Joule heating. Even with optimization of the chip design, waste heat cannot be ignored in the total power consumption of the device. In this work, we propose a new method to use the waste heat to generate additional spin-transfer torque in a magnetic insulator to assist current-induced magnetization reversal used in magnetic random access memory, which meets the policy of sustainable development recently set by the United Nations.

Recent progress in spin caloritronics has revealed that spin waves can be efficiently induced in a magnetic insulator [1, 2], which can be used for energy harvesting. However, the spin-transfer torque induced by spin waves has not been investigated. In this study [3], we demonstrated spin-wave-assisted magnetization reversal in a current-perpendicular-to-plane (CPP) giant magnetoresistive (GMR) nanopillar.

A GMR multilayer, consisting of  $\text{Co}_2\text{Fe}_{0.4}\text{Mn}_{0.6}\text{Si}$  (CFMS) (5)/ $\text{Ag}_{0.78}\text{Mg}_{0.22}$  (5)/CFMS (5), was grown on a Cr (20)/Ag (40) seed layer on a MgO(001) substrate by ultrahigh vacuum magnetron sputtering (all thicknesses are given in nanometers). The Heusler-alloy CPP-GMR junction was then patterned into elongated nanopillars with long axes between 100 and 800 nm using photo- and electron-beam lithography, as well as Ar-ion milling. These nanopillars were encapsulated by a 5-nm-thick magnetic insulator of  $\text{Fe}_2\text{O}_3$  with a Cr (1)/AlO (2) layer to enhance adhesion, followed by the top electrode of Ag (2)/Au (5). The magnetic transport properties were measured using a probe station in both field- and current-induced modes.

The CPP-GMR junctions were evaluated in a standard manner using an applied external field. With  $\text{Fe}_2\text{O}_3$ , an asymmetric GMR curve was obtained with GMR ratios of  $(32.8 \pm 0.1)\%$  and  $(10.2 \pm 0.1)\%$ . This asymmetry was induced by the formation of edge domains coupled with the spin-wave induced in  $\text{Fe}_2\text{O}_3$ , as shown in Fig. 1(a). Without  $\text{Fe}_2\text{O}_3$ , a symmetric GMR curve was observed, as shown in Fig. 1(b).

In Fig. 1(c), the corresponding current-induced magnetization reversal was measured under a magnetic field of -10 Oe, forming an antiparallel configuration. The switching current density was estimated to be  $(8.0 \pm 0.7) \times 10^7 \text{ A/cm}^2$  owing to (i) conventional spin-transfer torque by the pinned layer, and (ii) the influence of the edge domains exchange-coupled with a spin wave in  $\text{Fe}_2\text{O}_3$ . Here, current-induced magnetization switching from parallel to antiparallel configurations could not be achieved because of contribution (ii).

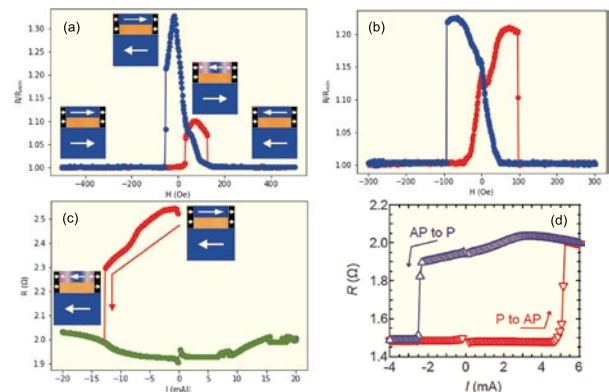


Fig. 1 GMR curves for a pillar (120 and 60 nm in long and short axes, respectively) (a) with and (b) without  $\text{Fe}_2\text{O}_3$  with a sensing current of 100  $\mu\text{A}$ . The corresponding current-induced magnetisation switching profiles (c) with  $\text{Fe}_2\text{O}_3$  under a magnetic field of -10 Oe and (d) without  $\text{Fe}_2\text{O}_3$  under a field of 3 Oe.

Without  $\text{Fe}_2\text{O}_3$ , the current switching in Fig. 1(d) is dominated by contribution (i), with switching current densities of  $(1.1 \pm 0.1) \times 10^7 \text{ A/cm}^2$  and  $(2.2 \pm 0.2) \times 10^7 \text{ A/cm}^2$  for the negative and positive currents, respectively.

These results indicate that the presence of the spin wave in  $\text{Fe}_2\text{O}_3$  can assist in magnetization reversal only when the spin wave is parallel to the free-layer magnetization. By comparing Figs. 1(c) and (d), the edge domain volume can be estimated to be almost 1/3 of that of the free layer. Further control of the GMR behavior can be achieved to reduce the power consumption in magnetization reversal.

### References

- [1] H. Chang, P. A. Praveen Janantha, J. Ding, T. Liu, K. Cline, J. N. Gelfand, W. Li, M. C. Marconi, and M. Wu, *Sci. Adv.* **3**, e1601614 (2017).
- [2] P. Jiménez-Cavero, I. Lucas, A. Anadón, R. Ramos, T. Niizeki, M. H. Aguirre, P. A. Algarabel, K. Uchida, M. R. Ibarra, E. Saitoh, and L. Morellón, *APL Mater.* **5**, 026103 (2017).
- [3] W. Frost, T. Seki, T. Kubota, R. Ramos, E. Saitoh, K. Takanashi, and A. Hirohata, *Appl. Phys. Lett.* **118**, 172405 (2021).

Atsufumi Hirohata (Corresponding Author, University of York)

E-mail: atsufumi.hirohata@york.ac.uk

Koki Takanashi and Takeshi Seki (Magnetic Materials Research Laboratory)

E-mail: koki.takanashi.d2@tohoku.ac.jp, takeshi.seki@tohoku.ac.jp

URL: <http://magmatelab.imr.tohoku.ac.jp/>



# Alloying Effects on Deuterium Retention in Ion-Irradiated Tungsten

International Research Center for Nuclear Materials and Science

The alloying effects of molybdenum, tantalum, and rhenium on deuterium retention in ion-irradiated tungsten alloys were investigated. A significant decrease of irradiation-induced deuterium retention by rhenium doping was observed, but there were almost no effects in molybdenum and tantalum doping. This was attributed to the interaction between solute and irradiation-induced defects.

Tungsten (W) and its alloys are recognized as leading candidates for plasma-facing material in a fusion reactor because of their attractive physical and chemical properties, such as high melting point, high thermal conductivity, high threshold energy for sputtering and low solubility of hydrogen isotopes. During service in a fusion reactor, W experiences irradiation of high-energy neutrons and energetic particles of deuterium (D) and tritium (T). High-energy neutrons induce displacement damage in W. Previous neutron-irradiation experiments have shown that irradiation-induced defects in pure W act as strong traps for hydrogen isotopes, and hence neutron irradiation should lead to a significant increase in T inventory in the vacuum vessel of a fusion reactor. Here, we investigated the effects of alloying elements such as molybdenum (Mo), tantalum (Ta), and rhenium (Re) on the retention of hydrogen isotopes in W after irradiation.

The samples were plates of W-2.5%Mo, W-5%Ta, and W-5%Re alloys (in atomic percent). They were heated in vacuum at 1273 K for 1 h to relieve strain potentially induced during fabrication and to remove hydrogen present in the samples as an impurity. Displacement damages were induced by irradiation of 6.4 MeV iron (Fe) ions to 0.26 dpa at 1073 K by using the Dual-Beam Facility for Energy Science and Technology at Kyoto University. The depth of the damaged region was estimated to be  $\sim 2 \mu\text{m}$  using Monte Carlo simulation. The irradiated samples were exposed to  $\text{D}_2$  gas at 0.1 MPa at 673 K for 10 h. The D retention was then measured with thermal desorption spectrometry (TDS), as shown in Fig. 1. The D retention in the non-irradiated W sample was small but it increased significantly after Fe ion irradiation due to the trapping effect of irradiation-induced defects. The irradiated W-5Ta and W-2.5Mo alloys showed D retention comparable with that of irradiated W [2], while the D retention in irradiated W-5Re alloy was far smaller [1]. As previously mentioned, the thickness of the damaged zone was  $\sim 2 \mu\text{m}$ , while the sample thickness was 500  $\mu\text{m}$ . Both the damaged zone and the non-irradiated volume therefore contributed to thermal desorption spectra. Hence, the D retention in the damaged zone was evaluated as the difference in D retention between non-irradiated and irradiated samples of the same material, as shown in Fig. 2. The addition of Re was effective in mitigating the irradiation-

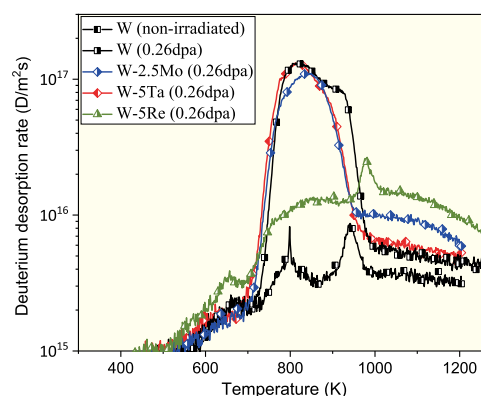


Fig. 1 Desorption spectra of D by TDS measurement. [1,2]

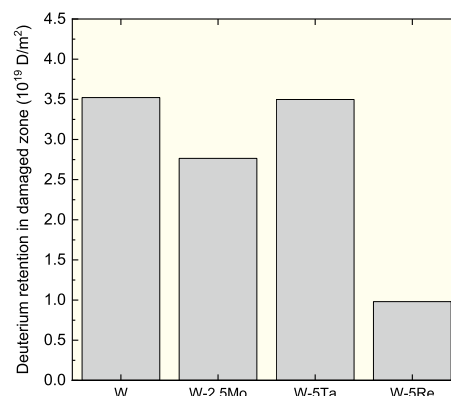


Fig. 2 Deuterium retention in W and W alloys.

induced increase in hydrogen isotope retention, while Mo and Ta showed no significant effects [1, 2]. These observations roughly agreed with the order of binding energy of a solute atom and W self-interstitial atom reported by Suzudo et al. in Ref. [3].

## References

- [1] Y. Hatano, K. Ami, V. K. Alimov, S. Kondo, T. Hinoki, T. Toyama, M. Fukuda, A. Hasegawa, K. Sugiyama, Y. Oya, M. Oyaidzu, and T. Hayashi, *Nucl. Mater. Energy*, **9**, 93 (2016).
- [2] J. Wang, Y. Hatano, T. Hinoki, V. Kh. Alimov, A. V. Spitsyn, N. P. Bobyr, S. Kondo, T. Toyama, H. T. Lee, Y. Ueda, and T. Schwarz-Selinger, *J. Nucl. Mater.*, **545**, 152749 (2021).
- [3] T. Suzudo, T. Tsuru, and A. Hasegawa, *J. Nucl. Mater.*, **505**, 15 (2018).

Yuji Hatano (Corresponding Author, University of Toyama)

E-mail: hatano@ctg.u-toyama.ac.jp

Yasuyoshi Nagai (Head of International Research Center for Nuclear Materials and Science)

E-mail: yasuyoshi.nagai.e2@tohoku.ac.jp

URL: <http://www.imr-oarai.jp/en/>



# Determination of Magnetic, Electronic and Lattice Contributions to Low-Temperature Specific Heat

Cooperative Research and Development Center for Advanced Materials

The separation of magnetic and non-magnetic contributions to the specific heat of ferromagnetic (FM) solids was applied to Ni-Mn-In alloys. It is shown that the disregard of magnetic contribution results in a noticeable underestimation of the Debye temperature and overestimation of the specific heat of the electron subsystem of a FM solid.

Experimental and theoretical research has shown that the low-temperature state of  $\text{Ni}_{50}\text{Mn}_{50-x}\text{In}_x$  alloys is ferromagnetic (FM) austenite if  $x > 16$  and antiferromagnetic (AFM) martensite if  $x < 15$  (see [1,2] and references therein). The specific heat of  $\text{Ni}_{50}\text{Mn}_{50-x}\text{In}_x$  alloys was measured at low temperatures in a wide composition range [1]. It has been shown that the specific heat value measured for  $\text{Ni}_{50}\text{Mn}_{50-x}\text{In}_x$  alloys with  $x < 15$  was significantly different from that measured for alloys with  $x > 16$  [1].

The low-temperature specific heat of a magnetic solid can be expressed by a sum

$$C(T) = \gamma T + \beta T^2 + C_M(T), \quad (1)$$

where the first summand is the specific heat of the electronic subsystem, the second summand is a Debye term describing the specific heat of the crystal lattice and the third summand describes the specific heat of magnetic excitations (magnons) [2]. In the absence of the magnetic term, the  $C(T)/T$  is a linear function of  $T^2$ . In this connection the coefficients  $\beta$  and  $\gamma$  are usually determined as the slope and intercept of experimental  $C(T)/T$  vs  $T^2$  dependence. The Debye temperature  $T_D$  is then estimated from the determined  $\beta$  value.

It was shown very recently that the determination of  $\beta$  and  $\gamma$  values is impossible if  $C_M(T)$  is disregarded [2]. This conclusion is explained here for the FM phase of  $\text{Ni}_{50}\text{Mn}_{50-x}\text{In}_x$ .

For an FM solid, the specific heat of magnetic excitations is equal to  $C_M(T) = K_{\text{FM}} T^{3/2}$ , where the temperature-independent coefficient  $K_{\text{FM}}$  is inversely proportional to the third power of the Curie temperature (see [2] and references therein). Figure 1 shows experimental and theoretical determinations of the total  $C(T)/T$  value vs  $T^2$  obtained for the ferromagnetic state of an  $\text{Ni}_{50}\text{Mn}_{33.8}\text{In}_{16.2}$  alloy ( $x = 16.2$ ). The magnetic and electronic contributions to the  $C(T)/T$  function are shown for comparison. It is seen that the magnetic contribution exceeds all others in the temperature range from 2 K to 8 K. Due to this, the value  $\gamma = 2.3 \text{ mJ}(\text{mol})^{-1}\text{K}^{-2}$ , determined by the Eq. (1) fit is strongly different from the value of  $5.1 \text{ mJ}(\text{mol})^{-1}\text{K}^{-2}$  that results

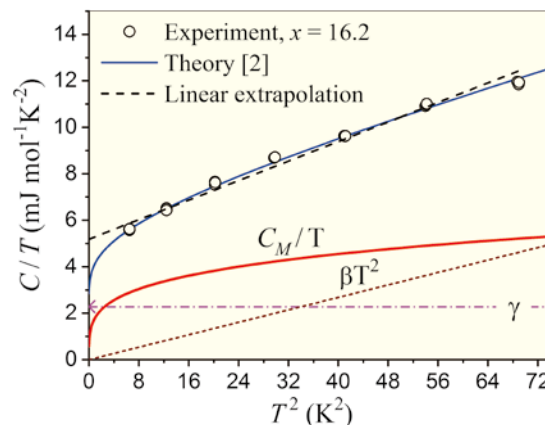


Fig. 1 The experimental (open circles) and theoretical (lines) dependencies of  $C(T)/T$  ratio on the squared temperature determined for  $\text{Ni}_{50}\text{Mn}_{33.8}\text{In}_{16.2}$  alloy. Magnetic (red solid line), electronic (pink dashed line) and lattice contributions (brown dotted line) to this ratio are shown for comparison.

from the linear extrapolation of experimental dependence  $C(T)/T$  to zero temperature. The difference is caused by the magnetic contribution to specific heat, which, in turn, causes the noticeable nonlinearity of  $C(T)/T$  vs  $T^2$ .

For the AFM phase of  $\text{Ni}_{50}\text{Mn}_{50-x}\text{In}_x$  with  $x < 15$ , the magnetic contribution strongly depends on the Néel temperature  $T_N$  [2]. This contribution exceeds the Debye term if  $T_N < 0.3T_D$ . The magnon and lattice contributions to the specific heat are cubic functions of the temperature, and so the separation of these contributions from the specific heat of an AFM solid is an open problem.

It can be concluded that the magnetic subsystem noticeably contributes to the low-temperature specific heat and cannot be disregarded.

## References

- [1] R. Y. Umetsu, X. Xu, W. Ito, and R. Kainuma, *Metals* **7**, 414 (2017).
- [2] A. Kosogor, V.A. L'vov, R.Y. Umetsu, X. Xu, and R. Kainuma, *J. Magn. Magn. Mater.* **541**, 168549 (2022).

Anna Kosogor (Corresponding Author, Institute of Magnetism National Academy of Sciences of Ukraine)

E-mail: annakosogor@gmail.com

Naoya Masahashi (Head of Cooperative Research and Development Center for Advanced Materials)

E-mail: naoya.masahashi.e6@tohoku.ac.jp

URL: <http://www.crdam.imr.tohoku.ac.jp/en/index-en.html>

# Spin Reorientation and Unusual Tetra-Critical Point in $\text{MnCr}_2\text{S}_4$

## High Field Laboratory for Superconducting Materials

The high magnetic phase diagram of the spinel compound  $\text{MnCr}_2\text{S}_4$  was investigated by combining element-specific magnetization measurements of X-ray magnetic circular dichroism (XMCD) and macroscopic thermodynamic measurements. The re-orientation of the sublattice magnetic moments was determined by XMCD and combined with macroscopic results. The present study shows the importance of the combination of microscopic and macroscopic analyses, which has been enabled by the collaboration of several laboratories.

Spinel compounds exhibit a variety of physical properties owing to spin-lattice coupling and competition for exchange interactions.  $\text{MnCr}_2\text{S}_4$  has strong spin frustrations and shows successive phase transitions from paramagnetic to ferrimagnetic at 65 K and then to a canting phase at 5 K. Sequential phase transitions occur at 3.5 T, 11 T, and 23.5 T. To understand this complicated magnetization process, we used the bridge proposal of GIMRT to combine measurements in high-field laboratories and the 40 T soft X-ray magnetic circular dichroism at SPring8.

Figure 1 shows the XMCD at the  $L_3$  edge of Mn [1]. At low temperatures, a few anomalies of the Mn signal were observed, indicating rearrangement of the Mn spins. In contrast, the Cr signal decreased toward 11 T and then increased again. It clearly shows the complex process of increasing tilt from the external magnetic field and then re-aligning along it. Detailed investigations indicated that this material has a quadruple critical point.

Generally, a quadruple critical point is not expected in an isotropic spin system with three sites. In this material, ultrasonic anomalies have been observed in the phase transition; therefore, the existence of spin-lattice coupling is considered to be the key. In such a case, the Monte Carlo calculation shows that the symmetry of  $Z_2$  is spontaneously broken and a staggered magnetic field of two components causes the phase diagram to have a tetra-critical point owing to the interplay of the symmetries of  $O(3)$  and  $O(2)$  and the recovery of  $O(2)$  symmetry above 23.5 T.

The present result shows the complexity of spinel compounds as well as the potential tuning of their magnetic properties by spin-lattice coupling.

### References

- [1] S. Yamamoto, H. Suwa, T. Kihara, T. Nomura, Y. Kotani, T. Nakamura, Y. Skourski, S. Zherlitsyn, L. Prodan, V. Tsurkan, H. Nojiri, A. Loidl, and J. Wosnitza, *Phys. Rev. B* **103**, L020408 (2021).

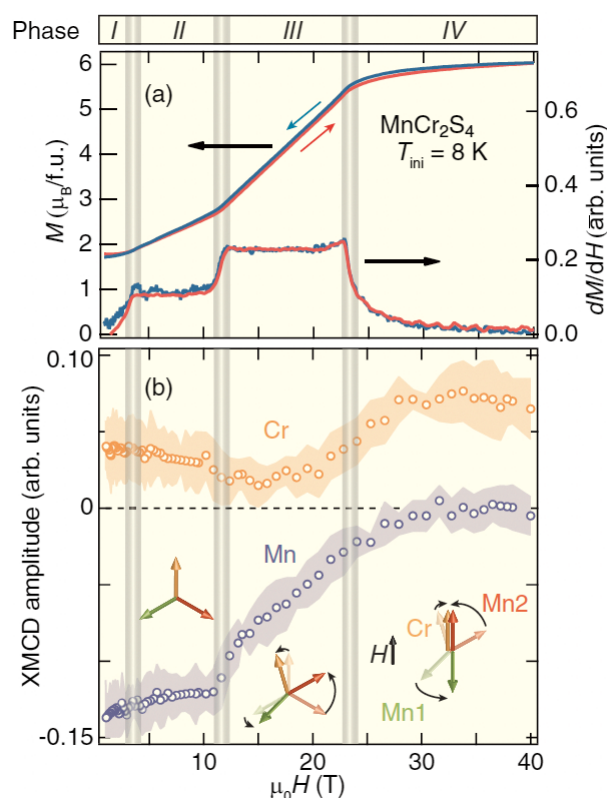


Fig. 1 Magnetic field dependence of Mn and Cr  $L_3$  edge XMCD signal compared with macroscopic magnetization curve. After Ref. [1].

Hiroyuki Nojiri (Head of High Field Laboratory for Superconducting Materials)

E-mail: hiroyuki.nojiri.e8@tohoku.ac.jp

URL: <http://www.hflsm.imr.tohoku.ac.jp/cgi-bin/index-e.cgi>

# Ab Initio Design of Effective Magnetostriction Materials for Electric Power Generation

Center for Computational Materials Science

Although magnetostriction is expected to contribute to electric power generation in SDGs, it is still necessary to increase the magnetostriction coefficient. We theoretically investigated the efficient doping effect in a Ga-Fe magnetostriction alloy (galfenol). Transition metal elements were unsuccessful, but La-doped galfenol showed a satisfactory increase in the magnetostriction property.

Materials with large magnetostrictions are extensively used as magnetic field sensors, magneto-mechanical actuators, and energy harvesters. A large (and preferably linear) magnetic field response is essential. Here, we proposed a consistent description of the effect of various types of doping with transition metals (TM) and rare-earth (RE) elements. We explain why the experimentally measured values of the  $\lambda_{001}$  coefficients did not change or even decreased in the case of TM doping, whereas in the RE type of doping, they increased.

The first-principles calculations of the structural and magnetic properties of the Fe-Ga alloy systems were performed using the Vienna Ab initio Simulation Package (VASP) with the supercell approach. A  $4 \times 4 \times 4$  cubic supercell (128 atoms/cell) was used for modeling. In the Fe-Ga alloy with an A2 structure (Fig. 1(a)), the probability of finding Ga atoms at neighboring sites is negligible. There are two types of Fe atoms in the Fe-Ga alloy: those with Ga atoms in the nearest-neighbouring positions (Fe(1)) and those with Ga atoms in the next-nearest-neighbouring positions (Fe(2)). The fundamental difference is that the density of antibonding  $d$ -states (DOS) on atoms of the Fe(1) type is much higher than that on atoms of the Fe(2) type. We focused on two limiting configurations, referred to as structures A and B. The Fe(1) atom was replaced, and there were no Ga atoms around the dopant (type A, Fig. 1(b)). The Fe(2) atom with four Ga atoms in the nearest neighboring positions was substituted (type B, Fig. 1(c)).

The simulation revealed two factors that affected magnetostriction [1]. First, it was energetically favorable for TM and La atoms to have a different local environment relative to atoms of the host lattice. The La atom preferentially occupied a position in the lattice surrounded only by Fe atoms, whereas TM atoms occupied sites in a local environment of four Fe atoms and four Ga atoms. The atoms closest to the

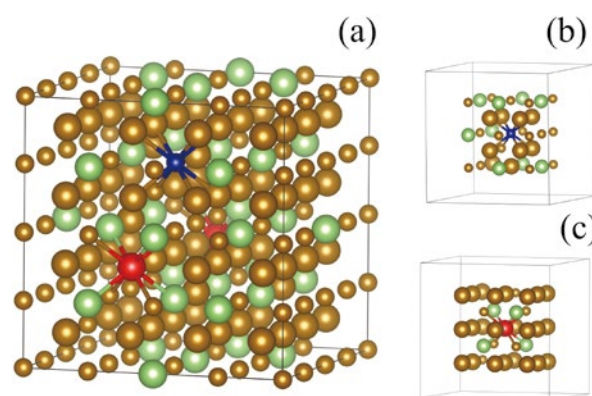


Fig. 1(a) Atomic configuration of  $\text{Fe}_{84.4}\text{Ga}_{14.8}\text{X}_{0.8}$ . Local atomic ordering around the dopant atoms in first and second coordination spheres for structures of (b) type A and (c) type B.

dopant Fe atoms had different electronic properties. Second, the Fe atoms of the first and second coordination shells changed their electronic properties differently, depending on the type of local ordering and impurities. The increase in magnetostriction owing to the antibonding nature of the Fe-TM bond was partially compensated by a decrease in  $\text{DOS}_{\text{Fe}(d)}$  (type A ordering) or a low  $\text{DOS}_{\text{Fe}(d)}$  (type B) near the Fermi level. The stronger bonding nature of the interaction between the Fe atoms of the first and second coordination spheres also reduced  $\lambda_{001}$ . In La-doping, the La-Fe bond has a binding character in the local ordering of type A and antibonding in structure B. Because the Fe-Fe interaction between atoms in the dopant's first and second coordination spheres is antibonding, it should enhance  $\lambda_{001}$ . The results obtained explained the experimental observations.

## References

- [1] T. Inerbaev, A. Abuova, Y. Kawazoe, and R. Umetsu, *Comp. Mater. Sci.* **202**, 110934 (2022).

Talgat Inerbaev (Corresponding Author, L.N. Gumilyov Eurasian National University)

E-mail: talgat.inerbaev@gmail.com

Momiji Kubo (Head of Center for Computational Materials Science)

E-mail: momiji@tohoku.ac.jp

URL: <http://www.sc.imr.tohoku.ac.jp/eng/>



## Post-Growth Annealing Effect on Electronic State in $T'$ -Type $R_2\text{CuO}_4$

### Center of Neutron Science for Advanced Materials

Among the single-layer  $R_2\text{CuO}_4$  ( $R$ : rare earth) with three structural isomers, the  $T$ -type cuprate with four oxygen atoms coordinated around the Cu ion exhibits superconductivity due to post-growth annealing. Therefore, it is essential to clarify the role of annealing in the ground state. Here, we studied the annealing effects on the electronic state by X-ray scattering measurements and revealed that the anneal-induced doping of electrons in  $\text{La}_{1.8}\text{Eu}_{0.2}\text{CuO}_4$  is associated with the appearance of superconductivity.

Superconductivity in cuprate oxides has been attributed to carrier doping into Mott insulators. However, after the report of superconductivity in  $R_2\text{CuO}_4$  ( $R$ : rare earth element) without effective carrier doping, the variety of ground states in  $R_2\text{CuO}_4$  has attracted tremendous attention. The importance of the coordination of oxygen atoms around the Cu ions on the physical properties was highlighted, and  $R_2\text{CuO}_4$  with a  $T'$ -type structure (four oxygen coordination) can have a metallic ground state. However, since post-growth annealing treatment is necessary for the emergence of superconductivity in a  $T'$ -type structure, the actual ground state of  $R_2\text{CuO}_4$  remains controversial.

To clarify the role of annealing and the ground state of  $R_2\text{CuO}_4$ , we performed complementary X-ray scattering measurements on  $\text{La}_{1.8}\text{Eu}_{0.2}\text{CuO}_4$  (LECO) and  $\text{Nd}_2\text{CuO}_4$  (NCO) [1, 2]. The former exhibits superconductivity due to annealing, whereas the latter is a non-superconductor even after annealing. Therefore, a comparison of the results would provide crucial information.

Figure 1 shows the Cu  $L_3$ -edge resonant inelastic X-ray scattering (RIXS) spectra of the as-grown and annealed NCO. The variation in the spectra due to annealing is quite similar to that induced by Ce doping, suggesting electron doping in the annealing procedure. Consistent results for NCO were obtained using Cu  $K$ -edge X-ray absorption near-edge structure (XANES) measurements (Fig. 2). However, the spectral change due to annealing was much more drastic in LECO. The number of induced electrons due to annealing is  $\sim 0.4$  and  $\sim 0.05$  per Cu atoms in LECO and NCO, respectively, while the removed oxygen value is comparable [3]. These results suggest distinct electron-doping processes in the two compounds and that a variation in the electronic band structure causes self-doping of carriers in LECO.

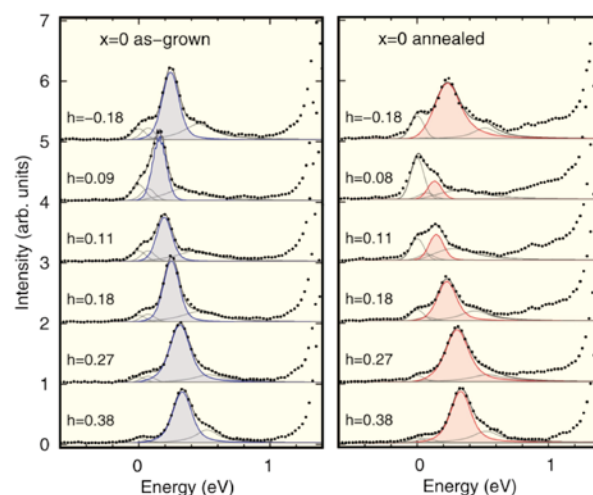


Fig. 1 Cu  $L_3$ -edge RIXS spectra of as-grown and annealed  $\text{Nd}_{2-x}\text{Ce}_x\text{CuO}_4$  with  $x = 0$  [1].

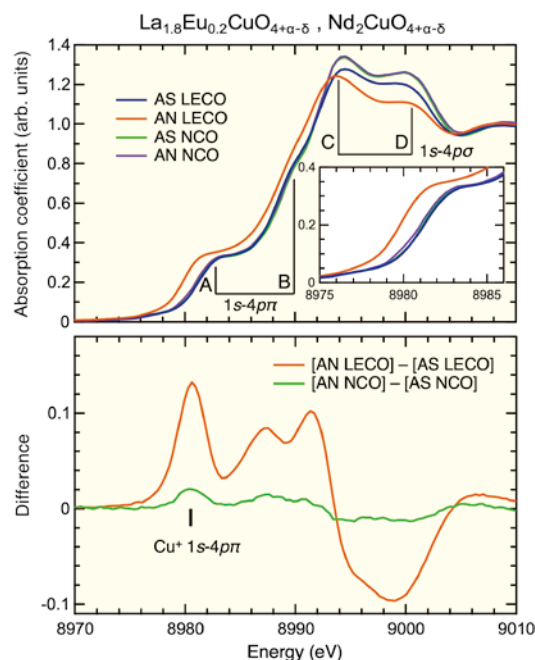


Fig. 2 Cu  $K$ -edge XANES spectra of as-grown and annealed  $\text{La}_{1.8}\text{Eu}_{0.2}\text{CuO}_4$  and  $\text{Nd}_2\text{CuO}_4$  [2].

Kawamata, T. Takamatsu, T. Adachi, M. Kato, and Y. Koike, J. Phys. Soc. Jpn. **90**, 105002 (2021).

## References

- [1] K. Ishii, S. Asano, M. Ashida, M. Fujita, B. Yu, M. Greven, J. Okamoto, D.-J. Huang, and J. Mizuki, Phys. Rev. Materials **5**, 024803 (2021).
- [2] S. Asano, K. Ishii, D. Matsumura, T. Tsuji, K. Kudo, T. Taniguchi, S. Saito, T. Sunohara, T. Kawamata, Y. Koike, and M. Fujita, Phys. Rev. B **104**, 214504 (2021).
- [3] M. Fujita, T. Taniguchi, T. Wang, S. Torii, T. Kamiyama, K. Ohashi, T.

Masaki Fujita (Head of Center of Neutron Science for Advanced Materials)

E-mail: masaki.fujita.b5@tohoku.ac.jp

URL: <http://nc-imr.imr.tohoku.ac.jp/index-e.html>





The latest issue and back issues of KRH  
are available here.



---

### Editors

Ryuta Kasada, Yoshinori Onose, Rie Umetsu,  
Shigeyuki Takagi, Haruhiko Morito, and  
Motomichi Koyama

---

### Editorial Staff

Misa Y. Tomimatsu, Aki Oikawa, and Yuko Godart

---

### Printing

HOKUTO Corporation

---

### Organization

Institute for Materials Research  
Tohoku University  
2-1-1 Katahira, Aoba-ku, Sendai 980-8577, Japan  
Tel. +81-(0)22-215-2144 Fax. +81-(0)22-215-2482

URL: <http://www.imr.tohoku.ac.jp/>  
E-mail: [pro-adm.imr@grp.tohoku.ac.jp](mailto:pro-adm.imr@grp.tohoku.ac.jp)



東北大学 金属材料研究所  
**Institute for Materials Research**  
**Tohoku University**

2-1-1 Katahira, Aoba-ku  
Sendai 980-8577, Japan

<http://www.imr.tohoku.ac.jp/>